



University of Kentucky  
UKnowledge

---

University of Kentucky Doctoral Dissertations

Graduate School

---

2011

## FABRICATION AND CHARACTERIZATION OF MESOSCALE PROTEIN PATTERNS USING ATOMIC FORCE MICROSCOPY (AFM)

Pei Gao

University of Kentucky, pgao2@uky.edu

[Right click to open a feedback form in a new tab to let us know how this document benefits you.](#)

---

### Recommended Citation

Gao, Pei, "FABRICATION AND CHARACTERIZATION OF MESOSCALE PROTEIN PATTERNS USING ATOMIC FORCE MICROSCOPY (AFM)" (2011). *University of Kentucky Doctoral Dissertations*. 827.  
[https://uknowledge.uky.edu/gradschool\\_diss/827](https://uknowledge.uky.edu/gradschool_diss/827)

This Dissertation is brought to you for free and open access by the Graduate School at UKnowledge. It has been accepted for inclusion in University of Kentucky Doctoral Dissertations by an authorized administrator of UKnowledge. For more information, please contact [UKnowledge@lsv.uky.edu](mailto:UKnowledge@lsv.uky.edu).

ABSTRACT OF DISSERTATION

Pei Gao

The Graduate School  
University of Kentucky  
2011

FABRICATION AND CHARACTERIZATION OF MESOSCALE PROTEIN  
PATTERNS USING ATOMIC FORCE MICROSCOPY (AFM)

---

ABSTRACT OF DISSERTATION

---

A dissertation submitted in partial fulfillment of the  
requirements for the degree of Doctor of Philosophy in the  
College of Arts and Sciences  
at the University of Kentucky

By

Pei Gao

Lexington, Kentucky

Director: Dr. Yuguang Cai, Department of Chemistry

Lexington, Kentucky

2011

Copyright © Pei Gao 2011

## ABSTRACT OF DISSERTATION

### FABRICATION AND CHARACTERIZATION OF MESOSCALE PROTEIN PATTERNS USING ATOMIC FORCE MICROSCOPY (AFM)

A versatile AFM local oxidation lithography was developed for fabricating clean protein patterns ranging from nanometer to sub-millimeter scale on octadecyltrichlorosilane (OTS) layer of Si (100) wafer. This protein patterning method can generate bio-active protein pattern with a clean background without the need of the anti-fouling the surface or repetitive rinsing.

As a model system, lysozyme protein patterns were investigated through their binding reactions with antibodies and aptamers by AFM. Polyclonal anti-lysozyme antibodies and anti-lysozyme aptamer are found to preferentially bind to the lysozyme molecules on the edge of a protein pattern before their binding to the interior ones. It was also demonstrated that the topography of the immobilized protein pattern affects the antibody binding direction. We found that the anti-lysozyme antibodies binding to the edge lysozyme molecules on the half-buried pattern started from the top but the binding on the extruded pattern started from the side because of their different spatial accessibility.

In addition, after incubating lysozyme pattern with anti-lysozyme aptamer in buffer solution for enough long time, some fractal-shaped aptamer fibers with 1-6nm high and up to tens of micrometers long were formed by the self-assembling of aptamer molecules on the surface. The aptamer fibers anchor specifically on the edge of protein patterns, which originates from the biospecific recognition between the aptamer and its target protein. Once these edge-bound fibers have formed, they can serve as scaffolds for further assembly processes. We used these aptamer fibers as templates to fabricate palladium and streptavidin nanowires, which anchored on the pattern edges and never cross over or collapse over each other. The aptamer fiber scaffold potentially can lead to an effective means to fabricate and interface nanowires to existing surface patterns.

KEYWORDS: Atomic Force Microscopy (AFM), Protein Patterns, Lysozyme,  
Aptamer, Nanowires

Pei Gao

08-22-2011

FABRICATION AND CHARACTERIZATION OF MESOSCALE PROTEIN  
PATTERNS USING ATOMIC FORCE MICROSCOPY (AFM)

By

Pei Gao

*Dr. Yuquang Cai*

---

Director of Thesis

*Dr. John E. Anthony*

---

Director of Graduate Studies

*08-22-2011*

---

## RULES FOR THE USE OF DISSERTATIONS

Unpublished dissertations submitted for the Doctor's degrees and deposited in the University of Kentucky Library are as a rule open for inspection, but are to be used only with due regard to the rights of the authors. Bibliographical references may be noted, but quotations or summaries of parts may be published only with the permission of the author, and with the usual scholarly acknowledgments.

Extensive copying or publication of the dissertation in whole or in part also requires the consent of the Dean of the Graduate School of the University of Kentucky.

A library that borrows this dissertation for use by its patrons is expected to secure the signature of each user.

Name

Date

---

---

---

---

---

---

---

---

---

---

DISSERTATION

Pei Gao

The Graduate School

University of Kentucky

2011



FABRICATION AND CHARACTERIZATION OF MESOSCALE PROTEIN  
PATTERNS USING ATOMIC FORCE MICROSCOPY (AFM)

---

DISSERTATION

---

A dissertation submitted in partial fulfillment of the  
requirements for the degree of Doctor of Philosophy in the  
College of Arts and Sciences  
at the University of Kentucky

By

Pei Gao  
Lexington, Kentucky  
Director: Dr. Yuguang Cai, Department of Chemistry  
Lexington, Kentucky  
2011  
Copyright © Pei Gao 2011

*For my well-beloved family*

## ACKNOWLEDGMENTS

I would like to express my greatest thanks to Professor Yuguang Cai who gave me helpful guidance and provided me an environment to improve my personal scientific research ability from the beginning of this research work to its completion. In the last five years, Professor Yuguang Cai's inexhaustibility in researching and teaching showed me a right way to work and study, and this is really important for my future career.

Many thanks to my research committee: Dr. Dong-Sheng Yang, Dr. Mark D. Watson and Dr. Tonglei Li. Your valuable suggestion and discussion are indispensable in developing this dissertation.

To my collaborators: Professor Yinan Wei at University of Kentucky, Professor Mehdi M. Yazdanpanah and Professor Robert W. Cohn at University of Louisville. This research work cannot be completed without your collaboration.

I must earnestly be grateful to my parents and my friends whose love and support made this work possible. Although my parents in China are thousands of miles away from me, their endless hours of child care, unrelenting optimism make me brave to go through difficulties times in my studying and working.

Finally, I would like to thank my husband Quanzhen Huang and my daughter Annie Huang who are always bringing me endless love, laughter and inspiration. Their support and encouragements make me a positive and confident person.

## TABLE OF CONTENTS

Acknowledgments.....	iii
Table of Contents.....	iv
List of Tables.....	vii
List of Schemes.....	viii
List of Figures.....	ix
Chapter 1- Introduction.....	1
1.1. Fabrication of nanopatterns of protein: motivation and techniques.....	1
1.2. Conventional nanofabrication methods .....	2
1.3. Novel lithographic methods .....	3
1.4. AFM operation principle and instrumentation .....	7
1.5. AFM imaging conditions .....	12
1.6. Objectives of this thesis .....	15
1.7. Organization of this thesis.....	15
Chapter 2-The fabrication and characterization of self-assembled monolayers.....	17
2.1. Introduction .....	17
2.2. Experimental part to prepare and characterize SAMs .....	18
2.2.1. Instrumentation.....	18
2.2.1.1. Ellipsometry.....	19
2.2.1.2. Fourier transform infra-red (FT-IR) spectrometry .....	22
2.2.2. Preparation of the Self-assembled monolayer on Si(100) wafer .....	26
2.2.2.1. Materials .....	26
2.2.2.2. Experimental procedure to prepare SAMs .....	26
2.2.2.3. The characterization of OTS film on silicon wafer .....	27
2.3. Conclusion of chapter 2 .....	30
Chapter 3- AFM Local oxidation lithography.....	31
3.1. Introduction .....	31
3.2. Experimental of AFM local oxidation lithography .....	33
3.2.1. Material .....	33
3.2.2. Instrument .....	33
3.2.3. Fabrication and characterization of OTSpd chemical patterns .....	33
3.2.4. The identification of OTSpd pattern.....	36
3.3. Conclusion of chapter 3.....	42
Chapter 4- A method for fabricating protein patterns on the octadecyltrichloro- silane (OTS) surface through paper swabbing.....	43
4.1. Introduction.....	43

4.2. Experimental.....	44
4.2.1. Preparation of self-assembled OTS film and OTSpd chemical patterns .....	44
4.2.2. The Fabrication and characterization of protein patterns .....	46
4.2.2.1. Immobilize lysozyme molecules on the OTS surface.....	46
4.2.2.2. Immobilize catalase molecules on the surface.....	52
4.2.2.3. Immobilize CaM molecules on the surface.....	54
4.3. Conclusion of Chapter 4.....	56
Chapter 5- The Boundary Molecules in a Lysozyme Pattern Exhibit Preferential	
Antibody Binding.....	57
5.1. Introduction .....	57
5.2. Experimental. ....	58
5.2.1. Two schemes to fabricate protein patterns.....	58
5.2.1.1. Immobilize lysozyme molecules on the OTSpd.....	59
5.2.1.2. Immobilize lysozyme molecules on the OTSpd-UTSox surfaces .....	61
5.2.2. lysozyme activity characterization through the binding with antibody..	62
5.2.2.1. Boundary binding effect on the lysozyme pattern from Scheme	
5.1.....	62
5.2.2.2. Boundary binding effect on the lysozyme pattern from Scheme	
5.2.....	69
5.3. Conclusion of Chapter 5 .....	73
Chapter 6- Label-free detection of the aptamer binding on protein patterns using	
Kelvin probe force microscopy (KPFM) .....	74
6.1. Introduction.....	74
6.2. Experimental.....	75
6.2.1. Fabrication of protein patterns on the OTS film.....	75
6.2.2. Boundary effect for aptamer binding on the lysozyme pattern.....	77
6.2.3. The working principle of Kelvin Probe force microscopy (KPFM).....	82
6.2.4. The KPFM characterization of aptamer binding.. .....	87
6.3. Conclusion of Chapter 6.....	90
Chapter 7- Aptamer fiber anchored on the edge of a protein pattern: a template	
for nanowire fabrication.....	92
7.1. Introduction.....	92
7.2. Experimental .....	93
7.2.1. Fabrication of aptamer fibers on the edge of protein pattern.....	93
7.2.2. Characterization of aptamer fibers on the edge of protein pattern...101	
7.2.3. The diffusion-limited aggregation (DLA) theory.....	105

7.2.4. The aptamer fibers were converted into Pd nanowires.....	108
7.2.5. Streptavidin assembled on the fibers made of biotin-tagged aptamers .....	111
7.3. Conclusion of chapter 7.....	114
Chapter 8- Conclusions and future projects.....	115
8.1. Conclusions.....	115
8.2. Large-scale fabrication of protein nanoarrays based on nanosphere lithography.....	116
8.3. The investigation of surface properties of OTSpd patterns.....	122
Reference.....	133
Vita.....	149

## LIST OF TABLES

Table 6-1. The CPD values of lysozyme pattern and the aptamer-lysozyme complex.....	88
Table 8-1. The statistical analysis result of adhesion forces obtained from the fifty points measured on OTS, OTSpd and UTSox surface.....	132

## LIST OF SCHEMES

Scheme 3-1. The fabrication of OTSpd and UTSox patterns in $50 \times 50 \mu\text{m}^2$ of OTS surface area.....	39
Scheme 5-1. The fabrication of a half buried lysozyme pattern on OTS surface.....	60
Scheme 5-2. The fabrication of a fully exposed lysozyme pattern on OTS surface.....	60
Scheme 7-1. The fabrication of nanowires on DNA template.....	95
Scheme 8-1. Procedure for preparation of large-scale positive-toned protein patterns.....	118
Scheme 8-2. Procedure for preparation of large-scale negative-toned protein patterns.....	120



## LIST OF FIGURES

Figure 1-1. Basic procedures of the three AFM nanofabrication methods.....	7
Figure 1-2. Schematic diagram of AFM working principle .....	9
Figure 1-3. Theoretical curve showing the interatomic force.....	11
Figure 2-1. The structures and formula of silanes used in this thesis.....	18
Figure 2-2. A two-layer model used for ellipsometry.....	20
Figure 2-3. The layout of laser ellipsometry measurement system.....	21
Figure 2-4. The layout of FT-IR measurement system.....	24
Figure 2-5. The illustration of a p-polarized IR beam incident.....	25
Figure 2-6. Schematic representation of the formation of OTS monolayer.....	27
Figure 2-7. FTIR spectra in the C-H stretching region of Si(100)/SiO <sub>2</sub> .....	28
Figure 2-8. AFM images of OTS layer adsorbed on the silicon surface.....	29
Figure 2-9. The plot of the C-H stretch bands region area in the Brewster's angle IR spectra of different silanes with methylene and methyl group Numbers.....	29
Figure 3-1. Schematic view of AFM local oxidation lithography.....	34
Figure 3-2. A 3x3 array of OTSpd disc-shaped pattern fabricated on the OTS ...	35
Figure 3-3. The topography image of the OTSpd pattern on OTS SAMs.....	36
Figure 3-4. The schematic reaction of PDAM with carboxylic acid group.....	36
Figure 3-5. The Brewster angle IR spectra of the UTS and UTSox monolayer....	38
Figure 3-6. The oxidation process of UTS to UTSox.....	38
Figure 3-7. The fluorescence microscope image of OTSpd and UTSox patterns.	41
Figure 4-1. The structure of OTS .....	45
Figure 4-2. The hydrolysis reaction of lysozyme.....	46
Figure 4-3. The topography image of the lysozyme pattern.....	48
Figure 4-4. Anti-lysozyme antibodies selectively bound on lysozyme patterns....	50
Figure 4-5. Infrared spectra of lysozyme and lysozyme-antibody complex.....	51
Figure 4-6. The catalase pattern fabricated on the OTSpd pattern.....	53
Figure 4-7. An oxygen bubble generated over the catalase pattern.....	54
Figure 4-8. The structure and formula of MUTMS.....	55
Figure 4-9. The CaM pattern fabricated on the OTSpd-MUTMS pattern.....	55
Figure 5-1. Representative lysozyme pattern on the OTSpd template.....	59
Figure 5-2. The heights of a pattern during the surface reactions in Scheme 5.2.	62
Figure 5-3. Polyclonal antibodies preferentially bind to the edge of lysozyme....	64
Figure 5-4. Analysis of the antibody height and phase contrast.....	64
Figure 5-5. Control test of the antibody binding.....	65
Figure 5-6. Antibody binding to the loosely packed, submonolayer lysozyme pattern and the tightly packed, full monolayer lysozyme pattern.....	67
Figure 5-7. High-resolution AFM image of lysozyme pattern.....	68
Figure 5-8. Antibodies preferentially bind to the OTSpdUTSox-lysozyme.....	70

Figure 5-9. Lysozyme pattern immobilized on the OTSpdUTSox template.....	71
Figure 6-1. A representative lysozyme disc pattern.....	77
Figure 6-2. The topography and phase images of the tightly packed lysozyme...	78
Figure 6-3. The topography and phase images of a representative lysozyme disc after incubation with a solution of randomly generated 42-mer.....	79
Figure 6-4. The topography image of the loosely packed and tightly packed lysozyme patterns after incubation with anti-lysozyme aptamers.....	82
Figure 6-5. The SEM image of AG <sub>2</sub> Ga needle tip.....	84
Figure 6-6. The comparison of AFM image.....	86
Figure 6-7. The KPFM characterization of lysozyme patterns.....	89
Figure 6-8. A side-by-side comparison of the surface potential images of an aptamer-bound lysozyme pattern and a lysozyme pattern.....	90
Figure 7-1. Lysozyme patterns after incubation with antilysozyme aptamers.....	98
Figure 7-2. The topography image of aptamer fibers.....	100
Figure 7-3. The phase image of long aptamer fibers.....	100
Figure 7-4. The analysis of complimentary sequences in Anti-lysozyme aptamer .....	102
Figure 7-5. The analysis of complimentary sequences in the random aptamer...	103
Figure 7-6. Fluorescent image of ethidium bromide-stained aptamer fibers.....	104
Figure 7-7. The logarithm of perimeter was plotted versus the logarithm of area	107
Figure 7-8. Aptamer fibers were converted into Pd nanowires.....	109
Figure 7-9. SEM image of Pd nanowires.....	110
Figure 7-10. FITC-labeled streptavidin assembled on the biotin-tagged aptamer .....	113
Figure 8-1. The Scheme 8.2d sample images taken separately under the white light and fluorescence.....	121
Figure 8-2. The negative-toned protein patterns.....	121
Figure 8-3. The topography image of UTSoxOTSpd patterns.....	124
Figure 8-4. The surface potential image of OTSpd and UTSox patterns.....	125
Figure 8-5. The fluorescence microscope image of OTSpd and UTSox patterns .....	125
Figure 8-6. The spatial hindrance of the higher molecules.....	126
Figure 8-7. The topography and friction images obtained during the contact mode scanning with different loading forces.....	128
Figure 8-8. The friction force as a function of AFM tip loading force.....	130
Figure 8-9. Schematic representation of a force-distance curve.....	132

# CHAPTER 1

## INTRODUCTION

### 1.1. Fabrication of nanopatterns of protein: motivation and techniques

Nanoscale protein patterns serve as one of the key elements in many fields including enzyme catalysis, biosensors, tissue engineering, diagnostic protein tips and pharmacology.<sup>1-3</sup> Surfaces covered with patterned proteins are especially crucial in biosensors, modified microscopic electrodes, and implanting devices.<sup>4-6</sup> However, precisely and easily immobilizing protein molecules on a specific place while retaining their native biological functionality is a difficult and challenging task. Besides immobilization techniques, the miniaturization of protein arrays is also quite important because of the huge potentials for the nanoscale protein pattern in future research. The development of smaller biosensors and biochips could potentially increase the sensing element density, improve detection limits, and reduce the analysis time and cost of analysis.<sup>7</sup> Therefore, many efforts have been devoted to the development of microfabrication techniques for the production of two dimensional protein patterns.<sup>8-14</sup>

Generally, a patterned substrate that contains some protein adhesives and resistive terminated groups is necessary for the selective binding of protein molecules from the liquid phase. Then, the sample with the chemical patterns is exposed to the protein solution to let the protein molecules accumulate on the patterned area. The driving forces for protein adsorption on the chemical patterns are electrostatic interactions, covalent bonding and bio-specific linkage.<sup>15-17</sup>

There are some conventional patterning techniques in the lab for fabricating nanometer to micrometer-sized arrays on surfaces, for example, photolithography,<sup>18</sup> and scanning electron beam lithography.<sup>19</sup> However, because of their unfriendly working environment, these conventional patterning techniques are limited in patterning certain organic and biological samples.

Therefore, there are several novel lithographic methods showing up including nanoimprinting lithography,<sup>20,21</sup> soft lithography,<sup>22-24</sup> and scanning probe lithography<sup>25,26</sup> to meet this urgent need. These novel lithographic methods are capable of creating nano-sized patterns on substrates with a mild patterning condition. Since they were published, these patterning methods have been widely applied in many research areas based on their different patterning characteristics, respectively.

## **1.2. Conventional nanofabrication methods**

Photolithography is one of the most traditional ways used for metal patterning in the microcircuits area. In this method, as a beam of UV light is cast on an optical mask covered surface, either the exposure part or the area beneath the mask will be etched away. Therefore, the designed patterns on the mask will be transferred onto the surface. This method is widely used in semiconductor industry because of its well known fabrication capability. Not only can the pattern shape and size on the surface be precisely controlled, but the photolithograph is also capable of generating a large pattern area on a surface. However, the resolution of this method inhibits its further development in the nanotechnology field. The resolution of photolithography is limited by optical diffraction.<sup>27</sup> The theoretical resolution of photolithography is about half of the wavelength of the light source used,<sup>27</sup> but the actual minimum feature size that can be fabricated is approximately the wavelength of the light source in the lab. The shorter wavelength lights (down to 157 nm) have been tried to reduce pattern feature size to less than 50nm.<sup>28</sup> However, the use of short wavelengths below 157 nm (deep UV and soft X-ray wavelengths) causes increased technical difficulties, particularly in developing new optical elements.<sup>29-33</sup>

Scanning electron beam lithography is another approach to make nanostructures on surfaces. This technique creates patterns line-by-line by scanning a high-energy beam of electrons or ions over a resist material. It is much slower than photolithography. It has been used in the production of mask and reticles for optical lithography, and for making very small scale devices as

well. The resolution of the electron beam lithography is limited by high-energy secondary electrons and the scattered electrons within the resist layer and substrate. It is reported that the resolution of electron beam lithography is above 10 nm.<sup>34</sup> In the newly developed method – focused beam lithography, the electron beam was replaced by an ion beam to improve its resolution. Because ions are heavier than electrons, the back scattering from the substrate can be minimized. Therefore, the resolution of focused beam lithography can reach 5nm compared with the electron beam lithography. Focused beam lithography has not been widely used due to a limited development so far.<sup>18</sup>

In summary, photolithography and scanning electron beam lithography have been highly developed and applied in semiconductor and integrated circuit fabrication. However, they are both not ideal in patterning some organic and biological samples because of the intense damage to surfaces. Therefore, some novel lithographic methods with a higher resolution and better accessibility for other fields have been urgently required to overcome their technical and financial limitations.

### **1.3. Novel lithographic methods**

There are several novel lithographic methods including nanoimprinting lithography, soft lithography, and scanning probe lithography.

Soft lithography also called micro-contact printing ( $\mu$ CP) was first demonstrated by Whitesides and coworkers.<sup>35</sup> The method is based on the use of an elastomeric stamp, which is cast and cured against a master created by photolithography or electron-beam lithography. The elastomeric stamp is typically made of polydimethylsiloxane (PDMS) and is capable of transferring “ink” molecules when they came in contact with target surfaces. The inking of PDMS stamps is processed by immersing them in different solutions corresponding to various substrates where ink molecules are transferred later; like thiols are used for noble metals or zinc selenide substrates<sup>36-38</sup> while silanes are used for silicon substrates.<sup>39</sup> The highly hydrophobic PDMS material allows the ink to be diffused not only on the surface but also in the bulk of the stamp material. This

diffusion in the bulk creates an ink reservoir for multiple prints. After the stamp is airdried, it is ready to transfer patterns on surfaces. Ink molecules will be transferred onto various solid surfaces once the PDMS mold comes in contact with substrates, which results in the formation of a self-assembled monolayer (SAM) on the contact area. This patterned self-assembled monolayer can be used as a resist for further pattern transfer. The resolution of the soft-lithography is limited by the mode feature size and the lateral diffusion of the ink molecules on substrates. Normally, the feature size can be made as small as 200 nm and the lateral feature size can reach below 100 nm by using a stiff mold as-called hard PDMS and UV-cured PDMS.<sup>40,41</sup> Since it is a one-step procedure to transfer a series of features onto surfaces, several other techniques founded on the application of the PDMS have been developed, such as micro-transfer printing ( $\mu$ TP),<sup>42</sup> replica molding,<sup>43</sup> and micro-transfer molding ( $\mu$ TM).<sup>44</sup>

Another stamping method is nanoimprint lithography. In this technique, a rigid mold is used to physically deform a thermoplastic polymer coated on a substrate to form micro or nanostructures. The imprint mold can be made of either metal or silicon dioxide produced on a silicon substrate. The imprint is normally done at a high pressure, around 50 bar, and in an elevated temperature ranging from 100 to 200 °C. The operation temperature is dependent on the glass transition temperature of the polymer-coated surfaces. It has been demonstrated that the resolution of nanoimprinting lithography can reach 6 nm.<sup>21</sup> The application of this technique is limited because the surface coating has to be thermoplastic polymer and the fabrication can not be done under normal pressure and temperature.

Scanning probe lithography (SPM) is a new class of surface modification techniques stemming from either scanning tunneling microscope (STM)<sup>26</sup> or atomic force microscope (AFM).<sup>25</sup> AFM is a newly developed instrument created in 1986 that has quickly attracted intense interest due to its great capability to image surfaces with high spatial resolution.<sup>45-49</sup> Many materials such as organic thin films,<sup>46,50-52</sup> metals,<sup>53-56</sup> and semiconductors<sup>57-60</sup> have been characterized at molecular or atomic resolution. For AFM scanning, a sharp probe is rastered

across sample surfaces to record the probe-surface interaction as a function of position. Typically, the dimension of the AFM tip is tens of nanometers. The sharp AFM tips have been explored as a way to fabricate nanosized patterns on surfaces and subsequently characterize them. The way of AFM working on surfaces will be explained later.

By taking advantage of the localized interaction between the AFM tip and surfaces, people have developed several different kinds of AFM based patterning techniques, including nanoshaving,<sup>61,62</sup> nanografting,<sup>63</sup> dip-pen nanolithography,<sup>64-67</sup> and AFM local oxidation lithography.<sup>68,69</sup> Due to their easy manipulation (no stamp is needed) and high resolution (less than 10nm) properties, these AFM based technologies have achieved their great successes in the area of nanoscale biological molecules patterning. According to their different patterning characteristics, different types of AFM tips, such as contact mode tips, tapping mode tips, or lab-made user coated tips are used to fabricate nanosized patterns on the self-assembled monolayers (SAMs). A self-assembled monolayer, is a layer of organic molecules self-assembled on a substrate, is typically used in AFM based lithography techniques. An AFM tip is capable of patterning structures on organic monolayers through displacing the surface coated molecules with a high load force on substrates, electrochemical degrading molecules with a potential applied between AFM tip and substrates, and transferring “ink” molecules from a precoated tip to replace background molecules on surfaces. Therefore, the created patterns following the scanning track of the tip can have a designated size, chemical properties, and adjustable topography. Moreover, the patterned sample surface can be characterized by the same AFM probe with a high resolution. In the following paragraph, I will simply explain some AFM based nanolithography patterning techniques used in labs.

Nanoshaving is accomplished by exerting a high load on an AFM tip during scanning. In the process, the high shear force pushes the tip to come in contact with the underlying substrate and shaves the adsorbed molecules off the surface to expose an area of uncovered substrate. Some nanopatterns such as

holes or trenches are fabricated with one to several scans. After switching to a lower force, the created negative pattern can be characterized by the same tip.

Nanografting is a technique that combines nanoshaving and molecule self-assembly techniques. It uses a moving AFM tip to mechanically displace molecules on the SAMs in a liquid cell with a high force load on surfaces. Then, new molecules from the solution immediately adsorb onto the grafted area, like thiol molecules contained in the solution can adsorb onto the freshly exposed gold area. Either negative or positive patterns can be fabricated by using different chain lengths of thiols contained in the solution to replace the background thiol. The same AFM tip can be used to image the produced nanopatterns at a reduced loading force.

Dip-pen nanolithography (DPN) was originally demonstrated by Mirkin and coworkers. It uses molecules of interest as the “ink”, an AFM tip as a pen “nib” and a solid substrate with a chemical affinity with the ink as “paper”.<sup>67</sup> The tip has been pre-coated with different adsorbates before it is applied in this technique. When a pre-coated AFM tip is scanning surfaces, it can directly “write” patterns in a submicrometer dimension on the surface. The pattern created consists of a small collection of molecules delivered from the AFM tip through the water meniscus between the tip and the substrate. The principal procedures of nanoshaving, nanografting, and DPN are illustrated in Figure 1.1.

In AFM local oxidation lithography, a conductive AFM tip is installed, and the contact mode is operated while a tip is scanning on alkylchlorosilanes self-assembled monolayers on the silicon substrates. A bias of about 5-10v is applied between the silicon (100) substrate and the conductive AFM tip. In the 100% humid environment (at 25°C), the layer of alkylchlorosilanes under the AFM tip is partially deconstructed, forming a partially degraded, carboxylic acid-terminated pattern in this oxidation process. AFM local oxidation is the basic protein patterning technique used in this thesis, and it will be further introduced in chapter three.



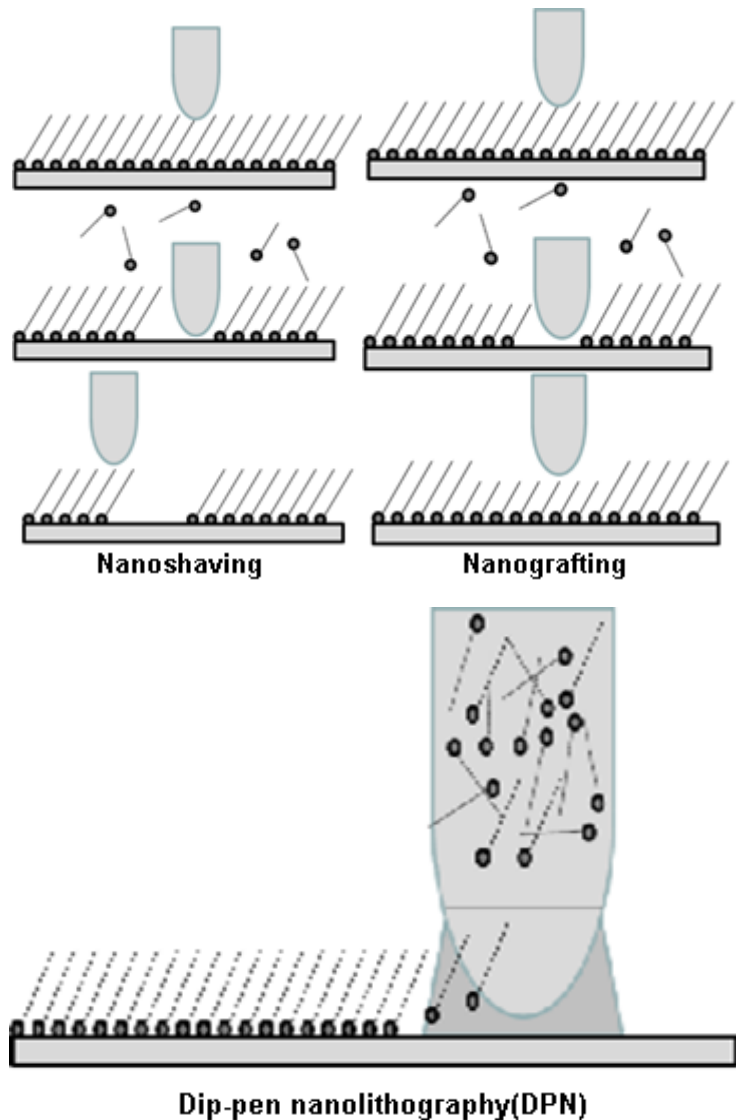


Figure 1-1. Basic procedures of the three AFM nanofabrication methods

#### 1.4. AFM operation principle and instrumentation

AFM was first invented by Quate and Gerber in 1986,<sup>25</sup> and was first commercially available in 1989. AFM is one of a family of scanning probe microscope types and has been a tool of great importance in biological science since its invention. Compared with other complementary techniques such as electron microscopy, AFM has a lot of extra advantages as an imaging tool in biology and physics which electron microscopy is not currently able to offer. Beyond its unique capabilities of visualizing at molecular level, AFM is also

capable of presenting more information about the sample of interest on a surface including topography, stiffness, adhesive force,<sup>70-72</sup> frictional force<sup>50,52,73,74</sup> and so on. In addition, besides being used in air and UHV (ultra-high-vacuum) media, AFM allows samples to be scanned under liquids which can be modified or changed during the imaging in real time. Therefore, this manner of imaging samples in a liquid cell provides us a chance to observe live biological activities in their native condition of need.<sup>75</sup> Using AFM, there have been many studies of biological materials including nucleic acids and their complexes with proteins, individual isolated proteins, membrane and membrane bound proteins, and living cells.<sup>76</sup> It was also demonstrated that the instrument can manipulate molecules on various surfaces through physical grafting or electrochemical reactions with the help of a conductive AFM tip. Besides that, it was also reported that AFM is capable of measuring the strength of molecular interaction through a functionalized AFM tip covered with some specific biological molecules.<sup>77</sup> This tip was placed on a sample surface to sense the specific interaction between different molecules on this surface and the AFM tip with pico-newton sensitivity.<sup>77,78</sup>

There are different parts working together to accurately operate an AFM instrument, including an AFM tip, a scanner, feedback electronics, and so on. A schematic diagram of a home-built atomic force microscope is shown in Figure 1.2.<sup>79</sup> The resolution that a typical AFM can achieve is 2-10nm in the x, y direction and 0.1nm in the z direction. A high resolution image can be obtained by a rastered probe scanning across a sample surface to record the tip and surface interaction. It is known that AFM probes the surface of a sample with a sharp tip; thus, one of the most important factors influencing the resolution is the sharpness of the tip. Normally, an AFM tip has a radius of curvature of around 10nm and is fabricated on free end of a thin cantilever arm which is 100 to 200  $\mu\text{m}$  long. Because the AFM tip is the only part to interact with the surface when it is scanning, its size, shape, and material are all critical to the interpretation of the information on the surface. In our experiment, all the tips used are pyramidal in shape and made of  $\text{SiO}_2$ .

When the AFM tip is scanning a surface, forces between the tip and the sample surface cause the cantilever to bend, or deflect. A photodetector measures the cantilever deflection as the tip is scanning the surface by recording the positions of a laser beam reflected from the back of the cantilever. The photodetector consists of four side-by-side elements of quadrant photodiodes which are sensitive to the position where the laser strikes. When an AFM tip is rastering across the surface, the laser point on the photodetector is deflected up and down or left and right on the four segments of the photodiode. The difference between the top and bottom photodiode signals indicates the bending of the cantilever in the vertical direction, which represents the three dimensional shape of the sample surface. The difference between the left and right photodiode signals indicates the torsion of the cantilever in the horizontal direction, which represents the force of the sample surface with the AFM tip. The torsion, or twisting, of the cantilever will increase or decrease depending on the frictional characteristics associated with the surface. The measured cantilever deflections allow a computer to generate a map of surface topography. Based on this working mechanism, AFM is capable of studying insulators and semiconductors, as well as electrical conductors.

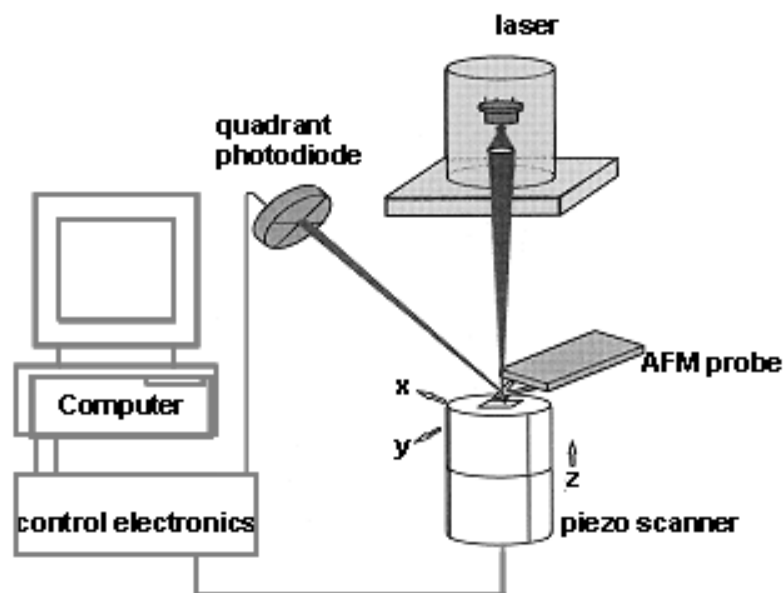


Figure 1-2. Schematic diagram of AFM working principle

There are several forces that typically contribute to the deflection of an AFM cantilever. The force most commonly associated with AFM is van der Waals force. Based upon the distance between the tip and the sample, and thus different interatomic forces, there are two kinds of AFM operating modes involved in this paper – contact mode and tapping (non-contact) mode. The two distance regions of contact mode and non-contact mode are red-labeled on Figure 1.3, respectively. In the contact region, the AFM cantilever is held less than a few angstroms from the sample surface, and the interatomic force between the cantilever and the sample is repulsive. In the non-contact region, the AFM cantilever is held on the order of tens to hundreds of angstroms from the sample surface, and the interatomic force between the cantilever and the sample is attractive. In different operating modes, various AFM tips with different parameters, such as surfacing coating or force constant, are used in our lab. In the contact mode, an AFM tip with around a  $0.15\pm 0.01$  N/m force constant is used to contact the sample surface all the way through the adsorbed fluid layer during the scanning. To acquire the image, a feedback loop monitors a small constant force between the cantilever and the sample of interest. However, in the intermittent region, an AFM tip with a much higher force constant ranging from 1.5-12.5 N/m is used, and the tip lightly taps on the sample surface during the scanning. This is referred to as tapping mode. In contrast with the contact mode, the tapping mode works by maintaining a constant oscillation amplitude of the AFM tip on the surface through the feedback loop. Because the tapping mode avoids dragging the tip around the surface, it has more advantages in probing the soft sample surface than the contact mode. The imaging mode used in this thesis is primarily tapping mode. In the following section, the three imaging modes working in the different force regions specified in Figure 1.3 will be described in detail, respectively.

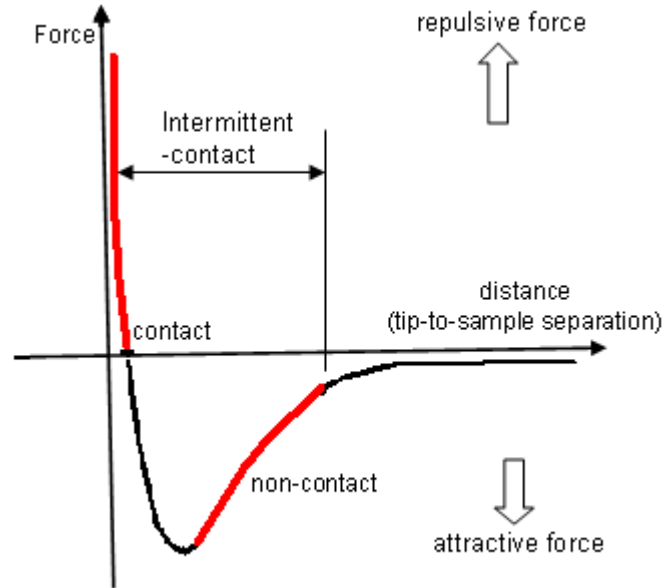


Figure 1-3. Theoretical curve showing the interatomic force between the tip and sample as a function of tip-sample separation

The other important part for AFM imaging on sample surfaces is an AFM scanner, which is a tube-shaped piezoceramics. Piezoceramics is a class of material that can elongate or contract proportionally to the voltage gradient applied to it. Conversely, it creates a voltage gradient when forced to expand or contract. There are four electrodes covering the outer surface of the tube, while a single electrode covers the inner surface. An application of voltage to one or more of the electrodes causes the tube to bend or stretch. Therefore, an AFM scanner can manipulate samples and probes with high precision in three dimensions. During the scanning, an AC voltage is applied to the different electrodes of the piezoelectric scanner to produce a scanning raster motion in the X and Y directions. The feedback system maintains a constant deflection of the laser beam on the quadrant photodiode by vertically moving the scanner at each x & y point all the time. By correlation, point by point, the feedback system's status with the scanner's motions, the z position is plotted against the X and Y scanning to provide the topography image, while the left and right signals from the photodiode simultaneously produce the friction image as well.

## 1.5. AFM imaging conditions

In contact mode, the AFM tip and sample surface are always in contact during imaging. Typically, images are acquired in the repulsive interaction region, where the cantilever bends upwards. Besides the repulsive van der Waals force mentioned above, there are two types of other forces contributing the contact mode scanning: a capillary force exerted by the thin water layer often present in an ambient environment, and the force exerted by cantilever itself. The magnitude of the capillary force depends upon the tip-to-sample separation. The force applied by the cantilever is like the force of a compressed spring which follows Hook's law  $F=K_c z$ , where  $K_c$  is the cantilever force constant and  $z$  is the displacement from equilibrium of the cantilever. During the imaging, the cantilever deflection is maintained constant by moving the piezo up or down. The output of the z-piezo voltage of the sample is plotted against the X, Y scanning to manifest a topographic image. Contact mode is the most common mode used in the AFM imaging, which can be applied to the different sample, especially for a rough surface with a high scanning speed. Additionally, it is capable of providing the friction information between AFM tip and the surface. Contact mode is avoided in imaging biological molecules on a surface, or a relative soft surface, because AFM tip can easily pick up some molecules or scrape the surface itself during the scanning.

For tapping mode, the cantilever on an AFM probe was oscillated at or near its resonant frequency, and only lightly taps the surface on the end of each oscillation during the scanning. The movement of the cantilever on the sample surface can be considered as a forced harmonic oscillator. To better understand the working principle of AFM tapping mode, we can start from a single harmonic motion (SHM). The angular frequency and the displacement of an oscillator in SHM are given by equation (1) and (2), separately.

$$\omega = \sqrt{\frac{k}{m}} \quad (1)$$

$$x = A \cos(\omega t + \psi) \quad (2)$$

Here,  $k$  is the force constant, and  $m$  is the mass,  $A$  and  $\Psi$  separately mean amplitude and phase angle, which are determined by the initial position and velocity of the body. As an AFM tip approaches a sample, the van der Waals attractive force between the tip and the sample causes changes in both the amplitude and the phase of the cantilever oscillation, which makes a simple harmonic motion of AFM probe to a damped oscillation. With a damping force  $F_x = -bV_x$  proportional to velocity added to a simple harmonic oscillator, the angular frequency  $\omega'$  and the displacement of a damped oscillator  $x$  are given by:

$$x = Ae^{-(b/2m)t} \cos \omega't \quad (3)$$

$$\omega' = \sqrt{\left(\frac{k}{m} - \frac{b^2}{4m^2}\right)} \quad (4)$$

First, the amplitude  $Ae^{-(b/2m)t}$  is not constant but decrease with time because of the decreasing exponential factor  $e^{-(b/2m)t}$ . It also shows that the larger the value of  $b$ , the more quickly the amplitude decreases. Second, the angular frequency  $\omega'$  is no longer equal to  $\omega = (k/m)^{1/2}$  but is somewhat smaller. From the above equation, it is concluded that a damped oscillator left to itself will eventually stop moving. But we can maintain a constant-amplitude oscillation by applying a force that varies with time in a periodic or cyclic way, with a definite period and frequency. Suppose we force the oscillator to vibrate with an angular frequency  $\omega_d$  that is nearly equal to the natural angular frequency  $\omega'$ , the amplitude  $A$  of the forced oscillation depends on the frequency of a sinusoidal driving force  $F(t) = F_{max} \cos \omega_d t$ , with maximum Value  $F_{max}$  could be worked out as equation (5).

$$A = \frac{F_{max}}{\sqrt{\left(k - m\omega_d^2\right)^2 + b^2\omega_d^2}} \quad (5)$$

When  $k - m\omega_d^2 = 0$ , the first term under the radical is zero, so  $A$  has a maximum near  $\omega_d = (k/m)^{1/2}$ . By correlation, the AFM tapping mode tip is mounted on a piezo disk actuator. At the beginning, the tip's frequency response curve was measured. Based on this, a modulated voltage is applied to the piezo actuator to

oscillate the cantilever at or near its resonant frequency to generate a large amplitude.<sup>80</sup> As the cantilever bounces vertically, the reflected laser beam is deflected in a regular pattern over a photodiode array, generating a sinusoidal electronic signal. This signal is finally converted to a root mean square (RMS) amplitude value displayed in AC volts. When the AFM tip is getting close to the sample surface, the resonant frequency, oscillation amplitude, and phase are changed due to an interaction or repulsive force between the AFM tip and sample, which is referred as a small dumping we discussed before. These changes are associated with the information about the sample's characteristics, including vertical height, hydrophobicity, and hydrophilicity. Same to the contact mode, an electronic feedback system moves the piezo up or down, to maintain a constant oscillation amplitude by keeping a constant force between AFM tip and sample, when the tip is vibrating on the surface. The topographic image of the sample surface is generated by using the output Z-piezo voltage. The AFM tip always lightly "taps" the surface and it only touches the sample surface at the end of vibration, which is also called intermittent mode. Therefore, the tapping mode overcomes problems associated with friction, adhesion, electrostatic forces that plague conventional AFM scanning methods, by alternately placing the tip in contact with the surface. As a result, the tapping mode is the most common imaging mode used to screen the biological samples on the surface for a higher resolution and less damage to the surface.<sup>81</sup>

Non-contact is another probing method in the operation of AFM. During non-contact imaging, the tip is also oscillated at the resonance frequency of the cantilever. However, the difference with the tapping mode is that the tip does not come in contact with the surface during the oscillation, but was kept in a few of nanometers distance from the sample surface. When the tip is close enough to the sample surface, it will bend towards the surface due to the interatomic attractive force between the cantilever and the sample. The oscillation amplitude will be changed correspondingly. Similar to the tapping mode, the feedback system moves the piezo up and down to maintain a constant oscillation amplitude. The piezo movement in three dimensions is recorded to create a



topographic image of sample surface. Although the non-contact mode exerts a very low force to the surface, it is not often operated in ambient condition because of the poor resolution. The good resolution can be obtained through the operation in an ultra high vacuum (UHV) chamber.

## **1.6. Objectives of this thesis**

The major goal of this research includes three parts. Firstly, the introduction of AFM local oxidation lithography as a fundamental fabrication method in the whole research, and a good way to create chemical patterns on octadecyltrichlorosilane (OTS) silicon wafers. Secondly, different mesoscale protein patterns with clean background were fabricated on the above mentioned chemical patterns, and their activities were studied through the binding with antibody and surface reaction, which were directly visualized by Atomic force microscopy (AFM). Thirdly, metal and bio-functionalized nanowires based on the DNA template were fabricated and designated on the lysozyme patterned OTS silicon surface. To accomplish these goals, AFM, Kelvin probe force microscopy (KPFM), Fourier transform infrared spectroscopy (FTIR), Scanning electron microscope (SEM), Ellipsometry, and Fluorescence Microscope were used to provide different information.

## **1.7. Organization of this thesis**

Following the first general background introductory chapter, chapter 2 and chapter 3 will separately describe the SAMs and AFM local oxidation lithography, which are respectively the basic working substrate and technique used in this research. Chapter 4 will introduce a “paper swapping” way to fabricate various bio-active protein patterns with a clean background on the chemical patterns created by AFM local oxidation lithography. The boundary effect of the immobilized protein pattern to the antibody binding on different chemical islands will be described in chapter 5. Chapter 6 discusses the DNA aptamer fibers anchored on the edge of protein patterns, and chapter 7 shows

how to fabricate different nanowires on these DNA fibers templates. In these two chapters, multiple techniques such as AFM, KPFM, SEM, and Fluorescence microscope are used. The Chapter 8 will briefly summarize the current and future projects.

## CHAPTER 2

# THE FABRICATION AND CHARACTERIZATION OF SELF-ASSEMBLED MONOLAYERS (SAMs)

### 2.1. Introduction

Self-assembled monolayers (SAMs) are ordered molecular assemblies that are formed spontaneously by immersion of a substrate into a solution of active molecules in a solvent. SAMs have been the subject of extensive research due to the ease of preparation, the tenability of surface properties via modification of molecular structure and function,<sup>82-84</sup> high structural order and stability. The intensive study on these films showed us their promising application in biosensing,<sup>85-89</sup> corrosion inhibition,<sup>90,91</sup> lubrication,<sup>92-95</sup> lithographic resists, surface patterning,<sup>22,96,97</sup> and molecular device fabrication.<sup>98,99</sup>

Organic molecules can spontaneously assemble on solid surfaces by immersion of substrate into the solutions of interest. There are three important functions of the organic molecules to form SAM. Firstly, the head groups, those provide a strong adsorbate-substrate interaction, such as covalent bonding and electrostatic force. There are several types of molecules that can form self-assembled monolayer for example, silanes on the hydroxyl surface which contains oxidized silicon, mica, and glass;<sup>100-102</sup> other molecules with the same behavior are the thiols on Au(111),<sup>93,103-108</sup> thiols on Ag(111),<sup>109</sup> thiols on Cu(111),<sup>110</sup> and Alkanethiols on Ni.<sup>111</sup> The second part of the molecules is the long alkyl chain. The van der Waals interaction between the long alkane chains of adjacent organic molecules (8.4 KJ/mol per CH<sub>2</sub> group) contributes to the ordering of the layer on the substrate. The third part of the molecule is the terminal functional groups such as alkyls, amides, alcohols, carboxylic acids, esters, and nitriles. The interfacial characteristics of the monolayer can be changed by varying these terminal groups through different chemical

modifications on those surfaces. Therefore, the incorporation of various organic molecules on solid surfaces provides a means to tailor interfacial properties.

SAMs have been thoroughly characterized using a large number of surface analytical tools. The most frequently used techniques are fourier transform Infrared (FT-IR) spectroscopy,<sup>104,112</sup> ellipsometry,<sup>113</sup> studies of wetting by different liquids,<sup>114</sup> x-ray photoelectron spectroscopy,<sup>103,115</sup> and scanning probe measurement.<sup>116,117</sup> Typical organic molecules commonly used in this thesis are illustrated in Figure 2.1. The SAMs assembled on the silicon surface was investigated by FT-IR spectroscopy, ellipsometry, and AFM, respectively.

Figure 2-1. The structures and formula of silanes used in this thesis. Mercaptoundecyltrimethoxysilane (MUTMS), Undecenyltrichlorosilane (UTS), Octadecyltrichlorosilane (OTS) and Dodecyltrichlorosilane (DDTS)

## **2.2. Experimental part to prepare and characterize SAMs**

### **2.2.1. Instrumentation**

The SAM characterization was performed with the Agilent PicoPlus AFM in an environmental chamber. The imaging mode is primarily tapping mode with MikroMasch NSC-14 tips, which have a typical natural frequency of 150 kHz and a force constant of 5N/m. All AFM characterizations were performed in an

environmental chamber with 70% relative humidity (RH). The SAMs thickness on a surface was examined by Angstrom Advance PhE 101 ellipsometer. A varian Excalibur 3100 Fourier transformed infrared spectrometer equipped with a semiconductor cooled DTGS detector was used to check the surface properties.

### 2.2.1.1. Ellipsometry

Ellipsometry is a technique that determines the change of elliptically polarized state of light reflected from an interface, which separates two media with different indices of refraction. The elliptically polarized light is composed of two types of linearly polarized lights; the electric fields of p polarized light and the electric fields of s polarized light. The electric fields of p polarized light is parallel to the plane of incidence and the electric field of s polarized light is perpendicular to the plane of incidence. When an electromagnetic wave is reflected from a interface, it will change its phase and amplitude. Therefore, the amplitude and phase of p and s polarized light will be altered upon reflection, respectively. This will result in a change in the overall polarization of the light wave. Here, the phase shift  $\delta$  and amplitude change  $|r|$  depend upon the angle of incidence, refractive index (ratio of speed of light in vacuum to material), and extinction coefficient (penetration depth of light into material). The polarization change from the light reflected on a sample is measured by two parameters  $\Delta$  and  $\Psi$ . Here, the angle  $\Psi$  represents the ratio of the changes in amplitude for the s and p polarizations of light upon reflection from the interface. The angle  $\Delta$  is the difference in the phase shifts that are experienced by s and p polarization upon reflection, which can be expressed as equation (1) and (2).

$$\Delta = \delta_p - \delta_s \quad (1)$$

$$\tan \Psi = \frac{|r_p|}{|r_s|} \quad (2)$$

An ellipsometer measures the ratio  $p$  shown in equation (3), which is related to the Fresnel reflection coefficients  $R_p$  and  $R_s$  for p polarized and s polarized light.  $R_p$  and  $R_s$  are given by equation (4) and (5), respectively. Here, the ratio  $p$  is a

complex function of the angle of incidence, the wavelength, the optical constants, the ambient medium, and the layer thickness.

$$\rho = \frac{R_p}{R_s} = \tan \psi \exp(i\Delta) \quad (3)$$

$$R_s = \left( \frac{n_1 \cos \theta_i - n_2 \cos \theta_t}{n_1 \cos \theta_i + n_2 \cos \theta_t} \right)^2 \quad (4)$$

$$R_p = \left( \frac{n_1 \cos \theta_t - n_2 \cos \theta_i}{n_1 \cos \theta_t + n_2 \cos \theta_i} \right)^2 \quad (5)$$

Ellipsometry is an indirect way to obtain all the information of interest such as optical constant and thickness of a sample. The two parameters  $\Delta$  and  $\Psi$  can not be converted directly to the optical constants of the sample. The interpretation of the ellipsometry data is based on a model consisting of parallel interfaces separating air, the alkylsilane monolayer, and the substrate shown in Figure 2.2.

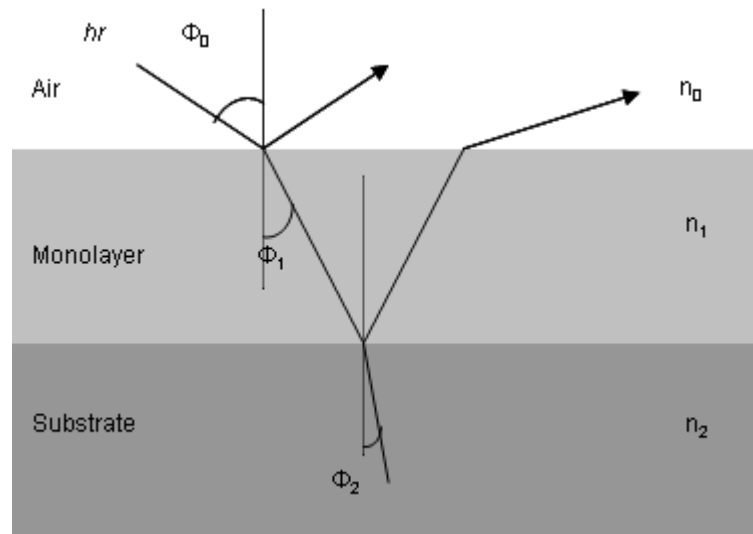


Figure 2-2. A two-layer model used for ellipsometry. The silicon substrate has refractive index  $n_2$  ( $\sim 3.8$ ), the alkylsilane monolayer on silicon has refractive index  $n_1$  ( $\sim 1.45$ ), and the ambient air has refractive index  $n_0$  assumed to be 1. The incident angle of the laser light  $\Phi_0$  is  $70^\circ$  (because of the higher sensitivity of ellipsometry under this angle). The angles of refraction  $\Phi_1$  and  $\Phi_2$  are  $40^\circ$  and  $15^\circ$  respectively, given by Snell's law ( $n_1 \sin \Phi_1 = n_2 \sin \Phi_2$ ).

We assume that the interfaces, monolayer-substrate and air-monolayer in the established model are isotropic and homogeneous. Moreover, each individual layer has a uniform optical constant. The thick substrate has a refractive index  $n_2$ , the monolayer has a refractive index  $n_1$ , and the ambient atmosphere has refractive index  $n_0$  (which is assumed to be 1). In principle, ellipsometry can determine both the thickness and the refractive index of a monolayer through an iterative procedure. It was reported that the thickness of these n-alkylsiloxane monolayer on a substrate corresponds very closely to those which we expect for a trans-extended chain oriented perpendicularly to the surface. This also agrees with the infrared measurements. Therefore, with a plausible optical constants and thickness,  $\Delta$  and  $\Psi$  values are calculated using the Fresnel equation. The calculated  $\Delta$  and  $\Psi$  values which match the experimental data at their best, provide the optical constants and thickness information of the sample. An ellipsometer can measure layers as thin as 1nm and up to several microns thick. Applications of ellipsometer include the accurate thickness measurement of thin films, the identification of materials or thin layers and the characterization of surface. The principle of the operation of a laser ellipsometer is showed in the Figure 2.3.

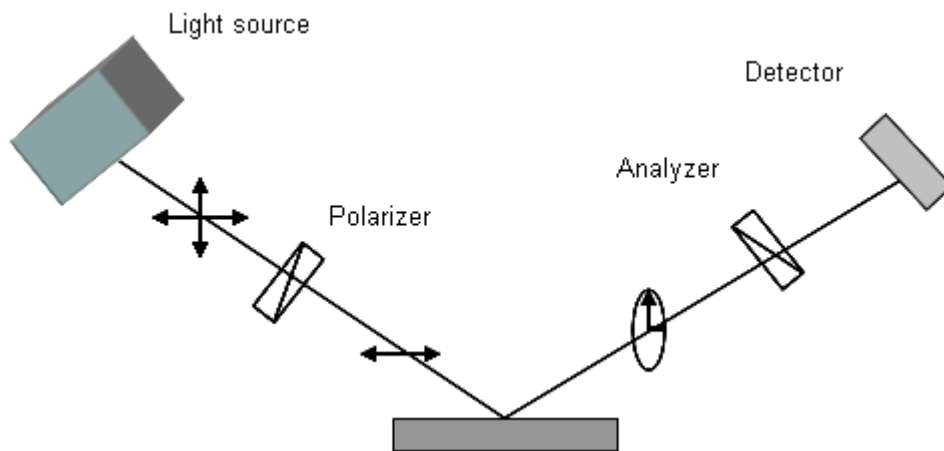


Figure 2-3. The layout of laser ellipsometry measurement system

It consists of a laser (commonly a 632.8nm helium/neon laser), a polarizer, an analyzer and a detector. The polarizer can provide a state of polarization which can be varied from linearly polarized light to elliptically polarized light to

circularly polarized light by varying the angle of the polarizer. When a beam is reflected off the layer on a surface, it will be analyzed by an analyzer. The operator changes the angle of the polarizer and analyzer until a minimal signal is detected. The minimal signal is obtained when the light reflected by the sample is linearly polarized. The analyzer is set so that only light with s polarization which is perpendicular to the incoming polarization is allowed to pass. Now, the measured angles from polarizer and analyzer are related with the two parameters  $\Delta$  and  $\Psi$ . Combined with the established model, a couple of  $\Delta$  and  $\Psi$  pairs measured for different places on a surface, can determine the thickness of the layer on the top.

Because ellipsometry measures the ratio of two values, it is highly accurate and reproducible. It measures phase and thus is very sensitive to the presence of ultrathin films. Meanwhile, it doesn't need a reference sample, and measurement is non-destructive to the sample surface.

#### **2.2.1.2. Fourier transform infra-red (FT-IR) Spectrometry**

Infrared spectroscopy is a widely used technique for material analysis in a research laboratory. As we know, an infrared spectrum measures the absorption frequencies which are corresponding to the vibration between the bonds of the atoms making up the material. Additionally, the size of the peaks in the spectrum is a direct indication of the amount of material present on the surface. Therefore, infrared spectroscopy has the capability to identify every different material, and quantify them from the corresponding infrared spectrum specified as a plot of intensity vs. frequency.

The traditional IR instrument is dispersive style, which uses a prism or grating to separate the individual frequency of energy emitted from the infrared source. Then, the detector measures the amount of IR energy at each frequency which has passed through the sample one by one and is summed up to draw the spectrum. Generally, it needs minutes to finish one sample measurement. Fourier Transform Infrared (FT-IR) spectrometry was developed to overcome the limitations encountered with the traditional dispersive instruments such as slow



scanning process and low sensitivity. A method for measuring all of the infrared frequencies simultaneously instead of individually was implemented by using interferometer. An interferometer produces a unique type of signal which has all of the infrared frequencies included through employing a beamsplitter. The beamsplitter takes the incoming infrared beam and divides it into two optical beams. One beam reflects off a mirror which is fixed in place, and the other beam reflects off a moved mirror with a very low speed. After the two beams experienced their reflection path respectively, they are recombined as meeting back at the beamsplitter. It is because that one beam travel is a fixed length and the other is constantly changing as its mirror moves, the signal which exits the interferometer is the result of these two beams interfering with each other. The resulting signal is called an interferogram which contains every infrared frequency generated in the source. This means that as the interferogram is measured, all frequencies are being measured simultaneously. Thus, the use of the interferometer results in extremely fast data collection and signal measurement, usually on the order of one second or so rather than several minutes. However, the measured interferogram signal can not be interpreted directly by us. A readable frequency spectrum represented as a plot of the intensity at each individual frequency is required to analyze the sample of information. FT-IR then uses Fourier transformation mathematical technique to decode the individual frequency and accomplish the whole process with the help of a computer. The sensitivity of FT-IR can also be improved through co-adding the one second scans together to ration out random noise. Figure 2.4 shows the layout of FT-IR measurement system.

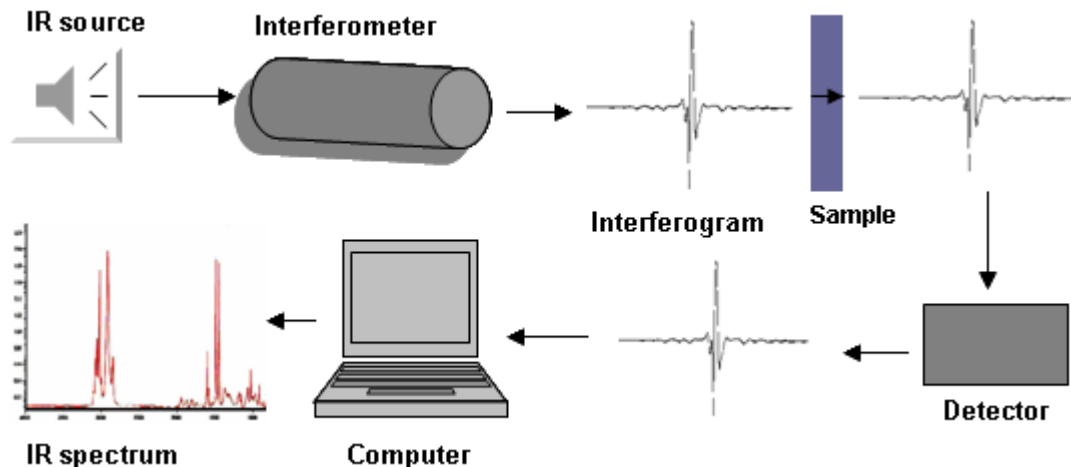


Figure 2-4. The layout of FT-IR measurement system

The FT-IR in my lab is equipped with a DTGS detector. There is an IR UMA 600 microscope attached to the FT-IR spectrometer, which is equipped with a liquid nitrogen cooled mercury cadmium telluride (MCT) narrow band detector. In addition, a computer-controlled shuttle to transfer samples to the designated positions is built in the sampling chamber of the IR spectrometer. The advantage of the shuttle is that more than one sample can be placed on the different sample holders in the sampling chamber at the same time and can be continuously checked without any interruptions during the experiment. In contrast to the traditional way, this setup can save us time on waiting for another nitrogen environment in the chamber every time a new sample is introduced. Furthermore the different background signals could be collected in the same environment as the sample. In total, there are seven sample holders in the IR chamber, setting at an angle of incidence of  $73.7^\circ$  to mount the IR transparent Si wafers, separately. The angle here is Brewster's angle also known as polarization angle, which is from the Brewster's law shown as equation (6).

$$\theta_B = \arctan\left(\frac{n_2}{n_1}\right) \quad (6)$$

Here,  $n_1$  and  $n_2$  are the refractive indices of the two media. So, the IR instrument used in our lab is also called Brewster's angle FT-IR, which is used to characterize the SAMs grown on silicon wafer. Because the refractive index of Si

is 3.42, if the air refractive index is assumed to be 1, the Brewster's angle is  $73.7^\circ$  for a silicon media in the air. The IR measurement is performed in the Brewster's angle configuration because the reflection of the IR beam at the front and back Si-air interfaces generates intense interference in such thin wafers, as shown in Figure 2.5a. When this interference is measured with the real signal, it will obscure the spectral contribution of the organic surface film of interest. This problem is solved by using a p-polarized IR beam incident on the surface at the Brewster's angle, which is shown in Figure 2.5b. The Brewster's angle can be understood that only the s polarized light can be reflected and the p polarized light perfectly refracted as an incidence with the specific angle  $\Phi_B$  ( $\Phi_B = \arctan(n_2/n_1)$ ) encounters an interface, which separates two media with different refractive index. Figure 2.5a and 2.5b show the two situations when a p-polarized IR beam incidence encounters an interface with a random angle and a Brewster's angle, respectively. Therefore, with a Brewster's angle FT-IR, the IR spectrum with only sample information in it will be collected by the detector. Instead, the intense interference signals originated from the continuous reflection on the silicon surface will be avoided. The incident ray with a random angle is supposed to both generate reflection and refraction on the front silicon-air interface in Figure 2.5a. However, the IR instrument used in our lab takes only transmission spectra, and thus a simplified scheme is provided here.

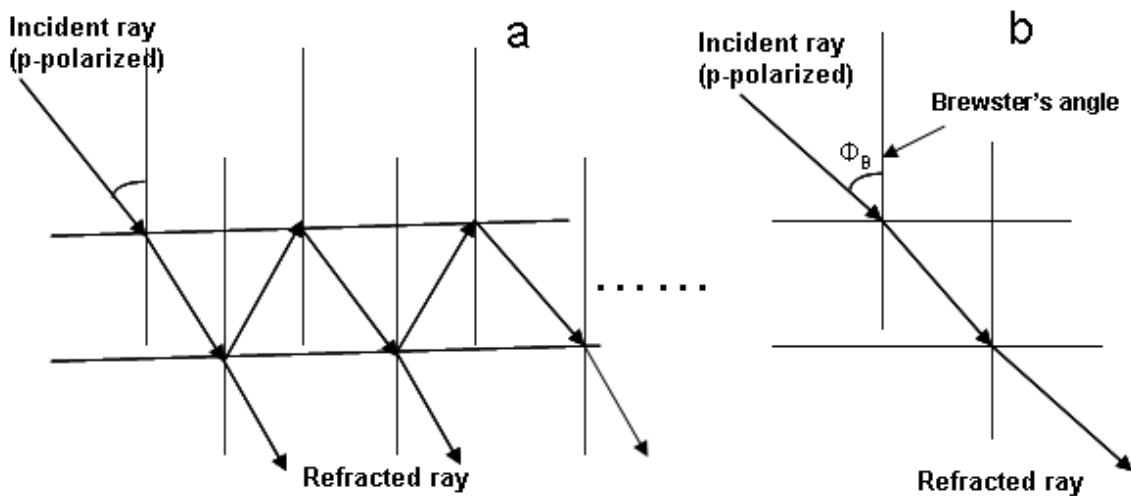


Figure 2-5. The illustration of a p-polarized IR beam incident encounters an interface with: (a) a random angle; (b) Brewster's angle

## **2.2.2. Preparation of the Self-assembled monolayer on Si(100) wafer**

### **2.2.2.1. Materials**

(100) silicon wafers are nitrogen doped, each having a resistivity of 5 ohm.cm. Octadecyl-trichlorosilane (OTS, 97%) is from Gelest. Toluene (HPLC grade) is from SigmaAldrich. All chemicals are used without further purification. All aqueous solution were prepared with water from a Narnstead NANoPure water purification system with normal resistivity of 18.2 MΩ cm

### **2.2.2.2. Experimental procedure to prepare SAMs**

(100) silicon wafers were cut into  $1 \times 1 \text{cm}^2$  pieces and rinsed with distilled water. After the wafers were dried in a flow of air, they were then boiled in the piranha solution (one part of 30% hydrogen peroxide solution in two parts of 98% sulfuric acid) for 20 minutes at 120-125°C to grow a fresh oxide layer. This solution is an extremely potent oxidant. It removes organic impurities from the substrate and also helps to grow a thin oxide layer of silanol (Si-OH) groups on the top. Once the solution cooled down to room temperature, these wafers were rinsed, and kept in the distilled water for future uses. The silanol groups created a hydrophilic surface on top of the wafers. After being rinsed in deionized water and dried in a stream of nitrogen, the cleaned wafers were dipped in a 5mM octadecyltrichlorosilane (OTS) toluene solution to start the adsorption reaction. During the 10 hours' incubation, the surface-bound water hydrolyzes the Si-Cl bonds to form Si-OH groups, which undergo condensation reaction to cross-link and bind with the substrate or with the adjacent alkyl silane molecules through Si-O-Si bonds. The formation of OTS monolayer on a silicon wafer is illustrated in Figure 2.6.



Figure 2-6. Schematic representation of the formation of octadecyltrichlorosilane (OTS) monolayer by adsorption of OTS molecules from solution onto silanol (Si-OH) groups covered on silicon wafer substrates

#### 2.2.2.3. The characterization of OTS film on silicon wafer

Here, AFM (Picoscan 3000; Agilent Technologies), FT-IR(Varian Exalibur 3100), and Ellipsometer (PHE-101) were used to characterize the silane adsorption after the overnight soaking in the OTS toluene solution. AFM and FTIR are capable of determining the surface properties of SAMs, such as roughness, adsorption mechanism, and surface properties. AFM topography and phase image in Figure 2.8 shows that OTS molecules formed a featureless and homogenous film on the silicon surface. The highly oriented and densely packed OTS film was very flat. It was demonstrated that the height variation was smaller than 5nm over the AFM scanner's range ( $90 \times 90 \mu\text{m}^2$ ). FTIR spectra in the C-H stretching region of OTS adsorbed on Si(100)/SiO<sub>2</sub> is shown in Figure 2.7. Methylene (-CH<sub>2</sub>) and methyl (-CH<sub>3</sub>) asymmetric and symmetric C-H bands are observed, which suggests the OTS adsorption on the surface. The peaks at 2918 cm<sup>-1</sup> and 2850 cm<sup>-1</sup> arise from the methylene (-CH<sub>2</sub>) asymmetric and symmetric stretching, respectively. Methyl (-CH<sub>3</sub>) asymmetric and symmetric stretching feature at 2965 cm<sup>-1</sup> and 2880 cm<sup>-1</sup>, respectively. The results are in close agreement with the FTIR spectra results of OTS layer, which is highly ordered

and densely-packed monolayer with perpendicular chain axis orientation.<sup>118,119</sup> The ellipsometry results indicated that the OTS film thickness was  $26\pm 3\text{\AA}$ , which was consistent with the published result as well.<sup>102</sup>

The peaks on  $2918$  and  $2850\text{ cm}^{-1}$  associated with  $-\text{CH}_2$  asymmetric and symmetric stretching in FT-IR spectra can also indicate the microstructure of SAMs arrangement on silicon wafer through their full width at half height (FWHH). It has been reported that a liquid-like state of paraffinic chains on surfaces was shown to be accompanied by a considerable broadening of the H-C-H stretch bands and quite blue-shift position of  $2924\text{ cm}^{-1}$  (FWHH above  $28\text{ cm}^{-1}$ ) and  $2854\text{ cm}^{-1}$  (FWHH above  $17\text{ cm}^{-1}$ ), respectively.<sup>120</sup> In comparison, the different peak position and relatively low corresponding FWHH as  $2918\text{ cm}^{-1}$  (FWHH ca.  $13.3\text{ cm}^{-1}$ ) and  $2850\text{ cm}^{-1}$  (FWHH ca.  $10.1\text{ cm}^{-1}$ ) from my results confirm that OTS molecules are packed in an ordered, solid-like arrangement on silicon surface.

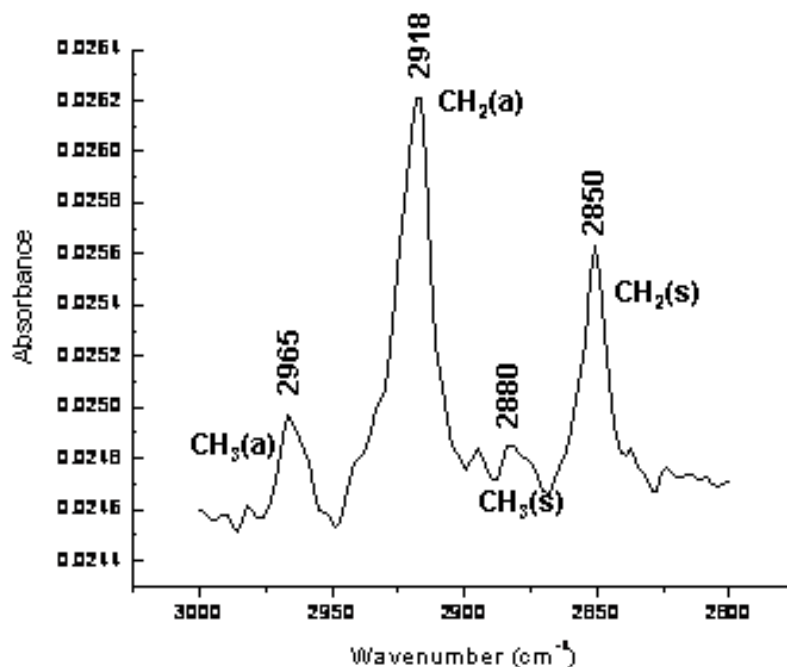


Figure 2-7. FTIR spectra in the C-H stretching region of Si(100)/SiO<sub>2</sub> with OTS adsorption showing  $-\text{CH}_2$  and  $-\text{CH}_3$  stretching bands

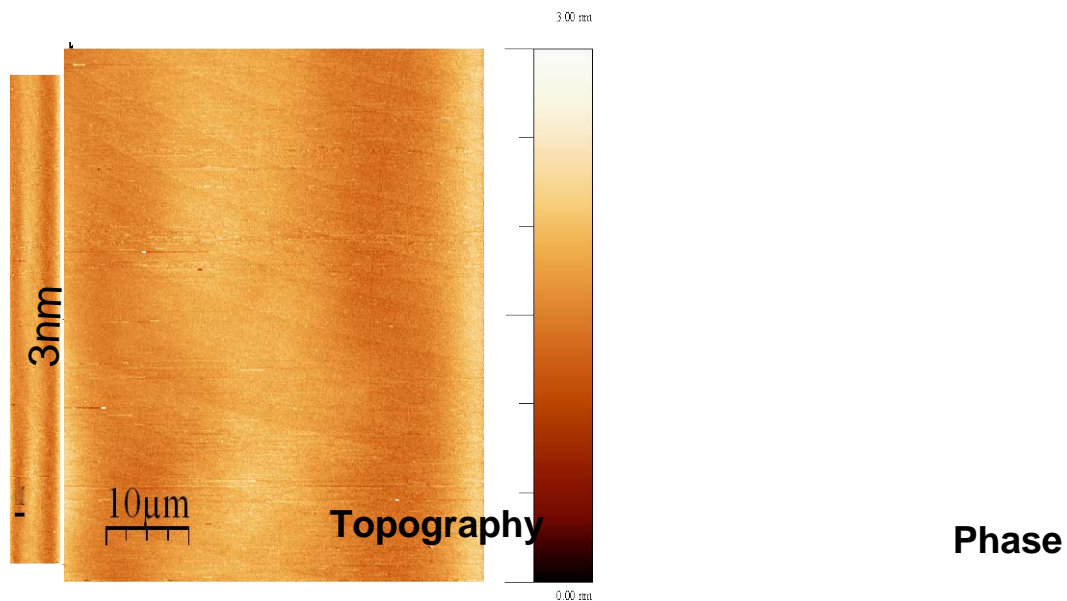


Figure 2-8. AFM image in the 50×50 µm<sup>2</sup> area showing the OTS layer is a feature and homogenous film on the silicon surface.

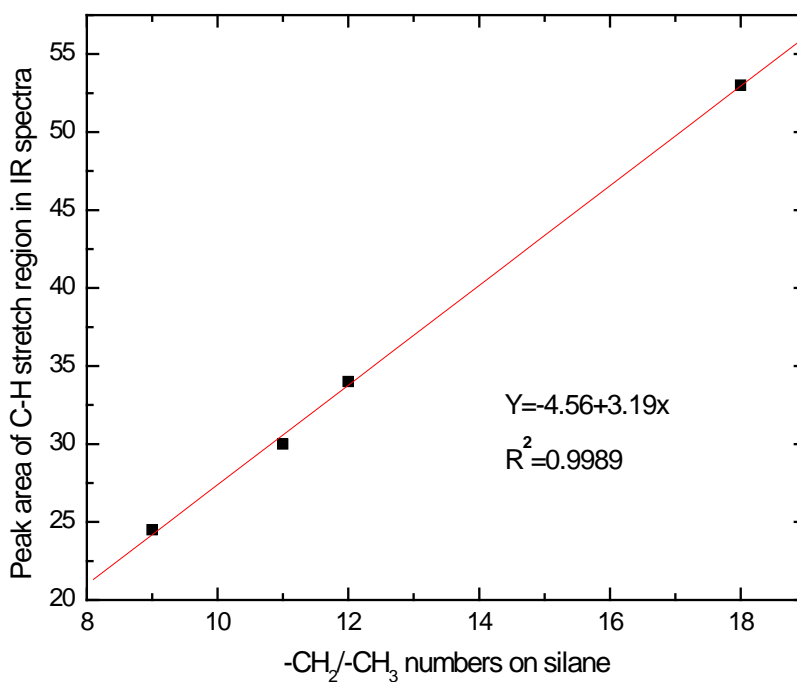


Figure 2-9. The plot of the C-H stretch bands region area in the Brewster's angle IR spectra of different silanes with methylene and methyl group numbers in the corresponding silane molecule

While OTS SAMs were formed on Si(100)/SiO<sub>2</sub> wafer surface, mercaptoundecyltrimethoxysilane (MUTMS), undecyltrichlorosilane (UTS), and dodecyltrichlorosilane (DDTS) SAMs were prepared through the same dipping method in our lab. Through the direct characterization from AFM and ellipsometry, it has been demonstrated that they all form a very thin and homogenous film on Si(100)/SiO<sub>2</sub> wafer surface. With different surface properties, they provide us a good substrate to manipulate on the top through either direct chemical way or indirect surface lithography way. All the SAMs related experiments will be discussed in the following chapters. In addition, the relationship between the C-H stretch bands region area in the Brewster's angle IR spectra of different silanes, and methylene and methyl group numbers in the corresponding silane molecule, is plotted in Figure 2.9. From the well-fitted linearity, we can conclude that FT-IR is a good technique to quantitatively indicate the amount of absorbed hydrocarbon material on the surface through measuring the C-H stretch bands region area in the Brewster's angle IR spectra.

### **2.3. Conclusion of chapter 2**

A very flat and homogeneous SAMs film was grown on Si(100)/SiO<sub>2</sub> wafer surface through the 10 hours' incubation in the different silane solutions for the cleaned wafers. Based on this method, OTS, UTS, MUTMS and DDTS SAMs on Si(100)/Si surface have been prepared in our lab. The various surface properties of SAMs such as the layer thickness, roughness, and chemical identity have been investigated by FT-IR, AFM, and ellipsometry, respectively. It was demonstrated that SAMs are a good substrate for the future patterning techniques to assemble protein molecules in our lab.



## CHAPTER 3

### AFM LOCAL OXIDATION LITHOGRAPHY

#### 3.1. Introduction

Working with a sharp conductive AFM tip and self-assembled organic monolayer on surfaces, people have developed the local oxidation lithography techniques. The local probe oxidation has been extensively used to fabricate chemical patterns on surfaces since it was invented. Chemical patterns created through this method were used to control the adsorption, shape, and size of molecules at mesoscale.<sup>121-124</sup>

Basically, a bias is applied between a conducting AFM probe and silicon substrate, and either a positive or a negative topographic feature is fabricated under the probe. The local probe oxidation conducted on a bare silicon surface generates SiO<sub>2</sub> positive pattern underneath of the probe.<sup>125,126</sup> The size and the height of the pattern are functions of the oxidation voltage and oxidation dwell time, which have been investigated in the literature.<sup>127-130</sup> If a bias is applied on the alkanethiol self-assembled monolayer grown on a single crystal gold surface, a negative topography pattern is created through the destructive desorption of the alkanethiol molecules by the local probe oxidation.<sup>131</sup> A more complicated situation could happen on the alkanethiol SAMs grown on a gold film coated silicon wafer. Depending on the alkanethiol terminal functionalities and the alkyl chain length, the pattern generated can be either a negative pattern or a positive pattern, respectively. The production of different topographic features on the surface depends on the growth of SiO<sub>2</sub> after the desorption of the alkanethiol molecules.<sup>132</sup>

A similar reaction pathway happens on a silane coated silicon wafer surface. Both a positive topography pattern<sup>133,134</sup> and a zero-contrast topography pattern have been reported regarding to the oxidation in a dry or an ambient humid environment.<sup>135,136</sup> The oxidation of a silane film in a dry environment yields oxide, whereas oxidation under an ambient relative humidity only oxidizes

the terminal methyl group of silane, which is an incomplete oxidation process called “constructive lithography”. In this method, only the terminal group is oxidized, and the growth of SiO<sub>2</sub> is negligible, thus, the patterns generated have no apparent topography change on the substrate.<sup>68,135,137-139</sup> The oxidation of OTS has been reported in the literature, which involves two processes to determine the final topographic change of patterns.<sup>136,140</sup> One is the degradation of the OTS film and the other is the growth of SiO<sub>2</sub> underneath the film. As a result,, the final pattern height is the summation of these two processes. In the case of conductive lithography, the oxide growth process is negligible under incomplete oxidation conditions. Therefore, the conducting AFM probe only oxidizes the terminal methyl group of the OTS molecule on silicon surface, converting the methyl group to carboxylic acid group (OTS<sub>ox</sub>). The constructive lithography generates patterns with almost no apparent topography change on OTS surface.<sup>135</sup>

It is generally agreed that the degree of oxidation causes these difference: incomplete oxidation only converts the terminal group of the silane film, while complete oxidation causes silane desorption from the substrate and the growth of SiO<sub>2</sub>. Here, OTSpd pattern is first introduced by our group, which involves the third possibility in the oxidation process of OTS SAMs on silicon wafer: the silane is partially degraded and stays on the surface after the oxidation. Using the setup illustrated in Figure 3.1 which is same as that used by the Sagiv group, but in 100% relative humidity instead, our data show that OTS molecules are partially degraded and stay on the surface. It was proven that the terminal methyl group was converted to carboxylic acid group which can attract different protein molecules through electrostatic interaction from protein solutions. AFM images show the OTSpd pattern is 10.2Å lower than the OTS film, which is different from the zero topography contrast OTS<sub>ox</sub> patterns. Also, it was proven that the OTSpd pattern can even grow very well beyond the contact area of the AFM probe in this method. So, by controlling the voltage and dwelling time of AFM tip on the surface, we can fabricate such OTSpd pattern ranging from ~18nm to submillimeter in size which is even beyond the piezo scanner’s range.

## **3.2. Experimental of AFM local oxidation lithography**

### **3.2.1. Material**

Silicon (100) wafers are nitrogen doped, with a resistivity of 13  $\Omega\text{cm}$ , were purchased from James Rive Semiconductors. The wafers were polished to the ultra-flat level with a root mean square (RMS) roughness smaller than 5 Å. Octadecyltrichlorosilane (OTS, 97%) and 10-undecenyltrichlorosilane (UTS, 97%) were from Gelest. Chloroform (HPLC grade, for residue analysis) were obtained from Mallinckrodt Baker. Toluene (HPLC grade) was purchased from Sigma-Aldrich. 1-Pyrenyldiazomethane (PDAM) was from Invitrogen. All chemicals were used without further purification. All aqueous solution were prepared with water from a Narnstead NANoPure water purification system with normal resistivity of 18.2 M $\Omega$  cm

### **3.2.2. Instrument**

The chemical pattern fabrication and characterization were operated with the Agilent PicoPlus AFM in an ambient environment. The chemical pattern was fabricated in the contact mode with MikroMasch CSC17 Ti-Pt coated AFM tip. The patterns were characterized in the tapping mode with MikroMasch NSC-14 tips, which have a typical natural frequency of 150 kHz and a force constant of 5 N/m. The fluorescent image was obtained by Nikon Eclipse N55i Microscope.

### **3.2.3. Fabrication and characterization of OTSpd chemical patterns**

In this thesis research work, all the substrates are self-assembled monolayer of octadecyltrichlorosilane (OTS) on Si (100) wafer. A platinum-titanium-coated conductive tip was installed on the Agilent PicoPlus AFM and operated in the contact mode. As the tip was in contact with the OTS film, a bias was applied between the Si (100) wafer and the conductive AFM tip. In the 100% humid environment (at 25°C), the OTS film under the AFM tip could be partially destructed, forming a partially degraded, carboxylic acid-terminated pattern (OTSpd) under this oxidation process.

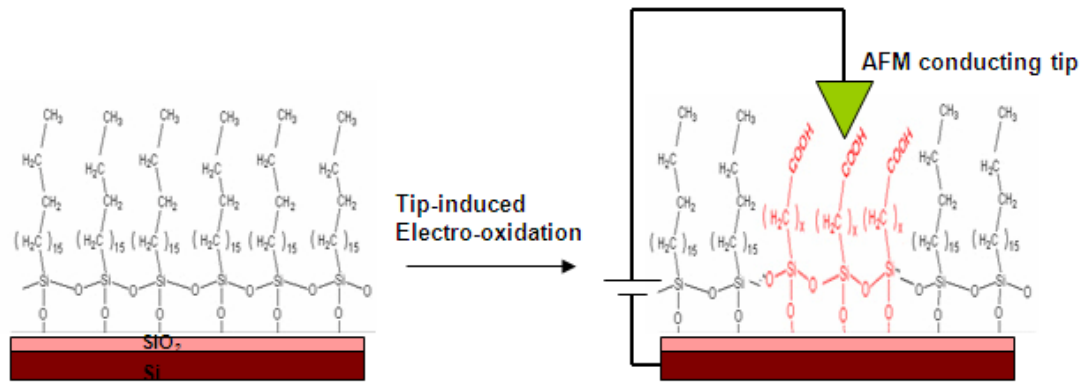


Figure 3-1. Schematic view of AFM local oxidation lithography: conductive AFM tip induced electrooxidation of top methyl functional group of octadecyltrichlorosilane (OTS) on the silicon wafer to carboxylic acid group in the 100% humid environment at 25°C.

From the AFM image, we can see the OTSpd pattern is lower than OTS background, as shown in Figure 3.2. The image was acquired under a 50mM PBS buffer to avoid the charge interaction between the AFM tip and the surface. The peak of the disk center is composed of silicon dioxide. The oxidation of a silane film is the function of humidity, voltage, and dwell time. The size of the OTSpd patterns is controlled by the duration of the bias voltage. The longer the bias voltage, the bigger the disc is. By controlling the duration of the voltage, the pattern can be fabricated from 18nm to submillimeter in size. Figure 3.2c shows the friction channel image of two thin lines fabricated by the AFM probe oxidation, where the line width is 18nm. Figure 3.2b is the histogram of Figure 3.2a. From the histogram, we measured the apparent height of OTSpd to be  $9 \pm 3 \text{ \AA}$ , and the apparent height of OTS film is  $20 \pm 2 \text{ \AA}$ . Thus, the OTSpd pattern is  $11 \pm 4 \text{ \AA}$  lower than the OTS background. The image (a) was acquired under a 50mM phosphate buffered saline (PBS) buffer. The same area was also scanned from different directions. The depth values of the OTSpd pattern from different scanning directions were consistent, indicating that the topography-friction crosstalks were minimal.

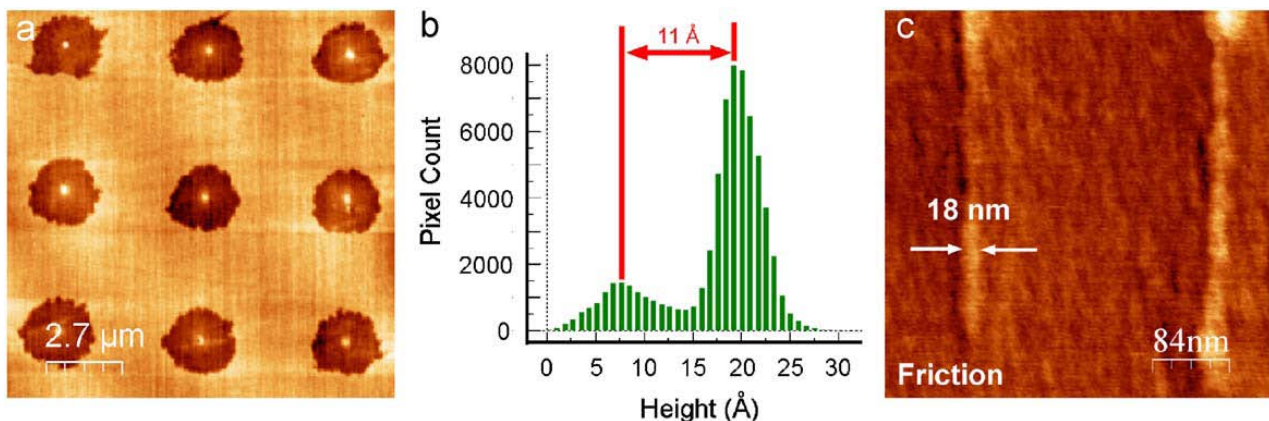


Figure 3-2. (a) A 3×3 array of OTSpd disc-shaped pattern fabricated on the OTS surface. (Topography, AC mode) (b) The height histogram of (a) shows that the OTSpd pattern is  $11\pm 4\text{Å}$  lower than the background. (c) Two lines were fabricated using the AFM probe oxidation on the OTS film. The line width is 18nm. (Contact mode, friction channel.)

In addition, we used PicoLith software to control the moving direction and speed of AFM tip, which can determine if the linear or disc shaped patterns would be fabricated. A stationary tip created disc-shaped patterns, while a moving tip created linear patterns. Because the design of the PicoLith software determines the AFM tip always be halted briefly before changing direction during the pattern writing process, the joints between two lines always appear as round discs. The AFM image in Figure 3.3a shows the linear OTSpd pattern created by AFM local lithography. In Figure 3.3b, the height cross-sectional profile along the line in Figure 3.3a illustrated that depth of OTSpd pattern is around  $10.2\text{Å}$ , which is consistent with the value measured before. These finished chemical patterns were used as templates to direct the assembly of lysozyme molecules and define the shape and dimension of the protein pattern.

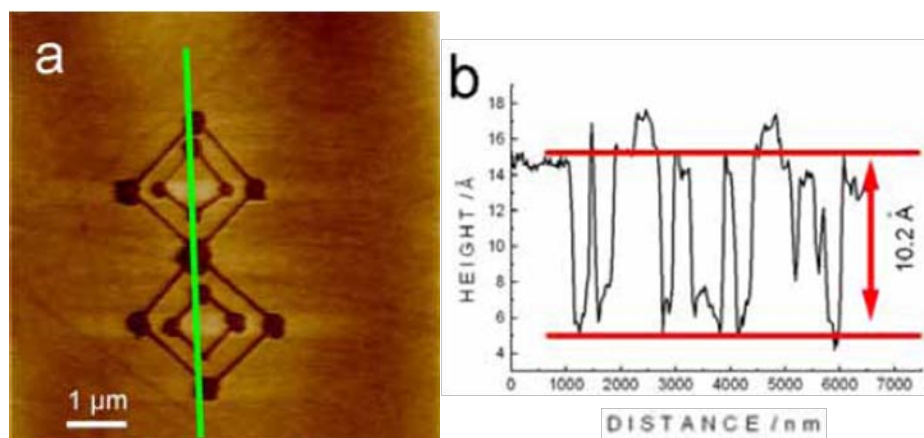


Figure 3-3. (a) The topography image of the OTSpd pattern on OTS monolayer of silicon surface. (AC mode) (b)The height cross-sectional profile along the green line in (a) shows the depth of OTSpd pattern is 10.2 Å.

### 3.2.4. The identification of OTSpd pattern

It is known that 1-Pyrenyldiazomethane (PDAM) can specifically react with the carboxylic acid group to form an ester product and generate fluorescence upon excitation. The schematic equation about this reaction is illustrated in Figure 3.4. Therefore, PDAM was directly used as a fluorescence-labeling reagent to identify the chemical properties of OTSpd patterns.<sup>141</sup> The binding of OTSpd patterns with PDAM has been visualized in our lab by AFM and fluorescent microscope, respectively.<sup>122</sup> It was demonstrated that the OTSpd pattern grew to the same height as OTS background after the binding with PDAM. The fluorescent microscope image showed the pattern area on the surface has fluorescence signal but with relatively low resolution.

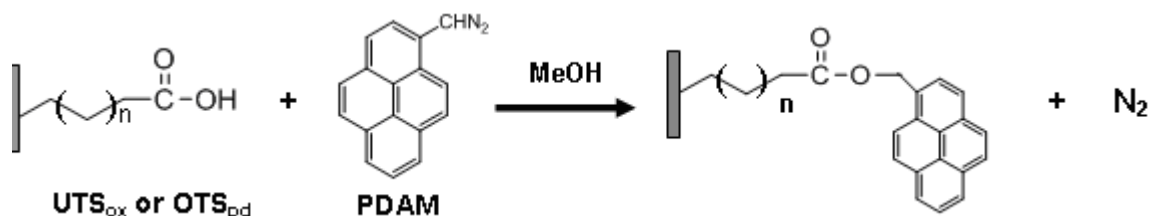


Figure 3-4. The schematic reaction of PDAM with carboxylic acid group on OTSpd and UTSox

To further prove that the fluorescence signal on the surface is from carboxylic acid group, an experiment was designed to prove the chemical properties of OTSpd surface by comparing its fluorescence signal with that from UTSox patterns. It has been demonstrated that double bond terminal group on undecenyltrichlorosilane (UTS) can be converted to carboxylic acid group through chemical way.<sup>101,142</sup> To confirm the conversion of UTS molecules on surfaces, a UTS monolayer on a 2.5cm×2.5cm silicon wafer was prepared, which follow the same procedure as the OTS monolayer preparation. Next, the UTS-coated silicon wafer was incubated in the oxidizing solution (0.01M NaIO<sub>4</sub>, 5×10<sup>-4</sup> M KMnO<sub>4</sub>, in 0.05M Na<sub>2</sub>CO<sub>3</sub> buffer) for 10h at 40°C. The sample was then rinsed with deionized water and followed by 1% Hydrazine for 1 min. Finally the sample was dried in a stream of nitrogen. In the Brewster angle IR spectra of the UTS wafer before and after oxidization in Figure 3.5, we can see the 3080 and 1645 cm<sup>-1</sup> peaks of the vinyl group disappear and a new peak at 1710cm<sup>-1</sup> appears, which corresponds to the carboxylic acid group. It can be concluded that the double bond was converted into carboxylic acid group after this oxidation process. The chemical reaction was shown in Figure 3.6.

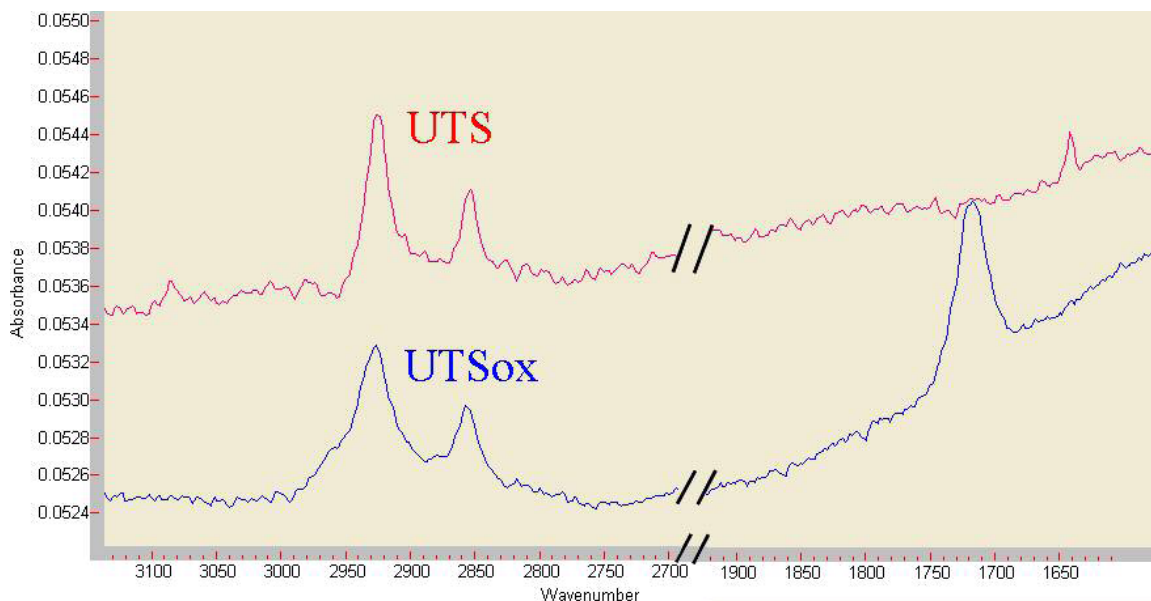


Figure 3-5. The Brewster angle IR spectra of the UTS monolayer (red) and the oxidized UTS (UTSox, blue) monolayer. The peak at  $1710\text{ cm}^{-1}$  of UTSox indicates the vinyl group of UTS is converted into the carboxylic acid group after the oxidation.

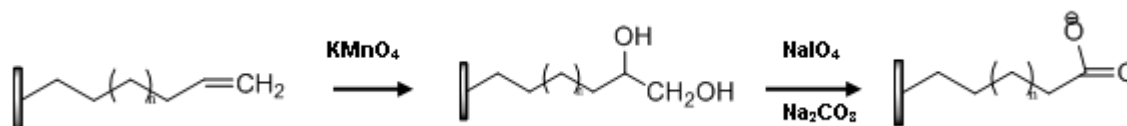
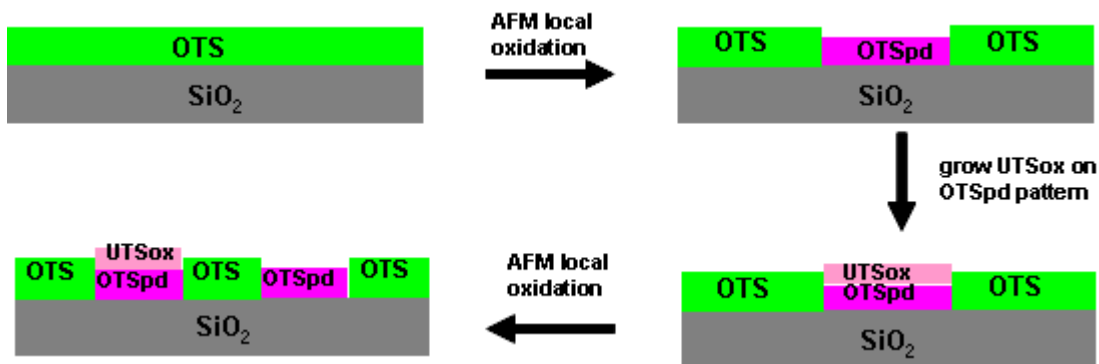


Figure 3-6. The oxidation process of undecenyltrichlorosilane (UTS) to UTSox

In this experiment, OTSpd and UTSox patterns are fabricated in  $50 \times 50\mu\text{m}^2$  of OTS surface area, respectively. The patterned sample was checked with fluorescence microscope after being incubated in 3mM PDAM methanol solution. Through direct comparison with UTSox, the chemical properties of OTSpd can be identified. Our experiment procedure is illustrated in Schemes 3.1. The carboxylic acid-terminated OTSpd patterns were first fabricated through the AFM local oxidation lithography in the contact mode in a humid environment. Subsequently, the pattern was incubated in a 5mM UTS toluene solution overnight. The UTS silane self-assembled on the hydrophilic OTSpd pattern, forming a second layer, which was double bond terminated on the top. Following the same oxidation method, the UTS layer on the OTSpd surface was converted



to UTSox layer. Next, some new OTSpd patterns were fabricated around the UTSox-OTSpd patterns on the OTS film. The sample was then dipped into 3mM PDAM methanol solution to start the reaction. After 10 hours of incubation, the sample was rinsed and ultrasonicated in methanol. When the sample was dried with a stream of Nitrogen gas, it was checked with fluorescence microscope.



Scheme 3-1. The fabrication of OTSpd and UTSox patterns in  $50 \times 50 \mu\text{m}^2$  of OTS surface area: OTS (green) is oxidized to OTSpd (pink) through the AFM local oxidation lithography. Next, the OTSpd pattern is reacted with UTS, to form a double bond terminated OTSpdUTS pattern. The OTSpdUTS pattern is then oxidized to a COOH-terminated OTSpdUTSox pattern (light pink). Next, another OTSpd pattern is fabricated around the OTSpdUTSox pattern.

From the fluorescence microscope image in Figure 3.7, we can see the patterned area is much brighter than the background area due to the fluorescent signal from PDAM covered on OTSpd and UTSox patterns. The bigger round disc on the surface is OTSpd pattern and the smaller ones are UTSox patterns. From the image, we can also see that the OTSpd pattern has a similar fluorescent signal as that from UTSox patterns which are terminated with carboxylic acid groups on the top, and this has been demonstrated by FT-IR spectroscopy. From this comparison, it can be concluded that OTSpd pattern is a carboxylic acid group terminated pattern. Furthermore, not only PDAM can identify the chemical properties of OTSpd surface, but also it has been used as a quantitative method to measure the amount of carboxylic acid group.<sup>143</sup> Based on the two ways to fabricate carboxylic acid terminated patterns in our lab: one is

AFM local oxidation lithography which uses a conductive AFM tip to partially degrade OTS molecules on the surface but with unknown oxidation process; the other one is the chemical method to convert double bond to carboxylic acid group through oxidant with a clear reaction mechanism, we can compare the carboxylic acid group coverage on OTSpd and UTSox patterns through the fluorescence signal quantitatively generated from the bound PDAM. The information from the comparison is expected to help us to better understand the AFM local oxidation process. The experiment is ongoing in our lab, and more data will be presented in chapter 8.

In a parallel experiment, the middle part of OTSpd surface was confirmed to be  $\text{SiO}_2$ . We fabricated an OTSpd patterns as shown in Figure 3.2. Then, the pattern was reacted with a 1% HF solution for 5 minutes, and imaged again after being rinsed with deionized water. It was found that the center “peaks” in the disc patterns changed to deep holes after the HF treatment, while other parts of OTSpd pattern remain intact. This indicated that the middle part of OTSpd pattern is composed of  $\text{SiO}_2$ , which can be etched away by HF solution. However, the remaining part of OTSpd pattern was protected by an organic layer from the HF etching, which is the partially degraded OTS layer. And thus, the OTSpd layer still remained  $10\text{\AA}$  below OTS background.

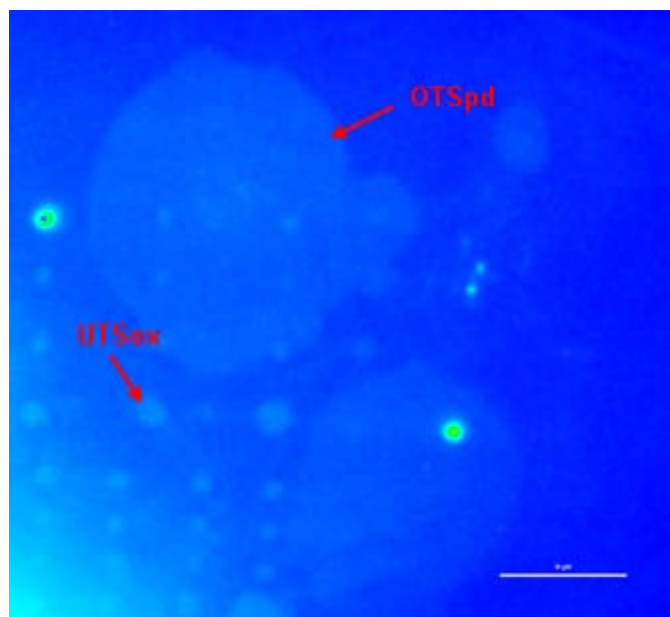


Figure 3-7. The fluorescence microscope image of OTSpd (big patterns) and UTSox (small pattern) patterns on OTS surface

In the experiments of determining the OTSpd depth and the OTSpd chemical identity, we conclude that OTSpd is a degraded silane layer with carboxylic acid groups terminated. Based on the data collected, we deduce that there are two simultaneous processes in the whole oxidation process: the degradation of the silane film, which decreases the pattern height, and the silicon oxide growth, which increases the pattern height. It was speculated that these two opposite processes reached equilibrium when the height of OTSpd was  $10\text{\AA}$  lower than OTS surface. It is known that the projection of carbon-carbon bond onto the surface normally ( $z$  axis) is  $1.26\text{\AA}$  for a trans-extended chain on surfaces.<sup>142</sup> Therefore, the  $10\text{\AA}$ -depth roughly corresponds to the dimension of eight  $\text{CH}_2$  units. However, this doesn't mean that there are exact eight  $\text{CH}_2$  units truncated from the OTS backbone in the local probe oxidation process. To explain, there are two situations we need to consider: firstly, the  $\text{SiO}_2$  underneath the probe might grow thicker after the local oxidation; secondly, the tip contact area is around  $10\times 10\text{nm}^2$  or larger in the AFM measurement, which means the height measured from AFM can not tell the surface feature to a signal. When tall and short molecules mixed, AFM can only detect the tall molecules because of the tip size. Therefore, the

AFM data only suggests that the oxidation process truncated at least eight CH<sub>2</sub> units from the OTS backbone. The mechanism of AFM local oxidation process needs to be further investigated.

### **3.3. Conclusion of chapter 3**

A new patterning method, AFM local oxidation lithography, has been created in our lab. Through this oxidation method, hydrophilic OTSpd patterns ranging from ~18 nanometer to submillimeter in size could be fabricated on OTS surface. OTSpd is carboxylic acid-terminated and around 10Å below the OTS background, which came from the partial degradation of OTS molecule in the oxidation process. It was demonstrated that the surface is converted to oxide during the local probe oxidation in low humidity environment. Under ambient humidity and fast moving speed, only the terminal group of OTS molecule is converted to carboxylic acid group, and the fabricated pattern OTSox has no topographic contrast with OTS background. However, in our new patterning method, the partially degraded OTSpd pattern with 10Å height contrast compared to OTS background is fabricated under 100% relative humidity environment. It was proven that the oxidation process is a function of environmental humidity, applied voltage, and dwelling time of tip on surfaces.

## CHAPTER 4

# A METHOD FOR FABRICATING PROTEIN PATTERNS ON THE OCTADECYLTRICHLOROSILANE (OTS) SURFACE THROUGH PAPER SWABBING

### 4.1. Introduction

Nanoscale protein patterns have potentials to be used in many fields including enzyme catalysis, biosensors, tissue engineering, diagnostic protein tips and pharmacology.<sup>1-3</sup> However, precisely and easily immobilizing protein molecules onto a specific place on a surface while retaining their native biological functionality is a difficulty and challenging. Generally, a patterned substrate that contains some protein adhesives and resistive terminated groups is necessary for the selective binding of protein molecules from the liquid phase. Then, the sample with the chemical patterns is exposed to the protein solution to let the protein molecules accumulate on the patterned area. The driving forces for protein adsorption on the chemical patterns are electrostatic interactions, covalent bonding and bio-specific linkage.<sup>15-17</sup> This process introduces lots of non-specific adsorptions accumulated in the non-patterned area, which reduces the sensitivity and signal quality of the protein sensors. Therefore, inhibiting the non-specific protein adsorption is a very important task in the protein patterning technology. In the lab, there are two approaches in inhibiting the protein's non-specific adsorption on the surface. One is passivation. An anti-fouling agent, typically an oligo/poly-ethylene glycol-based molecule is used to passivate the surface that is not designated for protein adsorption.<sup>144-149</sup> For example, Gu et al. fabricated patterns on the oligoethylene glycol (OGE)-terminated silane film by scanning probe oxidation. Avidin molecules were then coupled onto the pattern using 1-ethyl-3-[3-(dimethylamino)propyl]-carbodiimidehydrochloride (EDC) cross-linking, while the OEG-terminated background resisted the non-specific protein adsorption.<sup>150</sup> The other approach to reduce non-specific adsorption is to repetitively rinse the sample in water, buffer solutions or detergent solutions to get non-specific adsorption protein molecules off the surface after the protein

adsorption.<sup>151-155</sup> Both of these ways can generate relatively clean protein patterns, but the adsorption/rinsing parameters (such as the exposure time, buffer pH/concentration, selection of detergents, the rinsing time /strength) have to be optimized through trial and error, which is a cumbersome task.

In our lab, we created clean lysozyme protein patterns through the approach of “surface swabbing” with a piece of chemwipe paper, which is an easy and non-chemical way to avoid the non-specific protein adsorption. In this method, protein molecules were firstly selectively bound on the OTSpd pattern surface which is carboxylic acid-terminated group on the top through coulomb force. Due to the methyl-terminated group on the background of OTS substrate, protein molecules are adsorbed on both the capturing templates and the methyl-terminated alkylsilane surface when the sample was incubated in the protein solution. Subsequently, we swabbed the sample surface with a piece of ChemWipe paper instead of using anti-fouling agent or some rinsing solutions. We found that the paper swabbing removed most non-specifically adsorbed protein molecules. Only specifically immobilized protein molecules on the chemical template remained. Based on the “paper swabbing” approach, it could be concluded that the initial protein adsorption amount on the sample is irrelevant of the quality of the final protein pattern. In addition, this method has the potential to be used on other self-assembled silane films which have been extensively used for surface patterning and surface chemistry modifications without surface passivation or over rinsing. Therefore, the paper swabbing approach can not only generate a clean protein pattern but also is a simple and quick method without additional prior or post treatment on the sample.

## **4.2. Experimental**

### **4.2.1. Preparation of self-assembled OTS film and OTSpd chemical patterns**

(100) silicon wafers are nitrogen doped, each having a resistivity of 5 ohm.cm, were cut into 1×1cm<sup>2</sup> pieces and rinsed with distilled water. After the wafers were dried in a flow of air, they were then boiled in the piranha solution (one part of 30% hydrogen peroxide solution in two parts of 98% sulfuric acid) for

20 minutes at 120-125°C to grow a fresh oxide layer. This solution is an extremely potent oxidant. It removes organic impurities from the substrate and also helps to grow a thin oxide layer of hydroxyl (Si-OH) groups on the top. When the solution cooled to room temperature, these wafers were rinsed and kept in the distilled water for future uses. The hydroxyl groups created a hydrophilic surface on top of the wafers.

After being rinsed in deionized water and dried in a stream of nitrogen, the cleaned wafers were dipped in a 5mM octadecyltrichlorosilane (OTS) toluene solution to start the adsorption reaction. The structure of OTS is shown in Figure 4.1. AFM (Picoscan 3000; Agilent Technologies), FT-IR(Varian Exalibur 3100) and Ellipsometer (PHE-101) were used to characterize the silane adsorption after the overnight soaking in the OTS toluene solution. It was proven that the OTS surface is a featureless homogenous surface. The highly oriented and densely packed OTS film was very flat with a root mean square roughness smaller than 2Å. Over the AFM scanner's range (90×90µm<sup>2</sup>), the height variation was smaller than 5nm. The infrared spectroscopy of the OTS film was similar to the published one.<sup>156</sup> The ellipsometry results indicated that the OTS film thickness was 26±3Å, which was consistent with the published result as well.<sup>102</sup>

Figure 4-1. The structure of octadecyltrichlorosilane (OTS)

As we discussed before, to immobilize protein molecules on the surface, a patterned substrate which contains protein adhesives and resistive terminated groups is firstly required to selectively absorb the protein molecules from the liquid phase. In our experiment, the protein adhesive terminated groups (OTSpd) were created by AFM local oxidation lithography method, which was demonstrated in chapter 3.

## 4.2.2. The Fabrication and characterization of protein patterns

### 4. 2.2.1. Immobilize lysozyme molecules on the OTS surface

Lysozyme is a well-studied protein with known structure and functions. It is a relatively small globular protein with a molecular mass of 14kDa and dimensions of  $30 \times 30 \times 50 \text{ \AA}^3$ ,<sup>157</sup> which can hydrolyze 1-4-  $\beta$ -glycosidic linkages between N-acetylmuramic acid (NAM) and N-acetyl-D-glucosamine (NAG) residues present in the mucopolysaccharide cell wall and has a similar function as cellulase. The hydrolysis reaction of lysozyme is shown in Figure 4.2. Furthermore, lysozyme has been successfully immobilized and imaged with molecular resolution by the Atomic Force Microscope (AFM). As a model, we chose to first immobilize the hen egg white lysozyme on chemical patterns and study its binding activity to antibody.

Figure 4-2. The hydrolysis reaction of lysozyme to 1-4-  $\beta$ -glycosidic linkages between NAM and NAG

To immobilize protein molecules on the surface, firstly the protein molecules of interest need to be selectively adsorbed on some functionalized chemical islands through specific forces such as covalent binding, electrostatic,



bio-specific interactions, and molecular recognition. It has been demonstrated that lysozyme molecules can be immobilized onto carboxylic acid terminated chemical pattern to form a tightly packed monolayer on the chemical substrate through the coulombic force. In our experiment, the carboxylic acid-terminated chemical pattern (OTSpd) was fabricated by the AFM local oxidation lithography as described earlier. The carboxylic acid-terminated silane surface (OTSpd) has an estimated pKa of 4.9.<sup>158</sup> In a pH 7 buffer, the carboxylic acid-terminated pattern carries negative charges. The isoelectric point of lysozyme is 11, and lysozyme molecules carry positive charges in the pH7.0 buffer.<sup>159</sup> When the sample was incubated in a 4 $\mu$ g/ml lysozyme solution (in a 4-(2-hydroxyethyl)-1-piperazineethanesul-fonic acid (HEPES) buffer, pH 7.0, 25mM) for 2 hours, the positive charged lysozyme molecules are driven onto the negatively charged carboxylic acid-terminated patterns by the attractive Coulomb force. In the meanwhile, the protein molecules are also non-specifically adsorbed on the OTS background. The water contact angle on the sample surface changed from 110 $^{\circ}$  to smaller than 60 $^{\circ}$  after the protein incubation, which indicated that the whole surface was covered with protein molecules. The sample was then rinsed with deionized water and dried in a stream of nitrogen gas. Next, a piece of ChemWipe paper was cut into 2 $\times$ 5cm<sup>2</sup> stripes. We held the sample between the thumb and the index finger and wrapped it with the paper stripe. The sample surface was swabbed several times with a force between 1 and 5N, but each ChemWipe paper stripe was used only once. During each swabbing process, the motion was one directional. Back-and-forth swabbing should be avoided.

After being swabbed, the sample surface became hydrophobic again. Water stayed on the surface as beads instead of spreading to the whole surface. Figure 4.3 shows the AFM image of lysozyme patterns after the swabbing. The non-specifically adsorbed lysozyme molecules were completely removed, while the lysozyme molecules specifically immobilized on the carboxylic acid-terminated chemical templates remained intact. In Figure 4.3a, both the line and disc-shaped chemical patterns were generated through AFM probe local oxidation lithography. We used different bias duration to fabricate different sizes of the OTSpd discs.

Because the design of the PiciLith software determines the AFM tip always be halted briefly before changing direction during the pattern writing process, the joints between two lines always appear as round discs. In Figure 4.3b, the histogram illustrates that the lysozyme pattern is 17Å higher than the OTS background. Since the OTSpd pattern is 11Å lower than the OTS background, we can derive the height of the lysozyme molecule is 28Å. The lysozyme molecule is 30×30×50Å<sup>3</sup> in size. Thus, the height of lysozyme measured from our experiment is consistent with the value measured from the crystal structure,<sup>157</sup> assuming the lysozyme molecules on the pattern were adsorbed with their long axis parallel to the surface.

From the AFM image, we can see the lysozyme protein patterns are very clean and homogenous. The consistent 28Å height of the patterns' surface indicates the patterns are monolayer. The higher resolution AFM image of the lysozyme pattern directly shows that the lysozyme molecules are tightly packed within the pattern.<sup>160</sup>

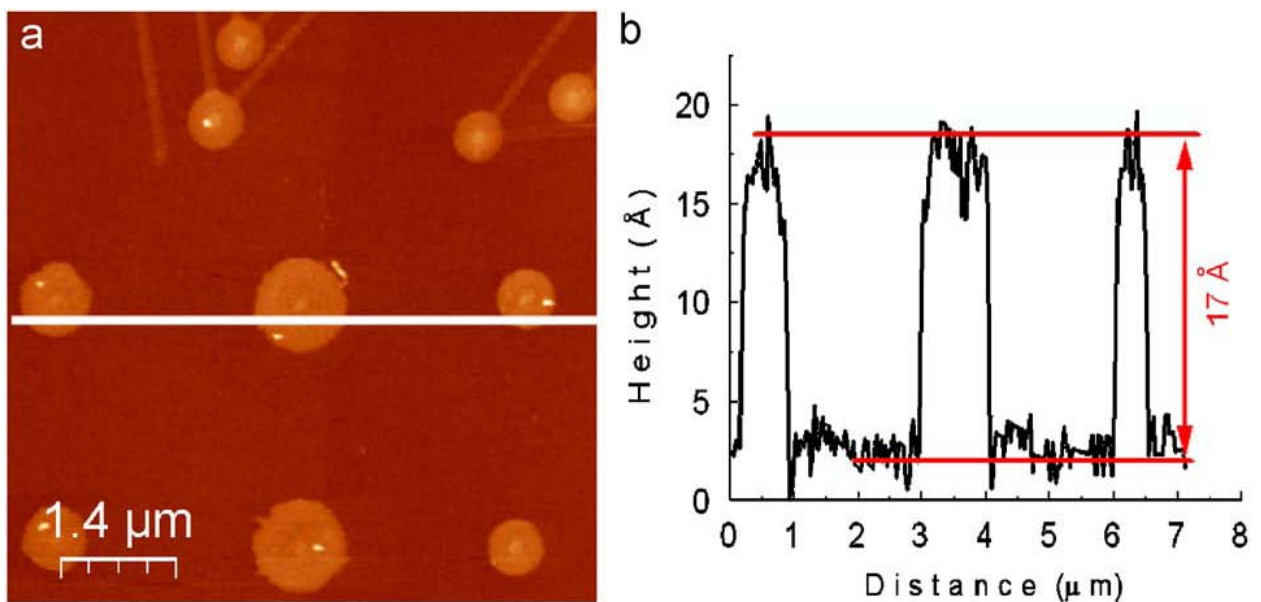


Figure 4-3. (a) The topography image of the lysozyme pattern fabricated on the OTSpd pattern. (AC mode) (b)The height cross-sectional profile along the white line in (a) shows the lysozyme is 17Å higher than the OTS.

The bio-active properties of the lysozyme molecule in the pattern can be tested with the binding of anti-lysozyme antibody. So, the lysozyme pattern was later incubated in the polyclonal anti-lysozyme antibody solution (200ng/ml, in a 10mM HEPES pH 7.0 buffer) for 2h before being characterized by the tapping mode AFM. Figure 4.4a shows the OTSpd chemical pattern. Figure 4.4b shows the same pattern after lysozyme incubation. Figure 4.4c shows the same pattern after the protein pattern was incubated with antibodies. Figure 4.4d is the histogram of Figure 4.4c. From the histogram, we find that the antibody-covered pattern is  $46\pm 6\text{\AA}$  higher than the OTS background. The height of the pattern increased an additional  $29\text{\AA}$  after we incubated the lysozyme pattern with the antibodies. The  $29\text{\AA}$  height corresponds to the antibody's height.<sup>161-163</sup> The anti-lysozyme antibody from the solution can selectively bind on the lysozyme molecule in the pattern on the surface, which demonstrates that our "surface swabbing" approach can fabricate clean and bio-active protein patterns.

There are several reasons that explain why the OTSpd patterns do not appear as round discs at joints of the lines. Firstly, due to the brief halt of the AFM tip when the tip is changing the direction on the surface, the OTSpd pattern should appear as round discs in the joint of lines, as those shown in Figure 4.3a. However, due to the surface heterogeneity (defects in the OTS film), the OTSpd patterns do not appear as round discs, and they instead appear as irregular shapes. We deliberately chose this region to demonstrate that the OTSpd template precisely controls the shape of the lysozyme pattern, even at those small irregular features. In Figure 4.4c, the antibody-bound pattern has exactly the same shape as the lysozyme pattern, which has, in turn, exactly the shape of the OTSpd pattern. Therefore, there exists neither non-specifically adsorbed protein nor non-specifically adsorbed antibody as shown in Figure 4.3.

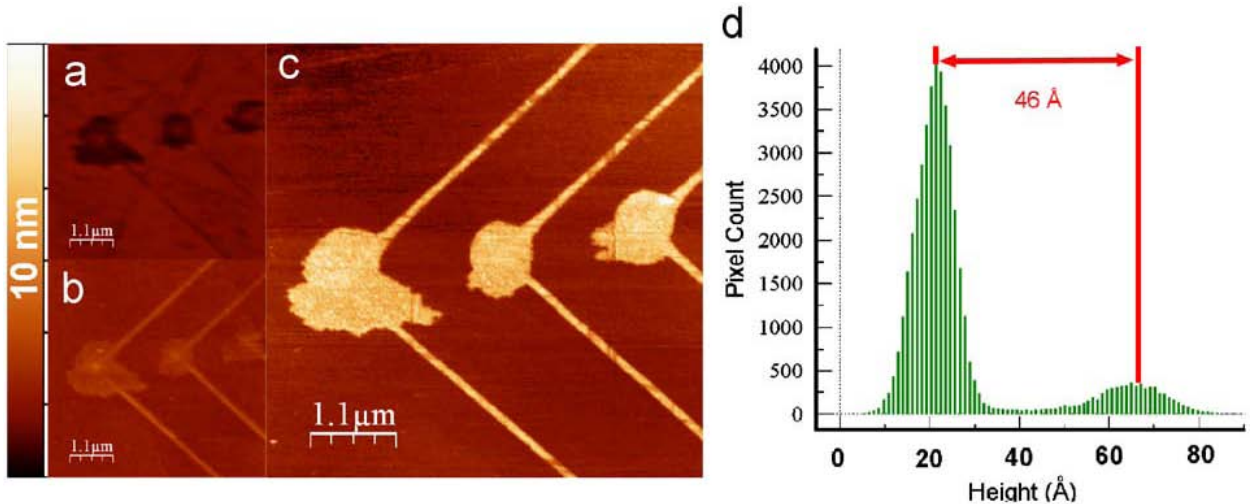


Figure 4-4. Anti-lysozyme antibodies selectively bound on lysozyme patterns after 2h incubation in antibody solution: (a) The OTSpd pattern. (b) The lysozyme pattern on the OTSpd template. (c) The lysozyme pattern after being incubated with polyclonal anti-lysozyme antibodies. (d) The histogram of (c). (a), (b), and (c) are topographic images, acquired using the AC mode of the Agilent PicoPlus AFM .All topographic images are rendered in the 10nm height scale

To further identify the binding of lysozyme and antibodies on the surface, the Infrared spectra of lysozyme and lysozyme-antibody complex were obtained respectively. Since lysozyme patterns smaller than 10μm would not be detectable by the IR microscope, a relatively larger lysozyme pattern was need for the IR characterization. We used the AFM to fabricate an 8×8 array of lysozyme discs in a 50×50 μm<sup>2</sup> area. Each disc in the array is 3 μm in diameter. Sixteen such arrays were fabricated as a 4×4 matrix inside a 200×200 μm<sup>2</sup> patterned region, resulting in 1024 lysozyme discs in total. The silicon wafers we used were polished on one side. The pattern was fabricated on the polished side. On the rough side, we applied a trace amount of Vaseline to eliminate the IR interference from two surface of the sample. To locate the lysozyme pattern, we made a scratch mark on the wafer before fabricating the protein pattern. Using the optical microscope attached on the IR microscope and the marks on the wafer as a reference, we could locate the invisible pattern and obtain the IR spectra over the 200×200 μm<sup>2</sup> patterned region.

The standard IR spectrum for the lysozyme was obtained by directly applying one drop of 4mg/mL lysozyme solution onto the silicon surface till it dried. Lysozyme formed a thick film on the surface after the drying, which appeared as a dark stain through the optical microscope. We acquired the IR spectrum of the thick film and used it as the standard IR spectrum of the lysozyme.

Here, The Infrared spectra of the different wafer surface were acquired by using a Varian UMA 600IR microscope equipped with a liquid nitrogen cooled mercury cadmium telluride (MCT) narrow band detector in the reflection mode. Figure 4.5b shows that the infrared spectra of the lysozyme monolayer were immobilized on the chemical template. Figure 4.5a shows that the infrared spectra of the lysozyme thick film with non-specific adsorption on the silicon wafer surface. Although the amide I, amide II, amide III, and N-H stretching bands are weak due to the monolayer nature of the pattern, the infrared spectra on the chemical templates are similar to the spectra of absorbed lysozyme on the surface. In addition, Figure 4.5c shows the infrared spectrum of the antibody covered lysozyme pattern, where a broad peak from 1100-1900  $\text{cm}^{-1}$  appears and buries all the weak peaks of the amides.

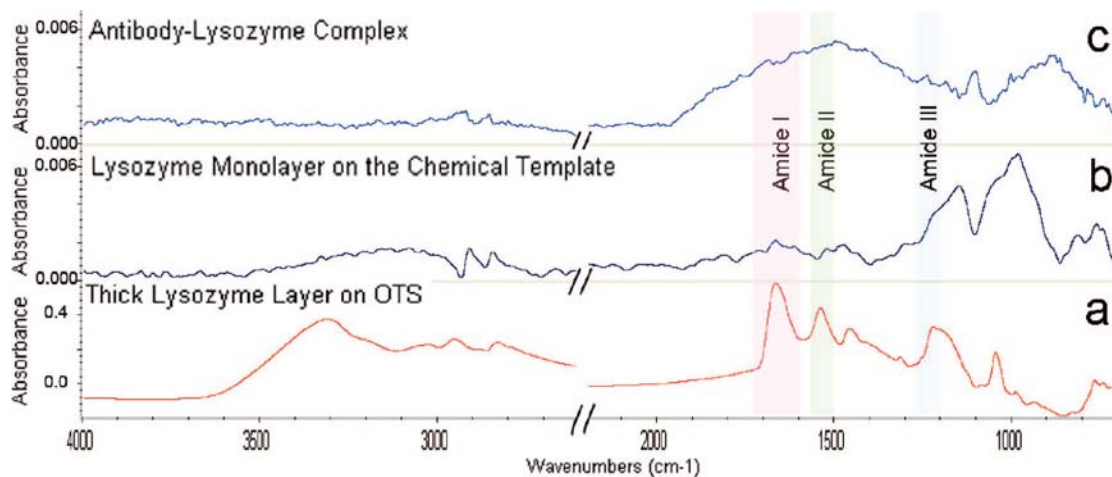


Figure 4-5. Infrared spectra of lysozyme and lysozyme-antibody complex: (a) infrared spectrum of a thick lysozyme film on the surface, (b) infrared spectrum of the lysozyme monolayer immobilized on the chemical template, and (c) spectrum of the same pattern after incubation with the antibody.

#### 4.2.2.2. Immobilize catalase molecules on the surface

A catalase protein pattern was fabricated on the OTS surface to demonstrate that the “surface swabbing” approach is not only applicable to lysozyme molecules but also applicable to other proteins.

Catalase is a well-known enzyme which can catalyze the decomposition of hydrogen peroxide. Oxygen is one of the products of the decomposition reaction, which can be observed as bubbles generated from the hydrogen peroxide solution. This provides a chance to study the activity of catalase patterns on the surface through the direct observation of the oxygen bubbles from the hydrogen peroxide solution given that they are still catalytically active. To immobilize catalase molecules on the OTSpd chemical patterns as lysozyme, similarly, the sample with OTSpd patterns will be incubated in the 4 $\mu$ g/ml catalase solution for 2 hours as the same procedure as that of the immobilization of lysozyme. The bovine catalase's isoelectric point is 5.4. In the pH3.5 buffer, the catalase molecule is positively charged, while the OTSpd pattern surface is slightly positively charged as well. In addition, the hydrophilic surface of the catalase has a stronger adhesion to the hydrophilic surface of the OTSpd than that of the hydrophobic OTS surface. Therefore, during the incubation the adhesion force drove the catalase molecule to selectively adsorb on the carboxylic acid-terminated template. Figure 4.6a shows a catalase pattern immobilized on the OTSpd template. The AFM image demonstrates that no catalase non-specifically adsorbed on the OTS surface after the swabbing.

It was demonstrated that catalase molecules can be immobilized on the OTSpd pattern and that a clean catalase can be obtained through the “paper swabbing” method. From the AFM images in Figure 4.6a, we can see that the immobilized catalase molecules are closely packed together on the patterns. In Figure 4.6b, the height cross-sectional profile along the white line in Figure 4.6a shows that the catalase pattern is 29 $\text{\AA}$  higher than the OTS background. Considering the 11 $\text{\AA}$  depth of the OTSpd pattern, the catalase height measured from AFM is about 40 $\text{\AA}$ , which is similar to the previous published results.<sup>164</sup>

To test the bio-activity of the catalase pattern fabricated on the OTS substrate, a drop (3 mL) of a 3%  $\text{H}_2\text{O}_2$  solution (in pH3.55 mM HAC/NaAc buffer) was applied onto the patterned area of the sample. Another 3mL drop of the 3%  $\text{H}_2\text{O}_2$  solution was also applied in a non-patterned region on the same sample as a control. At 25°C, after an hour, we observed an oxygen bubble inside the  $\text{H}_2\text{O}_2$  drop that covered the catalase pattern as shown in Figure 4.7a. In contrast, no bubble was observed for the control  $\text{H}_2\text{O}_2$  drop (Figure 4.7b). In Figure 4.7a, the pictures were taken through an optical microscope that focused on the  $\text{H}_2\text{O}_2$  drop/OTS contact interface. The field of view represents a small region within the drop. The bright background is the  $\text{H}_2\text{O}_2$  drop and the black disc is the oxygen bubble since the light reflected off the gas/liquid interface was not collected by the microscope's objective.

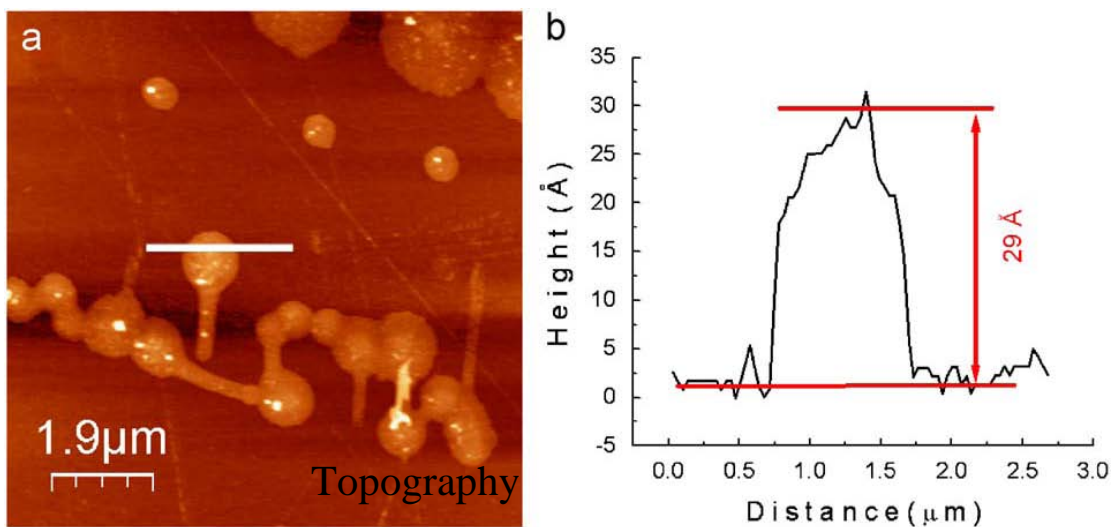


Figure 4-6. The catalase pattern fabricated on the OTSpd pattern after paper swabbing. (a) Topography, (ACMode). (b) The height cross-sectional profile along the white line in (a). The profile shows that the catalase pattern is about 29Å higher than the OTS background.

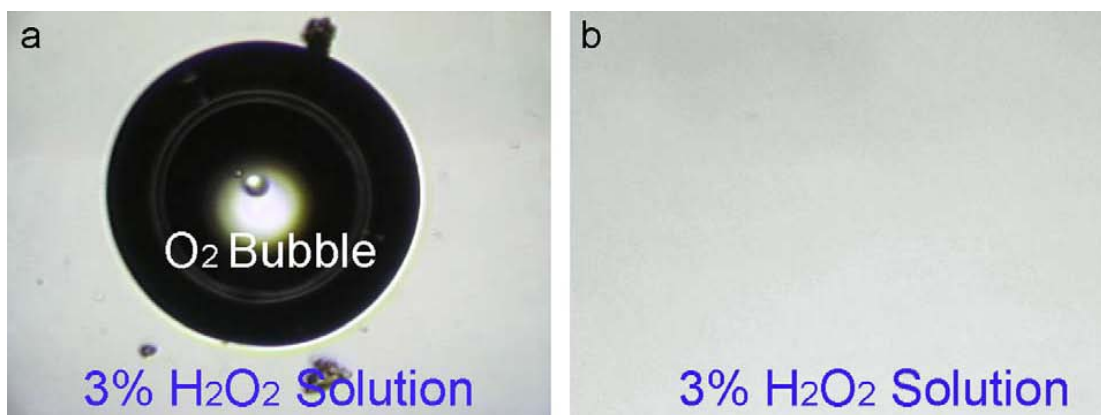


Figure 4-7. (a) An oxygen bubble (the black disc) generated over the catalase pattern inside a drop of 3% hydrogen peroxide solution. (b) No bubble was observed when a drop of 3% hydrogen peroxide solution was placed on the OTS surface. The images were acquired through an optical microscope in the reflective mode. The diameter of the oxygen bubble is about 60 mm.

#### 4.2.2.3. Immobilize CaM molecules on the surface

This “paper swabbing” approach was also attempted in order to fabricate calmodulin (CaM) patterns on the OTSpd-MUTMS chemical island. The structure and formula are shown in Figure 4.8. CaM is a calcium binding protein and expressed in all eukaryotic cells. Calcium ( $\text{Ca}^{2+}$ ) concentration is very important for many biological functions such as metabolism, smooth muscle contraction and immune response.<sup>165</sup> CaM participates in transducing numerous calcium concentration based signals to regulate these crucial cellular responses through the direct and indirect binding with calcium in many organisms.<sup>166-169</sup> We say “indirect” binding because a lot of proteins can not bind with calcium by themselves without the “help” of CaM. Therefore, the study of the binding of CaM and  $\text{Ca}^{2+}$  at the molecular level is valuable to understand how the change of  $\text{Ca}^{2+}$  signal is converted into cellular function in the organism.

In this experiment, OTSpd patterns were firstly fabricated through AFM local oxidation lithography. The sample was then incubated in 5mM mercaptoundecyltrimethoxysilane (MUTMS) in toluene solution over night. It was proven that the MUTMS molecules can self-assemble a layer on the OTSpd



surface through hydrogen bonding. Therefore, the carboxylic acid group on the surface was replaced by hydrogen sulfur (H-S) group on the MUTMS. After that, a drop of 100mM mercury chloride was dipped on the pattern area of surface for ten minutes and then rinsed off with the stream of deionized water. MUTMS molecules on the surface could react with mercury chloride to produce Hg-S bond on the surface, which provides a good substrate for the binding of cystein on CaM. Figure 4.9 shows a CaM pattern immobilized on the OTSpd-MUTMS template. The AFM image demonstrates that no CaM was non-specifically adsorbed on the OTS surface after the swabbing.

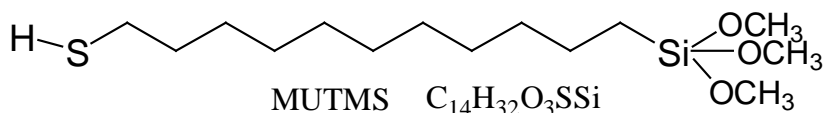


Figure 4-8. The structure and formula of mercaptoundecyltrimethoxysilane (MUTMS)

## Topography

Figure 4-9. The calmodulin (CaM) pattern fabricated on the OTSpd-MUTMS pattern after paper swabbing. Topography, (ACMode)

It was demonstrated that CaM molecules can be immobilized on the OTSpd-MUTMS pattern and a clean CaM pattern can be obtained through “paper swabbing” method. It is expected that the binding information gained on the CaM patterns can be obtained through the direct visualization by the AFM. Now, this project is being studied by other group members in our lab.

### **4. 3. Conclusion of Chapter 4**

The carboxylic acid-terminated chemical templates OTSpd on the OTS film can be fabricated through AFM local oxidation lithography. Three kinds of protein molecules were immobilized onto the prefabricated chemical patterns. The “paper swabbing” approach removed all non-specifically adsorbed protein molecules on the OTS background. It was proven that the protein patterns method can generate bio-active protein pattern with a clean background without the need of the anti-fouling the surface or repetitive rinsing.

## CHAPTER 5

# THE BOUNDARY MOLECULES IN A LYSOZYME PATTERN EXHIBIT PREFERENTIAL ANTIBODY BINDING

### 5.1. Introduction

Efficient, stable, and economical protein immobilization methods are always demanded in the production of protein sensors, protein motors, and bioethanol.<sup>87,170-178</sup> Simply, successfully patterning proteins can improve the efficiency and sensitivity of such protein-based devices and reactions. The “paper swabbing” approach can provide clean protein patterns without any non-specific adsorption on the background. It was also demonstrated that the lysozyme protein pattern created by this method is active towards antibody binding.

However, research on the development of protein patterns is still not complete. Normally, people have always paid more attention to the ways of fabricating nanosized protein patterns. However, the activity of the protein pattern is of great importance. To characterize and improve the activity of the immobilized enzyme, the structure–activity relationship of immobilized enzyme has to be understood at the molecular level. It is because that the protein reaction is highly site-specific and directional. That means the spatial accessibility of an immobilized protein molecule is critical, which is subjected to influences such as the adsorption orientation, the adsorption site, and the packing structure of the surface bound protein. The spatial confinements also suppress the relaxation of surface-immobilized protein.<sup>179</sup> It is understood that the immobilized protein molecules did not just arrange their 2-dimensional shape according to the chemical patterns we created, and they have their own distinct characteristics.

Since there are established protocols and feasible procedure for the evaluation of the immobilized lysozyme pattern, we chose this model system to investigate the geometry effect on the antibody binding through direct atomic

force microscope (AFM) visualization.<sup>161-163,180-184</sup> In our experiments two kinds of highly ordered lysozyme protein patterns have been fabricated on the octadecyltrichlorosilane (OTS) self-assembled monolayer surface. One of the lysozyme patterns is half buried in the OTS substrate and the other one is completely exposed out of the OTS substrate. Polyclonal antibodies are found to firstly bind on the edge of protein pattern before binding on the center of the pattern, suggesting that the edge molecules have a higher affinity toward antibody binding than that in the middle. It was demonstrated that protein molecules on the pattern edge had a higher affinity toward antibody binding than that in the center of the pattern. In addition, we found that the antibody binding to the edge lysozyme molecules on the half-buried pattern started from the top, whereas the binding on the extruding pattern started from the side because of their different spatial accessibility. The study is expected to be used in the immobilized enzyme system and as a useful guide in the development of protein patterns with higher activity in the future.

## **5.2. Experimental**

### **5.2.1. Two schemes to fabricate protein patterns**

In our experiments two kinds of highly ordered lysozyme protein patterns were fabricated on the octadecyltrichlorosilane (OTS) self-assembled monolayer surface to study the activity of the immobilized protein at the molecular level. The highly ordered and clean lysozyme protein pattern could be fabricated with “paper swabbing” approach discussed in chapter 4. Our experimental procedure is illustrated in Schemes 5-1 and 5-2, respectively. The antibody binding structures in Schemes 5-1 and 5-2 are not drawn to the actual ratio. They are only for illustration purposes showing they bind to the lysozyme and do not mean that antibodies actually bind to lysozyme in this specific orientation.

### 5.2.1.1. Immobilize lysozyme molecules on the OTSpd surfaces

In the first approach, similarly, carboxylic acid terminated OTSpd patterns were fabricated through the AFM local oxidation lithography in the contact mode in a humid environment.<sup>68,69</sup> The OTSpd patterns direct the shape and dimension of the protein patterns. When the patterned sample was incubated in the lysozyme solution, the lysozyme molecules could selectively bind on the carboxylic acid terminated OTSpd surface from liquid phase through coulombic force. Next, the sample was rinsed with deionized water and gently wiped with “KimWipe” paper to remove the nonspecifically adsorbed protein on the OTS background. The AFM image in Figure 5-1 shows the lysozyme patterns immobilized on OTSpd surface. The fabrication procedure is followed by Scheme 5-1. The histogram in the inset shows that the lysozyme pattern has an apparent height of 18Å, which is a monolayer. The detailed experimental procedure can be found in chapter 4.

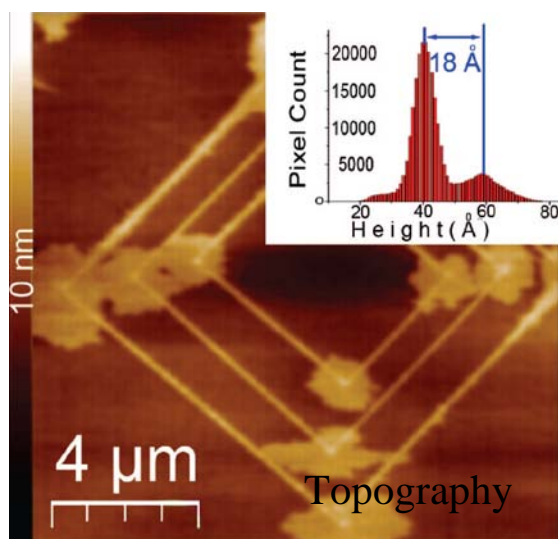
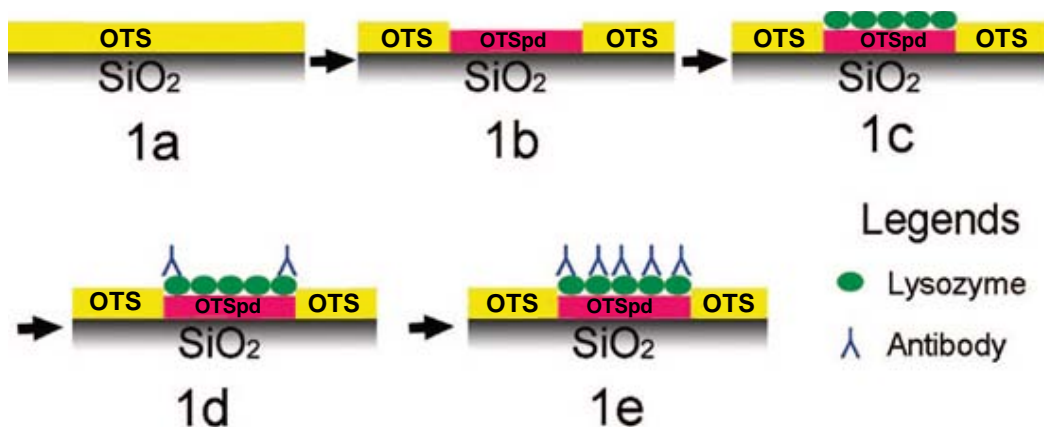
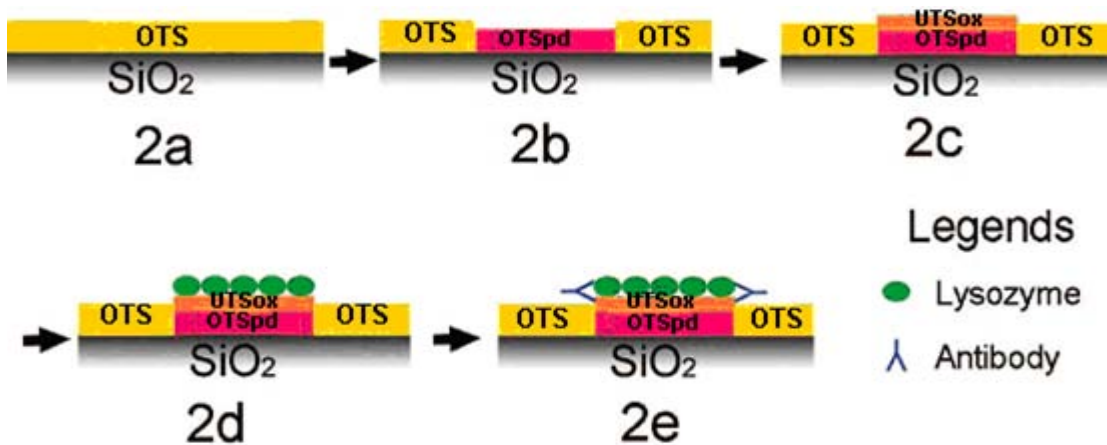


Figure 5-1. Representative lysozyme pattern on the OTSpd template (topography image, tapping mode, 14 μm x 14 μm, the scanning rate is 1 line/s). The histogram (inset) shows that the lysozyme pattern is 18Å above the OTS background.



Scheme 5-1. The fabrication of a half buried lysozyme pattern on OTS surface: OTS (1a) is oxidized to COOH-terminated OTSpd (1b, pink) under a conducting AFM probe. Next, lysozyme molecules (green) absorb on the OTSpd, forming a lysozyme pattern (1c, OTSpd-lysozyme). The polyclonal antibodies (blue) bind to the edge of the lysozyme pattern first (1d). When the incubation time is sufficiently long, antibodies cover the whole lysozyme pattern (1e).



Scheme 5-2. The fabrication of a fully exposed lysozyme pattern on OTS surface: OTS (2a) is oxidized to OTSpd (2b, pink) through the scanning probe oxidation. Next, the OTSpd pattern is reacted with undecenyltrichlorosilane (UTS), to form a double bond terminated OTSpdUTS pattern. The OTSpdUTS pattern is then oxidized to a COOH-terminated OTSpdUTSox pattern (2c). Next, lysozyme is immobilized on the OTSpdUTSox pattern. The immobilized lysozyme on the OTSpdUTSox template (2d) is then reacted with antibodies for 15 min (2e).

### 5.2.1.2. Immobilize lysozyme molecules on the OTSpd-UTSox surfaces

In the second route, carboxylic acid-terminated OTSpd patterns were first fabricated on the OTS film by an AFM conducting tip as the first route. Subsequently, the pattern was incubated in a 5mM UTS toluene solution overnight instead of the lysozyme solution. The UTS silane self-assembled on the hydrophilic OTSpd pattern, forming a second layer, which was double bond terminated on the top. The AFM image in Figure 5.2a shows that the OTSpd-UTS pattern fabricated on the surface, and the cross-sectional height profile in the inset shows that the OTSpd-UTS pattern has an apparent height of 14Å over the OTS background. Next, the sample with the bilayer pattern (UTS on the OTSpd, OTSpdUTS) was incubated in the oxidizing solution (0.01M NaIO<sub>4</sub>, 5×10<sup>-4</sup> M KMnO<sub>4</sub>, in 0.05M Na<sub>2</sub>CO<sub>3</sub> buffer) for 10h at a 40°C. The sample was then rinsed with deionized water and followed by 1% Hydrazine for 1 min. Finally the sample was dried in a stream of nitrogen. After this oxidation process, the double bond was converted into carboxylic group which carries negative charge. The full details of this oxidation process have been explained in chapter 3.

The pattern of OTSpdUTSox was then incubated in a 4µg/ml lysozyme solution (in a 4-(2-hydroxyethyl)-1-piperazineethanesul-fonic acid (HEPES) buffer, pH 7.0, 25mM) for 2 hours. The lysozyme has an isoelectric point of 11 and carries positive charges in the pH 7 buffer solution, while the carboxylic-terminated chemical patterns carry negative charges. When soaking the chemical patterns into the pH 7 lysozyme solution, the attractive coulombic force drove the lysozyme molecules to selectively absorb onto the carboxylic acid-terminated chemical patterns, forming a lysozyme pattern with the same shape as the chemical pattern. Differently, the lysozyme protein pattern in the first route was roughly 17Å higher than the OTS background while the protein pattern from the second route was 44 Å higher than the OTS background. The 27 Å height difference makes the lysozyme protein pattern fully exposed out of the substrate on the surface, which means that the spatial hindrance for the molecule on the edge of the protein pattern in the second route will be much smaller than that in the first route. So, it will give us an opportunity to study the properties of protein's

reaction on the surface in different spatial confinements. The AFM image in Figure 5.2b shows the OTSpdUTSox-lysozyme pattern on the OTS surface, and the cross-section height profile in the inset shows that the lysozyme pattern is 44Å higher than the background. Since the height of the OTSpdUTSox pattern is roughly 14Å above the OTS surface, the height of the lysozyme is 30Å, which is consistent with the previous experiment result.

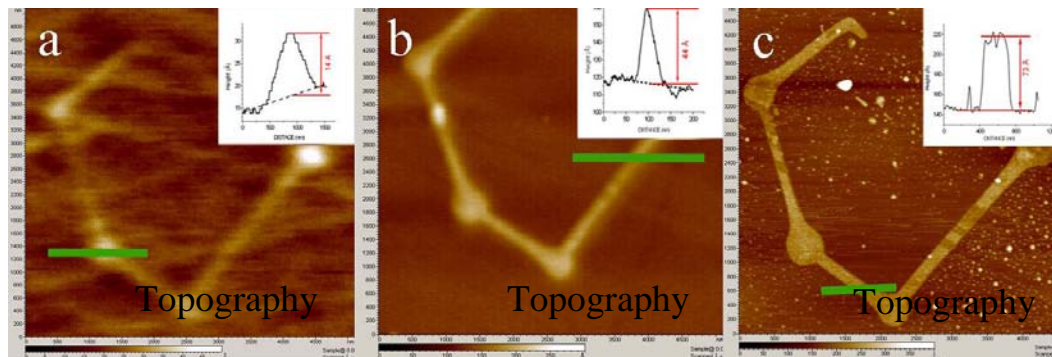


Figure 5-2. The heights of a pattern during the surface reactions in Scheme 5.2. a. The OTSpdUTS pattern (2c). The cross-section height profile (green line, plotted in the inset) shows the pattern is 14 Å higher than the background. b. The OTSpdUTSox-Lysozyme pattern (2d). The cross-section height profile (green line, plotted in the inset) shows the OTSpdUTSox-Lysozyme is 44 Å higher than the background. c. The antibody fully covered OTSpdUTSox-Lysozyme pattern. The cross-section height profile (green line, plotted in the inset) shows the antibody-covered pattern is 73 Å higher than the background.

## 5.2.2. lysozyme activity characterization through the binding with antibody

### 5.2.2.1. Boundary binding effect on the lysozyme pattern from Scheme 5.1

To demonstrate that the lysozyme pattern on the OTS surface is still active towards the binding of the antibody, the lysozyme pattern was incubated with the polyclonal anti-lysozyme antibody (anti-hen egg white, rabbit, Rockland Immunochemicals, Inc.) solution. One drop (33μL) of 100 or 200ng/mL polyclonal antibody solution was applied to cover the pattern on the surface. After 15 minutes incubation, the sample was taken out and rinsed three times with 100 μL of 5mM PH 7 HEPES buffer to remove most of the remaining nonspecifically



absorbed antibodies from the surface. Finally, the surface was blown dry with a stream of nitrogen. It was found that the antibodies preferentially bound on the edge of the lysozyme pattern while only a few antibodies bound to the lysozyme molecules in the pattern interior. Figure 5.3 shows the lysozyme pattern right after the antibody incubation. We can see that the edge of the lysozyme pattern increased an additional 28Å in height after the incubation with the antibody, which corresponds to the height of the antibody.<sup>161-163</sup> In Figure 5.4, we also measured the size of the antibody which non-specifically adsorbed on the OTS film (white spots in the image). From the cross-sectional profile, it shows the height of the antibody is around 31 Å. After incubating the lysozyme pattern in a 200ng/mL antibody solution for 8 h, the antibody fully covered the whole lysozyme pattern. Therefore, the whole lysozyme pattern grows an additional 28Å in height. The AFM image in Figure 5.2c shows us the antibody-covered pattern on the surface, and the cross-sectional height profile in the inset shows that the pattern has an apparent height of 73Å over the OTS background. Figure 5.2a-c shows the same region of pattern after the incubation in UTS solution, lysozyme solution, and anti-lysozyme polyclonal antibody solution, respectively. After each cycle of incubation, it shows the pattern maintained the basic shape and structure, and the pattern height increased from 14Å to 44Å, and 73Å.

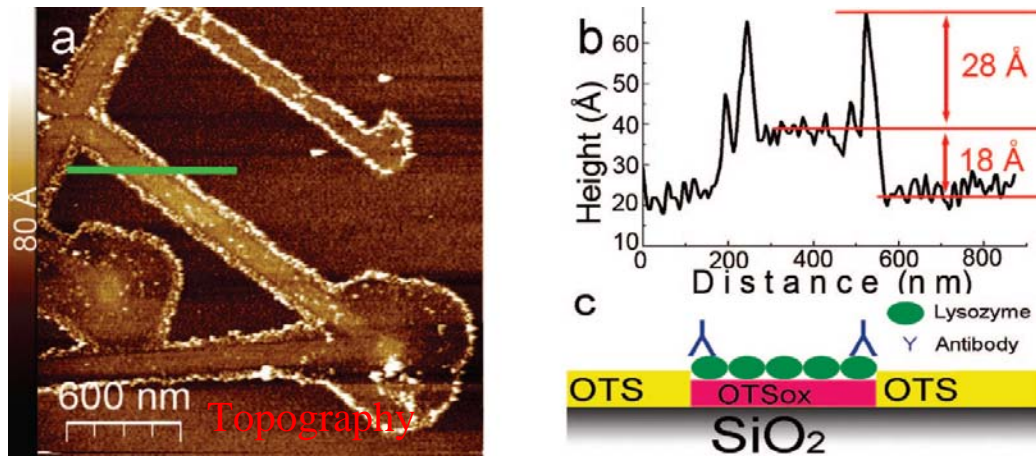


Figure 5-3. Polyclonal antibodies preferentially bind to the edge of the OTSpd-lysozyme pattern after 15 min incubation in a 100 ng/mL antibody solution. (a) Topography image (tapping mode,  $2.3 \mu\text{m} \times 2.3 \mu\text{m}$ , the scanning rate is 0.8 line/s.). (b) Height cross-sectional profile corresponding to the green line in (a). The profile shows that the lysozyme pattern is 18 Å above the OTS. The edge of the lysozyme pattern increases by an additional 28 Å after incubating in the antibody solution. (c) Structure model of the antibody bound on the lysozyme pattern.

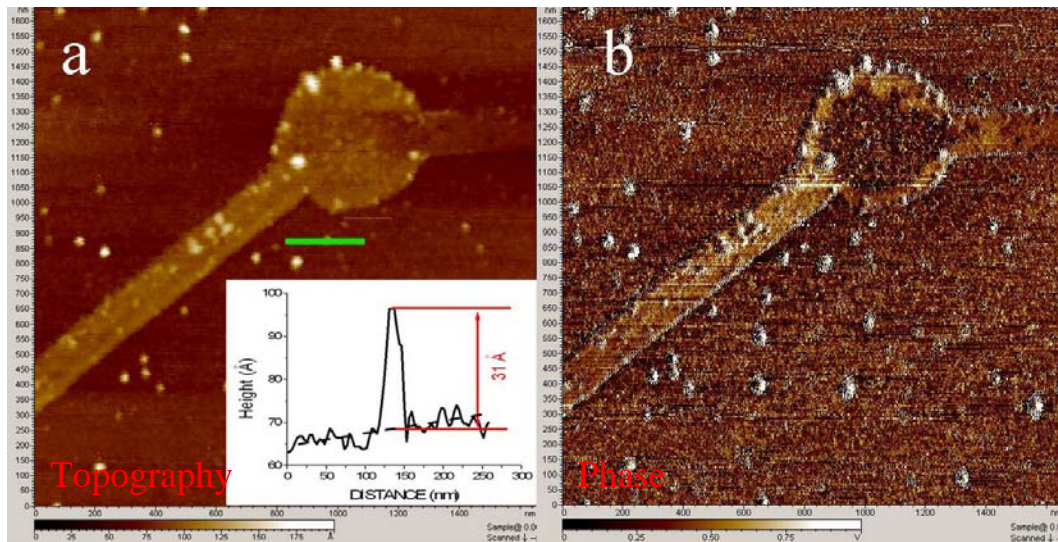


Figure 5-4. Analysis of the antibody height and phase contrast: a. Topography image of protein bound antibodies and the non-specific absorbed antibodies on the OTS background. The height cross-section profile (inset) of a non-specific absorbed antibody shows that the height of the antibody is 31 Å. b. The phase image of the same region; The antibodies appear as white spots.

Two control experiments have been done to demonstrate that the observed binding is a biorecognition event. Firstly, we rinsed a lysozyme pattern that had been incubated for 8h with a 200ng/mL antibody solution. The pattern was fully covered by the antibody. We imaged the sample before and after the rinsing. We found that the abundant rinsing only removed the nonspecifically adsorbed antibodies on the OTS background instead of those bound on the pattern area. It was proven that the rinsing process could not affect the adsorption of the lysozyme or the antibodies bound to the lysozyme.

Secondly, following the same procedure, anti-lysozyme antibodies were replaced by anti-polyhistidine antibodies in the incubation with the lysozyme pattern. The AFM image in Figure 5.5 shows that most of the anti-lysozyme antibodies preferentially bind to the edge of the disc shaped lysozyme pattern (white spots). Just a few anti-polyhistidine antibodies are observed on the lysozyme pattern, with only one absorbed close to the edge. It means that the polyhistidine antibodies do not exhibit the “edge binding” as anti-lysozyme antibodies do. Therefore, the observed “boundary binding” is a biospecific binding rather than nonspecific adsorption of antibodies on the step edges.

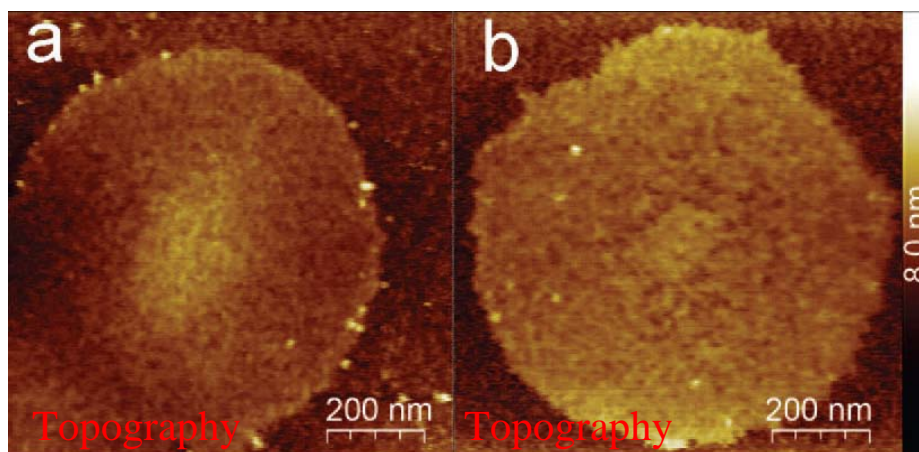


Figure 5-5. Control test of the antibody binding. Representative AFM tapping mode topography images; both (a) and (b) are 917 nm  $\times$  917 nm in size and 8.0 nm in height scale. A concentration of 100 ng/mL anti-lysozyme polyclonal antibody (a) or anti-polyhistidine antibody (b) was deposited on two lysozyme patterns with the same conditions.

Our observation indicates that (i) the immobilized lysozyme pattern maintains the antibody binding activity and (ii) the antibodies bind to the boundary lysozyme molecules of protein pattern before they bind to the interior lysozyme molecules. To further understand the “edge binding” effect, another experiment was done to compare the antibody binding to lysozyme molecules in a tightly packed, full monolayer lysozyme pattern with a loosely packed, submonolayer pattern.

Two different shapes of protein patterns were fabricated respectively in the form of line and disc as shown in Figure 5.6. The line pattern was created using a fast moving tip during the electrochemical oxidation of the OTS film, which led to an incomplete oxidation in the pattern, whereas the disc pattern was created using a stationary tip, which brought the complete oxidation of the OTS film. Thereby, the negative charge density over the line is lower than that of the disc pattern. As a result, after the lysozyme deposition, the lysozyme has only a submonolayer coverage on the line pattern. Whereas, the lysozyme film on the disc shaped pattern forms a tightly packed, full monolayer. The AFM image in Figure 5.6 shows the pattern after 5 minutes of incubation with a 100ng/mL antibody solution. The antibodies (white dots in the images) bound to the loosely packed, submonolayer lysozyme in the line pattern before the tightly packed monolayer ones in the disc pattern. The “preferential edge binding” did not occur for the line pattern. Most observed antibodies bound to the interior molecules of the line pattern. At this shortened incubation time, no binding was observed for the disc, indicating the loosely packed lysozyme molecules in the line pattern have better accessibility and improved flexibility than the edge lysozyme molecules in the tightly packed disc pattern.

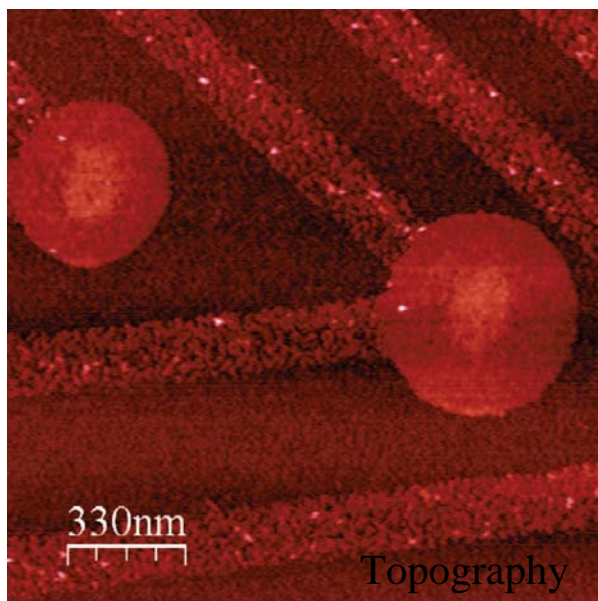


Figure 5-6. Antibody binding to the loosely packed, submonolayer lysozyme pattern (lines) and the tightly packed, full monolayer lysozyme pattern (discs)

It was speculated that the difference in the spatial accessibility and the structural flexibility between the lysozyme molecules on the edge and in the pattern center cause the observed difference in binding preference. In a tightly packed lysozyme pattern shown in Figure 5.7, which is a representative lysozyme pattern immobilized on the OTSpd template, most of the lysozyme molecules are embraced by neighboring lysozyme molecules. The left part of the image is the lysozyme, and the right part is the OTS film. From the smallest feature shown in the image, the resolution is estimated to be about 5 nm. Except for one defect spot, most of the lysozyme molecules inside the pattern appear as a continuous film, which can be understood from the way of the lysozyme molecules bind on the OTSpd pattern. On the OTSpd pattern, if there are still vacant areas larger than the size of lysozyme molecule, the lysozyme molecule from the solution will be driven by the attractive Coulomb force to fill in this site. Therefore on the OTSpd template, the coverage of lysozyme reaches to the saturation value. Therefore, in the pattern, both the neighboring lysozyme molecules and the underneath supporting surface block the epitopes on the lysozyme from external accesses. Also, the relaxation and lateral translational

and rotational motions of lysozyme molecules in the center are constrained by their tightly packed neighbors, whereas the edge proteins are more flexible. Therefore, the antibody molecules have more chances to access the lysozyme on the edge and tend to bind to the edge first. When the edge sites have been occupied and there are still free antibodies in the solution, the antibodies can also bind to the interior lysozyme of the pattern.

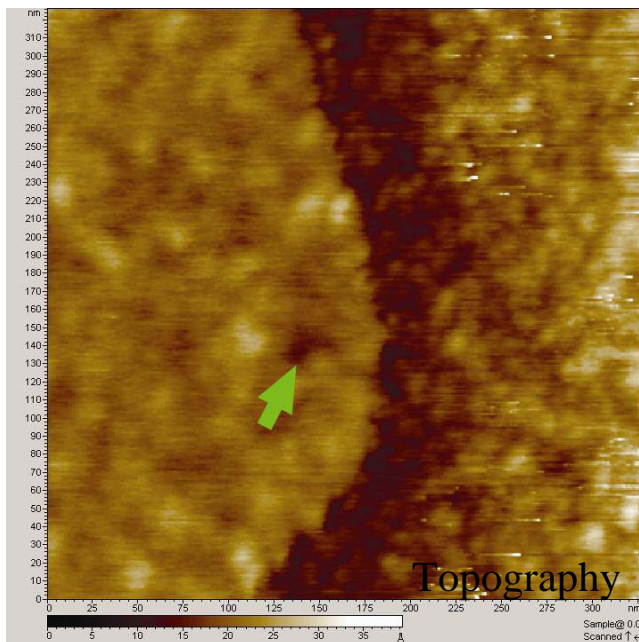


Figure 5-7. High-resolution AFM image of lysozyme pattern. Tapping mode,  $327 \times 327 \text{ nm}^2$ . The left part is one section of a lysozyme disc immobilized on the OTSpd template. Except for one defect spot (green arrow) in the center of the image the lysozyme appears as continuous film. The height variation within the lysozyme pattern is smaller than  $7 \text{ \AA}$ . We explain this variation as the height difference in different lysozyme adsorption conformations.

The preference of the antibody binding on the loosely packed submonolayer rather than tightly packed full monolayer protein pattern further confirms our speculation. Because the lysozyme molecules in the submonolayer film are not in contact with other molecules, they are better relaxed and easier to access than the lysozyme molecules in the tightly packed lysozyme pattern.

#### 5.2.2.2. Boundary binding effect on the lysozyme pattern from Scheme 5.2

In the first route, the lysozyme on the OTSpd chemical patterns is half buried in the 10Å deep OTSpd channel, with an apparent height of only 18Å over the OTS, whereas the protein patterns from the second route is immobilized on a 14Å high terrace with an apparent height of 46Å above the OTS. To investigate the topographic effect of the lysozyme pattern toward the antibody binding, we deposited the antibodies on the OTSpdUTSox lysozyme pattern following the same procedure as described for the OTSpd-lysozyme pattern. The AFM image in Figure 5.8 shows the OTSpdUTSox-lysozyme pattern after 15 minutes incubation with a 100ng/mL antibody solution. At first glance, the pattern appears the same before and after the antibody incubation. However, by analyzing the topographic image (Figure 5.8a) along with the corresponding phase image (Figure 5.8b), we find that the antibodies also preferentially bound to the edge. Furthermore, these antibodies bound to the edge in a configuration different from the antibody binding configuration in the OTSpd-lysozyme pattern.

The phase channel detects the chemical properties of a surface, which complements the capability of topography image to distinguish the different chemical islands with the same topography. Although both the lysozyme and antibody are proteins, they have quite different contrasts in the phase image. Therefore, the phase signal can be used to identify the positions of antibodies in the pattern. From the AFM phase image in Figure 5.8b, we can see the antibody has a higher phase contrast than both the lysozyme and OTS, and it appears as a white spot in the phase image. Therefore, we can locate the position of antibodies through the phase signal change on the surface. In the height and phase cross-sectional profiles, the phase signal has two peaks over the pattern edge, where the topographic data show that the height of the white rim is 31 Å. This height matches the size of the antibody. In the phase profile, there are also few peaks between the two “edge peaks”. They correspond to the few antibodies bound to the lysozyme pattern from the top.

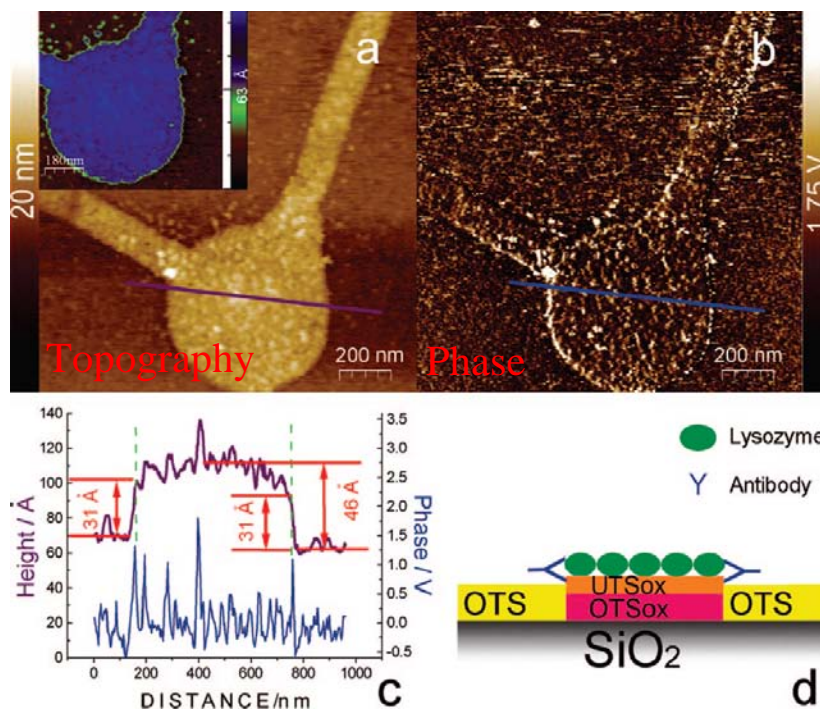


Figure 5-8. Antibodies preferentially bind to the OTSpdUTSox-lysozyme pattern from the side. (a) Topography image, tapping mode,  $1.4 \mu\text{m} \times 1.4 \mu\text{m}$ , 0.8 line/s. Inset: The lysozyme disc is rendered in an exaggerated color scale to demonstrate the 31 Å high antibody on the edge. Due to the minute height difference between the lysozyme pattern and the antibody, the common gradient scale is unable to show the antibody in the topographic image. (b) Phase image. A white rim around the pattern edge reveals the presence of antibodies on the edge. (c) Height (purple line) and phase (blue line) cross-sectional profiles. (d) Structure model of the side-bound antibody on the lysozyme pattern.

It is known that the topographic change may also interfere with the phase signal. However, the phase signal jumping due to the topographic change have unique characteristics and can be distinguished from the phase signal changes from the surface chemistry. Figure 5.9 shows an example of a lysozyme pattern immobilized on the OTSpdUTSox template. It appears as a terrace 46Å above the OTS background. When the tip moved across a step edge, the sudden topography change caused the “jumping” of the phase signal. However, in such circumstances, the direction of jumping is associated with the scanning direction.



In Figure 5.9d, the green curve corresponds to the green line in the trace (left to right scan) phase image (Figure 5.9a). The left (rising) edge and the right (falling) edge appear as a positive peak and a negative peak, respectively, in the phase cross-sectional plot. In the right to left scan phase image (Figure 5.9b), the left (falling) edge and the right (rising) edge appears as a negative and a positive peak (red curve in Figure 5.9d), respectively. Another characteristic associated with the topographic originated phase change is that the phase signal change in the trace scan line is opposite from that in the retrace scan line. The green and red curves in Figure 5.9d are the trace and retrace phase cross-sectional profiles corresponding to the same topographic position. They have opposite peaks over the same topographic position.

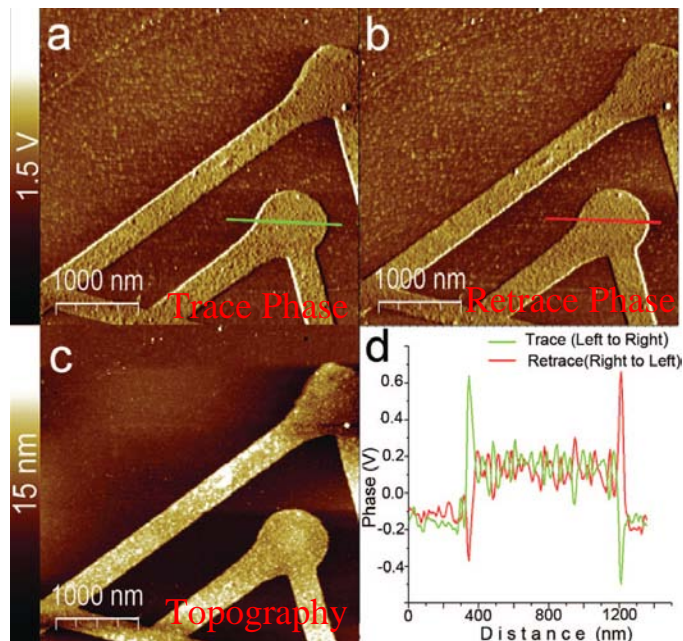


Figure 5-9. Lysozyme pattern immobilized on the OTSpdUTSox template. The lysozyme is 46 Å above the OTS. The phase signal peaks from the topographic jumping are opposite for the trace and retrace scans (3.8 μm × 3.8 μm, tapping mode). (a) Phase image, trace (from left to right, 1.5 V phase scale). (b) Phase image, retrace (from right to left, 1.5 V phase scale). (c) Topographic image, 15 nm height scale. (d) Phase signal cross-sectional profiles corresponding to the red (trace) and green (retrace) lines across the lysozyme terrace.

In the phase channel image of the lysozyme pattern on the OTSpdUTSox template (Figure 5.8b) after the antibody incubation, a white rim surrounds the

lysozyme disc pattern in the phase channel. From the phase cross section plot of the lysozyme pattern after the antibody binding, we found the phase signal shows two positive peaks at both the rising edge and falling edge. In addition, the trace and retrace phase signal lines are identical. Therefore, based on these unique characteristics, we can distinguish the phase signal changes originating from the topography and the phase signal changes originating from the surface chemistry.

From the discussion above, we can conclude that peaks in the phase channel of Figure 5.8c come from surface chemistry change rather than topographic interference. They indicate the presence of the antibodies surrounding the lysozyme pattern after the antibody incubation. Therefore, the white rim around the lysozyme pattern is assigned to the bound antibodies. When the OTSpd-UTSox-lysozyme pattern was incubated in the antibody solution for an enough long time, the antibodies will fully cover the whole pattern surface as shown in Figure 5.2c.

The AFM image in Figure 5.8 also shows that the antibodies preferentially bind to the edge lysozyme molecules in the OTSpdUTSox-lysozyme pattern as OTSpd-lysozyme pattern. However, the antibodies preferentially bound to the edge lysozyme molecules from the top to the OTSpd-lysozyme pattern, while they bound from the side to the OTSpdUTSox-lysozyme pattern. In Figure 5.8c, we plot the height cross-sectional profile and the phase cross-sectional profile together. At the pattern edges, the phase signal has two peaks, which is corresponding to the position of the antibodies. In the same position of the height cross-sectional profile (along the green dashed line in Figure 5.8c), we find there are two small steps on the edge. The height cross-sectional plots of these steps reveals their heights are  $31\text{\AA}$ , which matches the reported size of the antibody.<sup>161-163</sup> Even though these antibodies bound on the side of protein patterns are invisible in the topography image, we can identify the antibody binding through AFM phase channel as well as the phase signal change in the phase cross sectional plot. If the antibodies bind to the edge lysozyme from the top, the antibody would be higher than the protein pattern, which is never observed from

the OTSpdUTSox-lysozyme pattern. In addition to this, the lysozyme pattern is around 46Å higher than the OTS substrate, the observed 31Å height of the step on the protein pattern edge indicates that the antibodies bind to the protein from the side (Figure 5.8d). In both the topography and phase cross section profile, there are also few peaks between the two “edge peaks”. They correspond to the few antibodies bound to the lysozyme pattern from the top.

Through the comparison above, it can be concluded that the fully extruding lysozyme pattern favors the side binding and the half-buried lysozyme pattern favors the top binding. The “template embedding” approach developed in our lab indicates the way of protein immobilization on the surface significantly affects the binding direction for protein molecules to polyclonal antibodies.

### **5.3. Conclusion of Chapter 5**

Two kinds of tightly packed lysozyme pattern were fabricated on different prefabricated chemical pattern through AFM local oxidation lithography. In the antibody binding experiment, we find that the antibodies preferentially bind to the edge lysozyme molecules before their binding to the lysozyme molecules in the interior of the pattern. It could be understood that the edge molecules have better spatial accessibility and flexibility. The interior molecules on the pattern are surrounded by their neighbor molecules and their epitopes are blocked by their close packed neighbors from the periphery as well as the supporting surface from the bottom. It can be derived that a protein nanoarray with more protein molecules on the edge has higher bioactivity than a protein microarray if the coverage of an immobilized protein remains the same. In turn, a microarray has more edge protein molecules and has higher bioactivity than a protein film. Therefore, reducing the protein pattern feature to the nanoscale will improve the overall binding of immobilized proteins toward antibodies. The study is expected to be used in the immobilized enzyme system and as a useful guide in the development of immobilized enzymes with higher activity in the future.

## CHAPTER 6

### **LABEL-FREE DETECTION OF THE APTAMER BINDING ON PROTEIN PATTERNS USING KELVIN PROBE FORCE MICROSCOPY (KPFM)**

#### **6.1. Introduction**

Patterned DNA and protein have been widely used in the bio-sensing and bio-analysis applications.<sup>185-188</sup> The protein or DNA molecules usually form ordered islands on surface in such protein and DNA arrays. Different kinds of analytes can be recognized or captured by these specific protein or DNA islands on the surface. As a result, the changes originated from this recognition or capture can be gathered and analyzed to obtain analytes' information such as concentration, binding activity, or other derivative properties people are interested in.<sup>186</sup> The array approach in bio-analysis offers lower unit cost, better sensitivity, and the possibility for larger-scale screening. However, the way how to transfer the recognition event into a readable signal always keeps the array technology from being used more in this field. Usually, labeling agents are required,<sup>189</sup> but the requirement of labeling agents limits the applicability and increase the cost of the array method.

Kelvin probe force microscopy (KPFM) measures the spatial distribution of surface potential.<sup>190,191</sup> Bio-macromolecules such as protein and DNA have distinct charges. The surface potentials over the immobilized bio-macromolecules are different from the background. When protein molecules bind to other protein or DNA molecules on the surface, their surface potentials also change. Therefore, measuring surface potential variations during a reaction is a promising approach toward the label-free detection for protein/DNA chips. Previous KPFM experiments have demonstrated that different protein molecules can be recognized based on their different isoelectric points.<sup>189,191</sup> In addition, KPFM can distinguish single stranded DNA from double stranded DNA adsorbed on the surface since single stranded DNA molecules have different surface

charges from double stranded DNA molecules.<sup>189,192-194</sup> These pioneering works have demonstrated the power and potentials of KPFM for the label-free detection of biological relevant events.

Our previous work has shown that in a well-ordered protein pattern, the edge protein has a much higher binding affinity than the interior protein molecules.<sup>160</sup> This is because that the edge protein molecules are better relaxed and are easier to be accessed whereas the protein molecules in the interior part of the tightly pack pattern are blocked and embraced by their neighboring protein molecules. This discovery suggests that in a protein array, the binding event happens from the edge binding. In this chapter, the anti-lysozyme aptamer-protein binding was also investigated. Aptamer based molecular recognition is a developed area that is expected to be used in novel biosensor, where the aptamer-protein binding is the key step.<sup>195-206</sup> Aptamers are short sequences of signal-stranded polynucleotides. Aptamers bio-specifically bind to the different target analytes such as proteins, cells.<sup>207</sup> As we know, the antibodies are routinely used for the protein recognition in the biological field. However, the aptamer has some comparable advantages over antibodies such as less loss of sensitivity after multiple times use, better thermal stability and lower synthesis cost. It was shown the anti-lysozyme aptamer also preferentially bind to the edge of a tightly packed lysozyme pattern. Besides that, most KPFM studies on biological samples have the spatial resolution at the micron level.<sup>189,191</sup> In our lab, a long and sharp Ag<sub>2</sub>Ga needle tip was used and it was demonstrated that KPFM is capable of detecting the aptamer-protein binding down to the nm scale.

## **6.2. Experimental**

### **6.2.1. Fabrication of protein patterns on the OTS film**

The highly ordered and clean lysozyme protein pattern could be fabricated with “paper swabbing” approach we discussed in chapter Four. Some carboxylic acid-terminated OTSpd patterns were fabricated through the AFM probe oxidation lithography,<sup>68,135</sup> which directs the shape and dimension of the protein patterns. When the pattern sample was incubated in the lysozyme solution, the

lysozyme molecules could selectively bind on the carboxylic acid -terminated OTSpd surface from liquid phase through the coulombic force. Next, the sample was rinsed with deionized water and gently wiped with “KimWipe” paper to remove the nonspecifically adsorbed protein.<sup>208</sup> The AFM image in Figure 6.1 shows a representative lysozyme disc before the aptamer binding. The height cross-sectional plot in Figure 6.1c corresponds to the black line in Figure 6.1a, showing an apparent height of 1.5nm of the lysozyme pattern. In Figure 6.1d, the histogram image shows the height distribution of the topography image. From the histogram, we measured the peak positions and their standard deviations. From these values, the lysozyme disc is calculated to be  $1.5\pm 0.4$ nm higher than the OTS background. Since the OTSpd we fabricated was 1nm lower than the OTS film,<sup>69,160</sup> the actual height of the lysozyme in Figure 6.1a is 2.5nm, which is a monolayer and consistent with the published result.<sup>160,209</sup> The detail experiment part could be found in the chapter four.

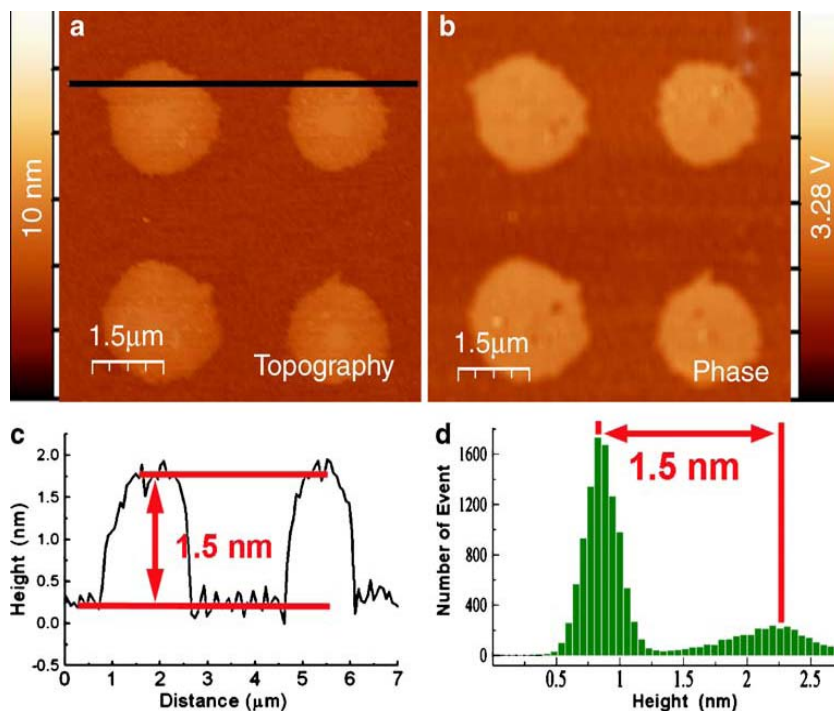


Figure 6-1. A representative lysozyme disc pattern before the aptamer incubation. (a) Topography image. (b) The phase image. (c) The height cross-sectional profile corresponding to the black line in a. d The height histogram of the topography image. From the height distribution statistics, the lysozyme is  $1.5 \pm 0.4$  nm higher than the OTS background. Image was acquired with Agilent PicoPlus AFM in AC Mode

### 6.2.2. Boundary effect for aptamer binding on the lysozyme pattern

To demonstrate aptamer's binding to the lysozyme pattern on the OTS surface, the sample was incubated in a 200  $\mu$ l 100-nmol/ml anti-lysozyme aptamer aqueous solution (pH=7) at room temperature in a sealed vial for 10h. After rinsing with de-ionized water for three times, the pattern was characterized by AFM at 25°C with a relative humidity of 70%. Here, the sequence of anti-lysozyme aptamer is 5'-ATCTA CGAAT TCATC AGGGC TAAAG AGAGT TACTT AG-3', which is obtained from Operon.

After the incubation, the change of lysozyme pattern was shown in the AFM image of Figure 6.2. The topography image (Figure 6.2a) shows that the height of the pattern edge increases an additional 1–5 nm, whereas the interior of

the lysozyme pattern remains unchanged, which is still  $1.5 \pm 0.3$  nm above the OTS. In the corresponding phase image (Figure 6.2b), the pattern edge is much brighter than the pattern interior. In Figure 6.2c, we plotted the height (black) and phase (red) cross-sectional profiles, which correspond to the black and red lines in the topography and phase images, respectively. The plots show that the edge of the pattern increased an additional 5 nm after the incubation. In the height cross-sectional profile, the standard deviation of the lysozyme height is 0.3 nm, whereas the edge of the lysozyme pattern is 5 nm higher than the lysozyme. Therefore, the height increase after the aptamer incubation reflects the real topography change on the pattern edge. It was demonstrated that the anti-lysozyme aptamer preferentially bound on the edge of lysozyme protein pattern. Compared with the “boundary effect” of antibodies on the lysozyme patterns,<sup>160</sup> this preferential edge binding can also be explained as the better flexibility and relaxation of the molecules in the edge of the pattern than that in the interior of the pattern.

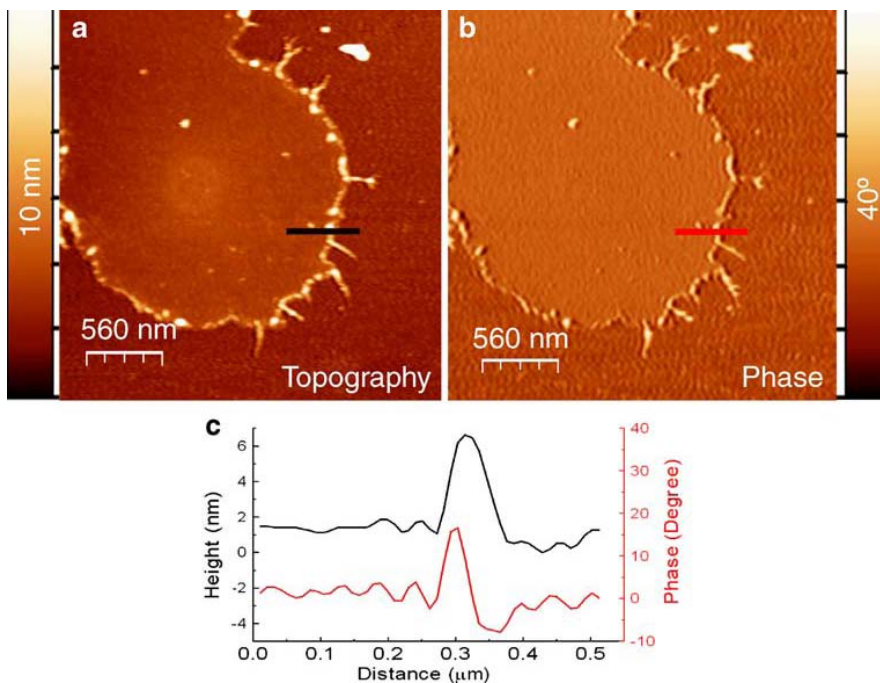


Figure 6-2 The topography (a) and phase (b) images of the tightly packed lysozyme pattern after incubation with the anti-lysozyme aptamer. c The topography (black) and phase (red) cross sectional profiles corresponding to the black line in a and the red line in b. The images were acquired with the Veeco Multimode AFM with the  $\text{Ag}_2\text{Ga}$  tip in tapping mode.



As a control test, a lysozyme pattern was incubated in a 100-nmol/ml solution of a random sequence DNA solution at the same condition as the anti-lysozyme aptamer. This single-stranded DNA is a randomly generated 42-mer, which is the same length as the anti-lysozyme aptamer. The aptamer is also obtained from Operon and its sequence is 5'-TATGC TAAAC CTTAC AAGTT GGAAG TCGAG CGTTG AAGCA GG-3'. After the sample was rinsed with de-ionized water for three times, it was characterized with AFM at 25°C with a relative humidity of 70%. The AFM image in Figure 6.3a shows that the lysozyme pattern remains the same after the DNA incubation. No height change is observed in the topographic image. The pattern in Figure 6.3 is still a lysozyme pattern.

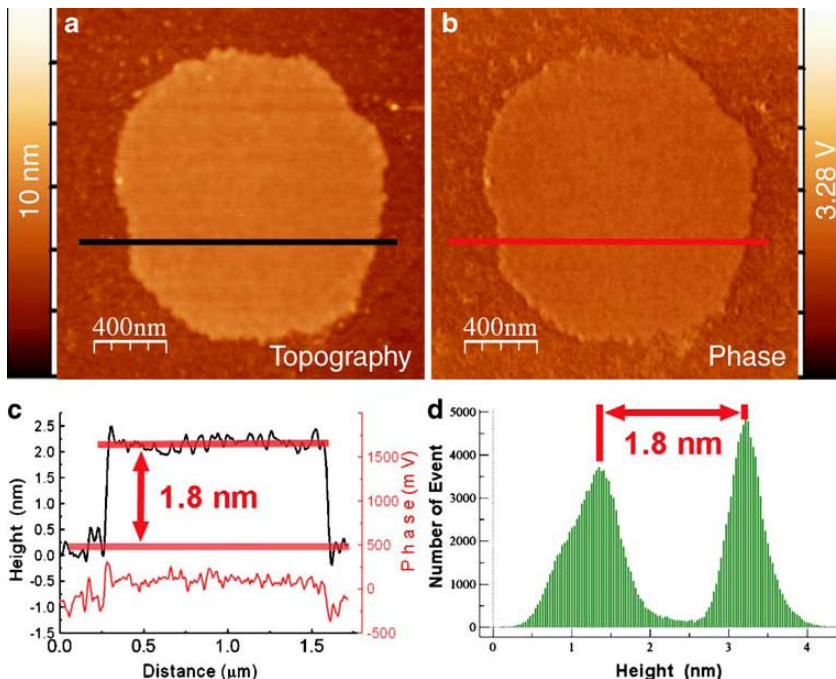


Figure 6-3 The topography (a) and phase (b) images of a representative lysozyme disc after incubation with a solution of randomly generated 42-mer single-stranded DNA. No DNA is observed on the disc. c The topography (black) and phase (red) cross-sectional profiles corresponding to the black line in a and the red line in b. d The height histogram of the topography image. From the height distribution statistics, the lysozyme is  $1.8 \pm 0.4$  nm higher than the OTS background. Images were acquired with Agilent PicoPlus AFM in AC Mode.

The control experiment shows that the randomly generated DNA aptamer did not bind to the lysozyme pattern. This fact confirms that the observed anti-lysozyme aptamer lysozyme binding is a bio-specific recognition event rather than the non-specific adsorption on the surface. Compared with the polyclonal antibodies binding in the last chapter, the anti-lysozyme aptamer also showed the similar preferential edge binding on the protein pattern.

Some fibers could be found growing from the edge of protein pattern in Figure 6.2. In contrast, our control experiment shows that no fiber formed after incubating the same lysozyme pattern with de-ionized water or blank buffers. Therefore, from this control experiment, we can conclude that the fibers in Figure 6.2 are composed of DNA. Some fibers could also be found after the lysozyme pattern was incubated with the random 42-mer DNA. The difference is that the fibers from the randomly sequence aptamer did not bind to the lysozyme pattern but sit on the OTS background. The non-specific adsorbed DNA aptamer could be rinsed off the surface. Since both the anti-lysozyme aptamer and randomly sequenced aptamer can form fibers, the fiber formation is not a protein-specific event. In addition, the fact that the fibers bound on the edge of protein pattern could not be washed off the surface further demonstrates that this “anchoring effect” is protein-specific. From the topography cross section profile, we can know that these fibers are typically 4-6nm in height and several hundred nanometers in length. A fully stretched 42-mers signal-stranded DNA normally is 31.5nm long assuming the base-to-base distance in a fully stretched signal-stranded DNA is  $7.5\text{\AA}$ .<sup>210</sup> Therefore, the height and length indicate that these fibers are not individual aptamer. After incubating the aptamer-bound pattern in a 55°C water bath for 10h, most of the fibers were removed, whereas the aptamers bound on the lysozyme pattern edge still remained. We suspect that these fibers are consisted of many aptamers self-assembled through inter-molecules hydrogen bond, which has been reported by other research group.<sup>211</sup> Based on the experiments finished, we can explain the protein-specific “anchoring effect of the aptamer fibers binding on the edge of protein patterns.

In chapter 5, we explained the antibody's preferential edge binding to lysozyme pattern by the better accessibility, better relaxation, and higher flexibility of the edge lysozyme molecules than the interior ones. To further demonstrate this "edge effect", some tightly packed and loosely packed lysozyme patterns were intentionally fabricated with a stationary tip and fast moving tip, respectively. In the AFM local oxidation lithography process, a stationary AFM tip always produces a disc shaped pattern which has experienced a completed oxidation process. In contrast, a partially degraded OTSpd line pattern was fabricated with a fast moving AFM tip. Its oxidation process is incomplete and will lead to a lower "COOH" surface density of the chemical pattern. After incubating the chemical pattern with a lysozyme solution, a tightly packed lysozyme pattern will be formed in the disc area and a loosely packed lysozyme pattern will be formed in the linear area, respectively.

To understand the edge binding of anti-lysozyme aptamers, we also did the same experiment as to the antibody by fabricating both the tightly packed and the loosely packed lysozyme pattern region in a small area. The AFM image in Figure 6.4 shows the results after these patterns were incubated in the anti-lysozyme aptamer solution. It was demonstrated that aptamers only selectively bound on the edge of the tightly packed, disc-shaped lysozyme pattern. No significant aptamer binding is observed at the interior of the disc pattern. In contrast, aptamers bound both to the edge and the interior of the line pattern. It could be explained that the lysozyme molecules in the loosely packed pattern are not blocked and embraced by their neighboring lysozyme molecules. Therefore, they have better flexibility and relaxation than the lysozyme molecules inside a tightly packed pattern.

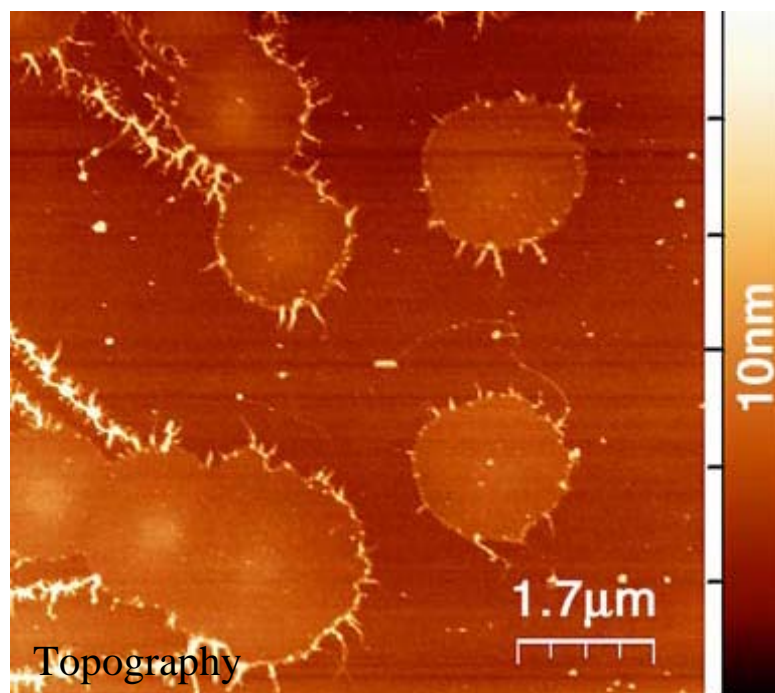


Figure 6-4. The topography image of the loosely packed and tightly packed lysozyme patterns after incubation with anti-lysozyme aptamers. Aptamers bound to both the interior and edge lysozyme molecules in the loosely packed patterns (line patterns in the image). In contrast, aptamers only bound on the edge of the tightly packed lysozyme disc pattern. Image was acquired with Agilent PicoPlus AFM in AC Mode.

From Figure 6.2 and Figure 6.4, we can conclude that the anti-lysozyme aptamer also demonstrates the preferential edge-binding effect when it reacts with a tightly packed lysozyme pattern.

### 6.2.3 The working principle of Kelvin Probe force microscopy (KPFM)

The name “Kelvin probe” is originated from Lord Kelvin who firstly proposed the concept of measuring the difference in work function between two materials.<sup>189</sup> Lord Kelvin’s method was developed by Zisman in 1932 and appeared in its modern form in 1991.<sup>212,213</sup> The physical principle of KPFM is similar as Kelvin’s method except the force is measured here instead of the current. The Kelvin method has a high sensitivity for potential measurement but

does not provide a lateral image of the variation of the contact potential difference (CPD) on the surface.<sup>194,214,215</sup> It is because that it integrates over the whole plate area. However, KPFM method not only detects the CPD between a conducting AFM probe and the surface but also provides a simple way to achieve the high lateral resolution measurement.

In KPFM method, the probe and substrate are imagined as two opposing plates of a capacitor. The energy ( $U_{cap}$ ) of such a capacitor can be expressed as:

$$U_{cap} = 1/2C(\Delta V)^2 \quad (1)$$

where C is the capacitance and  $\Delta V$  is the potential difference between the probe and substrate. By taking the derivative with respect to separation, we get the force between the two capacitor plates.

$$\frac{dU_{cap}}{dZ} = F_{cap} = -1/2 \frac{dC}{dZ} (\Delta V)^2 \quad (2)$$

Here,  $\Delta V$  has a DC and an AC component.

$$(\Delta V) = \Delta V_{DC} + \Delta V_{AC} \sin(\omega_{KP}t) \quad (3) \quad \text{where: } \Delta V_{DC} = \Delta V_{DC,app} - \Delta\phi$$

By expanding the  $(\Delta V)^2$  term, we can see that it can be broken down into three distinct parts each with a different dependence on the AC frequency.

$$(\Delta V)^2 = \left\{ \Delta V_{DC}^2 + \frac{\Delta V_{AC}^2}{2} \right\} - \left[ 1/2 \Delta V_{AC}^2 \cos(2\omega_{KP}t) \right] + \left[ 2\Delta V_{DC} \Delta V_{AC} \sin(\omega_{KP}t) \right] \quad (4)$$

If the frequency ( $\omega_{KP}$ ) is chosen to be the resonant frequency of the probe, the last term in formula (4) will dominate the force response of the capacitor.

Therefore, the force between the probe plate and sample plate has the form of:

$$f = -\frac{dC}{dZ} V_{AC} (V_{TipDC\_Bias} - V_{Surface}) \sin(\omega t) \quad (5)$$

where C is capacitance, Z is separation,  $V_{AC}$  is AC voltage difference between the tip and surface. It is shown that the force felt by the vibrating capacitor is proportional to the difference in voltage between the probe and substrate.

The feedback system of the AFM varies the  $V_{\text{TipDC\_Bias}}$  to minimize the force ( $f$ ) to zero. At this moment, the value of the  $V_{\text{TipDC\_Bias}}$  equals the value of surface potential  $V_{\text{surface}}$ . The principle of KPFM determines that the measured CPD value is a function of the capacitance between the AFM probe and the surface. There is a capacitance between the AFM probe and the surface directly under the AFM probe. There are also capacitance between the AFM probe and the surfaces near the AFM probe. Therefore, the value of CPD is the convolution result from the surface potential directly under the probe and surface potentials from area surrounding the probe.

In addition, the shape of the probe also affects the probe-substrate capacitance. It is concluded that the CPD value over a specific spot also contains information from other places, which lowers the spatial resolution of KPFM. A generic pyramid shaped tip usually yields a poor resolution because it has a large surface region surrounding the tip. Here, we characterized the surface with the  $\text{Ag}_2\text{Ga}$  needle tip from NaugaNeedles Inc. The tip has a long and sharp  $\text{Ag}_2\text{Ga}$  needle attached at the end of the pyramid shaped probe shown in Figure 6.5.

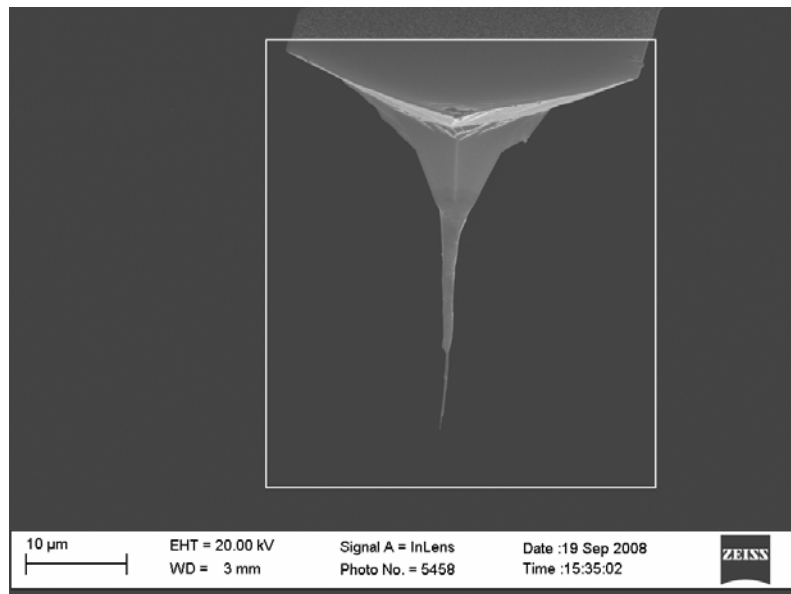


Figure 6-5. The scanning electron microscope (SEM) image of  $\text{Ag}_2\text{Ga}$  needle tip from NaugaNeedles Inc.

Because of the minimal width and surface area, the effect from the tip's side planes and surface surrounding the tip was largely minimized. Thus, the KPFM spatial resolution is improved.<sup>214,216,217</sup> When we scan the same sample with the generic pyramid shaped tip and Ag<sub>2</sub>Ga needle tip, respectively, it was found the AFM images obtained by the Ag<sub>2</sub>Ga needle tip have much higher spatial resolution than those from the generic pyramid shaped tip. All the images are shown in Figure 6.6. The left side including (a), (c), and (e) are scanned by the generic pyramid shaped tip, and the right side including (b), (d), and (f) are obtained by the Ag<sub>2</sub>Ga needle tip. As a result of its shape, the Ag<sub>2</sub>Ga needle tip helps to get the local information directly under the tip, which is ideal for KPFM characterizations.

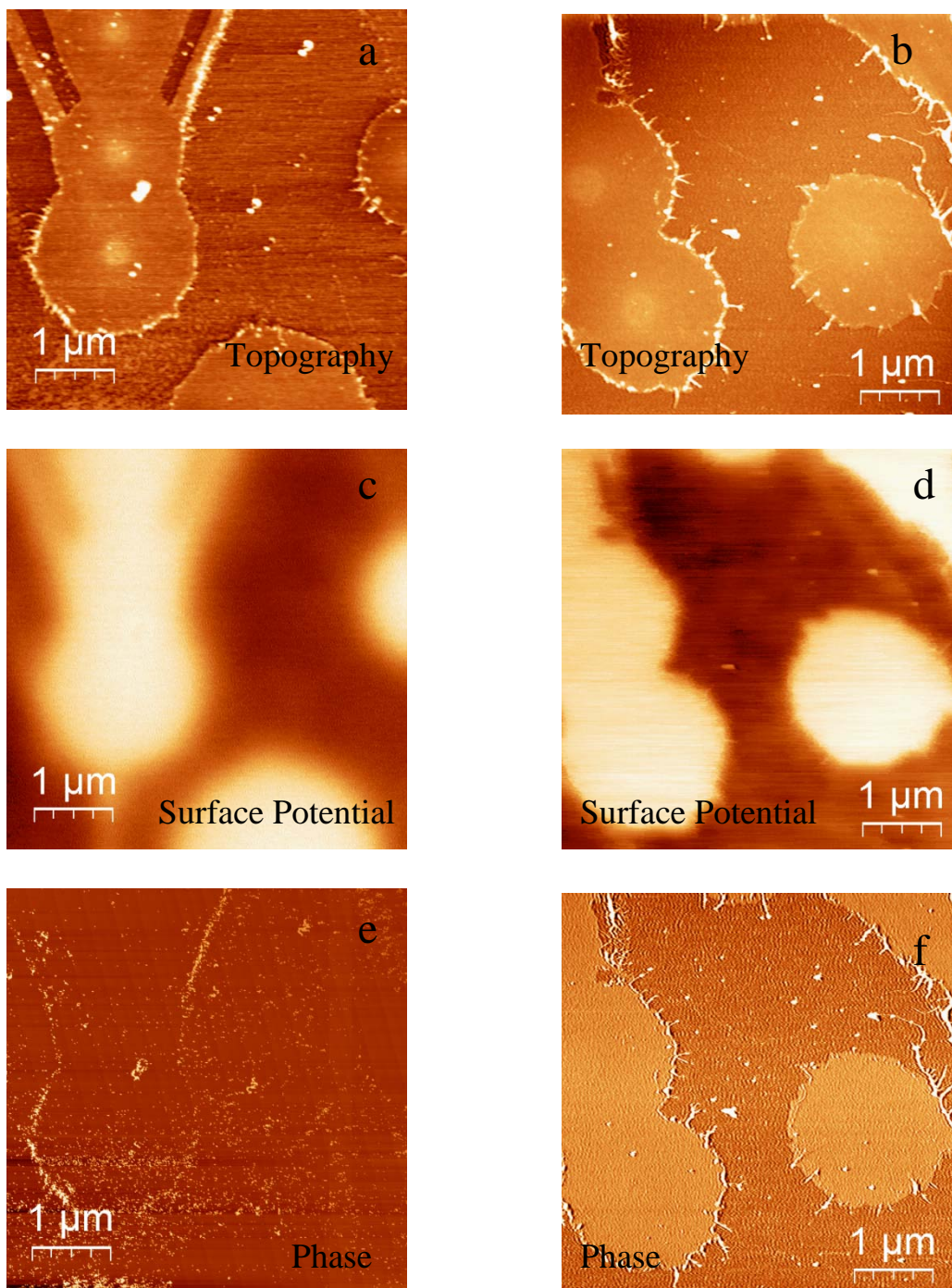


Figure 6-6. The comparison of AFM image obtained through generic pyramid shaped tip and Ag<sub>2</sub>Ga needle tip. (a), (c), (e) are from generic pyramid shaped tip; (b), (d), (f) are from Ag<sub>2</sub>Ga needle tip.



#### 6.2.4 The KPFM characterization of aptamer binding

The characterization was conducted with the Veeco Multimode AFM (J scanner, working in the surface potential mode). The sample was grounded. We used the high-aspect-ratio Ag<sub>2</sub>Ga tip for the characterization. The tip was held at 4 nm above the surface, with a 10V AC amplitude applied on the tip. During characterization, the topography, phase and surface potential images were acquired simultaneously. All images were processed with the WSxM software.

After a tightly packed lysozyme pattern was incubated in the aptamer solution and rinsed with de-ionized water, it was found that the aptamer preferentially binds on the edge of the protein pattern. The AFM image in Figure 6.7 shows a representative tightly packed lysozyme pattern with anti-lysozyme aptamers bound on the pattern edge. In the topographic image (Figure 6.7a), the edge-bound aptamers appear as a white rim with an apparent height of 3nm. The width of the rim is about 30nm, which is much wider than the actual width of a signal-stranded DNA. This widening effect is due to the convolution effect of the tip, which has a typical size of 25nm. In the corresponding surface potential image (Figure 6.7b), the lysozyme patterns appear as bright regions. A side-by-side comparison of the topography and surface potential cross-sectional profiles crossing the pattern edge (Figure 6.7c) illustrates details about the surface potential variation over the pattern edge. From the height cross-sectional profile, the lysozyme region has a height of  $1.4 \pm 0.2$  nm, whereas the lysozyme-aptamer complex (the “bump”) is 1.3 nm higher than the lysozyme. The additional height increase on the edge of protein pattern indicates the aptamer-lysozyme binding. In Figure 6.7c, we plot the cross-sectional profiles of the topography (black line) and the surface potential (red line) together. Since the two profiles correspond to the same position in the image, we can compare the topography change and surface potential change of the same place on the surface side by side. It was shown that the topography profile shows a peak at the place where aptamers bind to lysozyme, whereas the surface potential profile shows a small step on the falling edge. The plots in Figure 6.7c are representative cross sectional plots for the edge of protein pattern with aptamer binding in the image. In the surface

potential image, the edge bound aptamers appear as the characteristic “shoulder” on the lysozyme pattern edge. It was also proven that side-by-side cross-sectional plots of other parts of the pattern’s edge show similar results that the CPD value of the aptamer-lysozyme complex is slightly lower than that of the lysozyme and higher than that of the OTS background.

Table 6-1. The CPD values of lysozyme pattern and the aptamer-lysozyme complex.

	CPD(mV, CPD of OTS =0 mV))	Uncertainty (mV)	N
Aptamer-Lysozyme	58.9	7.9	212
Lysozyme	70.5	4.4	200

To quantify our results, we statistically analyzed the CPD values of the aptamer-lysozyme binding complex and lysozyme pattern, respectively. We first created a cross-sectional profile along the edge of protein pattern in the topography (green line in Figure 6.7a) because the positions of aptamers are clearly shown in the topography image. As a result, the topography cross-sectional profile along the pattern edge precisely covered the aptamer positions. Then, we extracted the X and Y coordinates of every point in this profile. Then, we looked up every surface potential values according to these X and Y coordinates in the surface potential cross section profile. In the exactly same method, we also created another two cross-sectional profiles that are on the lysozyme pattern (blue line in Figure 6.7b) and on the OTS background (pink line in Figure 6.7b), respectively. In order to make a side-by-side comparison, the three cross-sectional profiles created are parallel on the surface potential image. After the quantitative analysis, the CPD values of the OTS background and the lysozyme pattern are obtained. We present the CPD values of the aptamer-lysozyme complex and lysozyme in reference to the CPD of OTS. The results are summarized in Table 6.1.

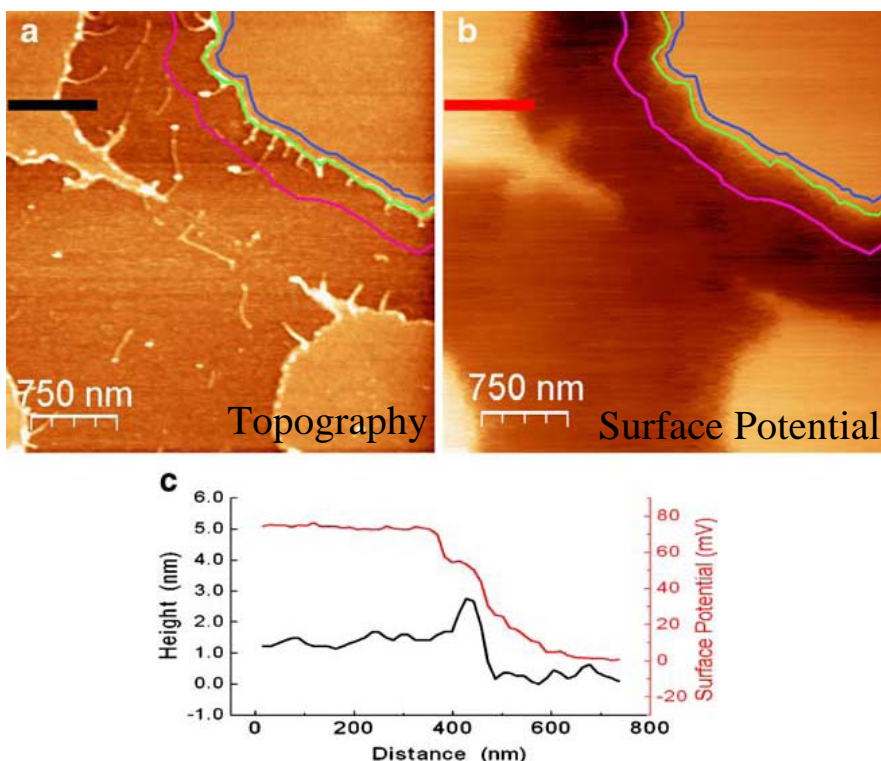


Figure 6-7. The KPFM characterization of lysozyme patterns. a Topography image. b Surface potential image. The CPD value of every point on the pink, green, and blue line was measured. The data were processed and used as the representative CPD values of OTS, aptamer-lysozyme complex and the lysozyme. The results are listed in Table 6.1. c The side-by-side plot of the topography cross-sectional profile (black line) and the surface potential cross-sectional profile (red line). The images were acquired with the Veeco Multimode AFM with the  $\text{Ag}_2\text{Ga}$  tip in tapping mode.

From the Table, we can see that the aptamer-lysozyme binding complex has a lower CPD value than that of the lysozyme pattern. In AFM image of Figure 6.8, we also compare edges of the aptamer-free lysozyme pattern with the aptamer-bound pattern. It was found that the shoulder step shown in Figure 6.6 was not present for the aptamer-free lysozyme pattern edge. Figure 6.8 shows the two surface potential images side by side, which were acquired by using identical imaging parameters and the same AFM tip. The aptamer-bound pattern in Figure 6.8a and the aptamer-free lysozyme pattern in Figure 6.8b are

in the same size and rendered in the same color scale. The CPD levels of OTS in both images are also adjusted to be the same. The green color designates the place where the CPD values are 0-66 mV higher than that of OTS background, whereas the light yellow color means the places where CPD values are 66 mV higher than that of OTS surface. By comparing these two surface potential images, we find that the edge of the aptamer-bound pattern shows a wider green band than that of aptamer-free lysozyme pattern. Therefore, the width of the green band (regions with CPD 0-66 mV higher than that of OTS substrate) could be used to identify the aptamer binding in the surface potential image. The KPFM method provides a straight forward method to detect the aptamer binding without the need of cross-sectional profile and more statistical analysis.

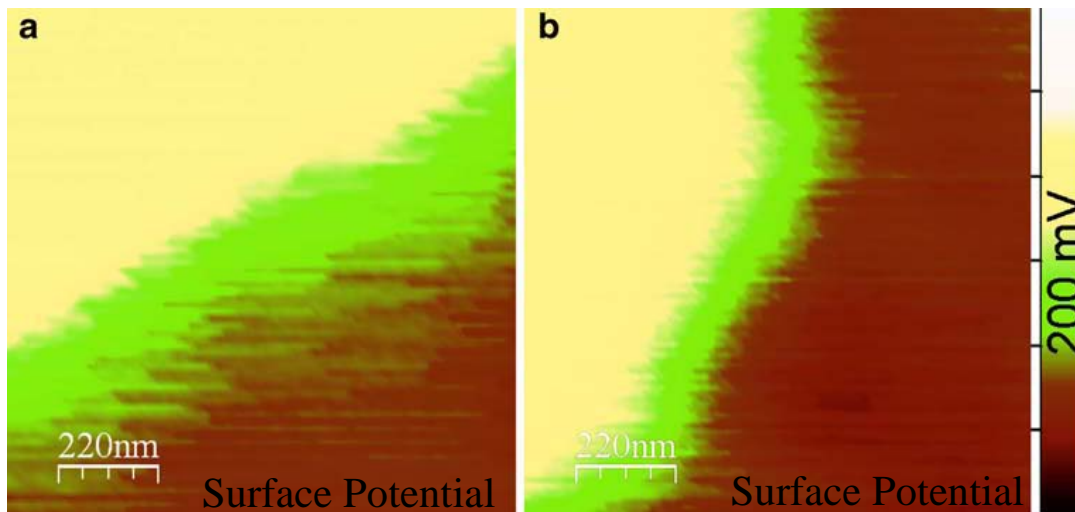


Figure 6-8. A side-by-side comparison of the surface potential images of an aptamer-bound lysozyme pattern (a) and a lysozyme pattern (b). The images are rendered in the same surface potential scale (200 mV). The CPD values of the background OTS in a and in b are also adjusted to be the same. In the figure, the dark brown color designates the OTS background. The images were acquired with the Veeco Multimode AFM with the  $\text{Ag}_2\text{Ga}$  tip in tapping mode

### 6.3 Conclusion of Chapter 6

It was found that the anti-lysozyme aptamers preferentially bound on the edge of the tightly packed lysozyme pattern after the protein coated sample was

incubated in the aptamer solution. In this chapter, we introduce Kelvin Probe Force Microscopy (KPFM), which can measure the contact potential difference (CPD) between the AFM probe and sample surface. It was demonstrated that KPFM was capable of detecting the aptamer-lysozyme binding. From the experiment, we concluded that the CPD value of aptamer-lysozyme binding complex is 12 mV lower than the lysozyme. In addition, by comparing the surface potential images of aptamer-bound and aptamer-free lysozyme pattern, we found the edge of the aptamer-bound pattern showed a wider green band that was the region with CPD value 0-66 mV higher than that of OTS. We demonstrate that KPFM is a straightforward approach to identify the aptamer binding without the need of cross-sectional profile and statistical analysis.

## CHAPTER 7

# APTAMER FIBER ANCHORED ON THE EDGE OF A PROTEIN PATTERN: A TEMPLATE FOR NANOWIRE FABRICATION

### 7.1. Introduction

Nanowires have unique properties not seen in bulk materials.<sup>218</sup> Many proto-type applications like high performance solar cells, waveguides, nanolasers, transistors, and bio-sensors are based on the novel functions of nanowires,<sup>219-222</sup> How to interface freestanding nanowires to existing devices on a solid substrate and how to control the positions of freestanding nanowires on a substrate are the two technical challenges that undermine the development of nanowire-based devices. One approach to address these problems is to use the lithographic pattern to control nanowire positions. Nanowires can be directed to the lithographic patterns either standing up like a forest,<sup>219,223</sup> or lying flat on the pattern.<sup>224,225</sup> However, in many applications such as wires connecting different electrodes, nanowire transistors, and nanowire memory switches,<sup>226</sup> lying down nanowires on the surface are required. Furthermore, these lying down wires must not cross over and collapse over each other. Without manipulating nanowire one-by-one, how to let the nanowires to lie down at designated positions while avoiding the nanowire overlapping remains as a challenging task.

In this chapter, we report a deoxyribonucleic acid (DNA)-based nanotechnology to tackle the problem of interfacing and positioning nanowires. The DNA technology enables us to create complicated structures on the surface.<sup>227-230</sup> Our approach employs the bio-specific recognition of a DNA aptamer, which was discussed in chapter six. The aptamer protein binding has been used to build supramolecular structures at nanoscale.<sup>231,232</sup> In our previous study, it has been proven that when an anti-lysozyme aptamer reacted with a lysozyme lithographic pattern on the surface, the aptamer preferentially bound on

the edge of the lysozyme pattern at first.<sup>233</sup> If the exposure level of aptamer was increased ( i.e. in a buffer solution for a long time), additional aptamers in the solution self-assembled onto the edge-bound aptamer, forming surface-bound aptamer fibers with one end anchored on the edge of lysozyme pattern. Thus a DNA scaffold was formed, which grew from the edge of the protein pattern.

Nanowires originated from the protein pattern could be fabricated on this DNA scaffold. We used these aptamer fibers as a template to fabricate palladium and streptavidin nanowires. These nanowires adsorbed on the surface and never crossed over each other. The bio-specific recognition of the anti-lysozyme aptamer and lysozyme pattern determined that the metal nanowires fabricated from the aptamer fiber scaffold always initiated from the edge of the protein pattern. Thereby, our metal nanowire fabrication approach offers a possible solution to control and interface the nanowire to existing protein-coated patterns.

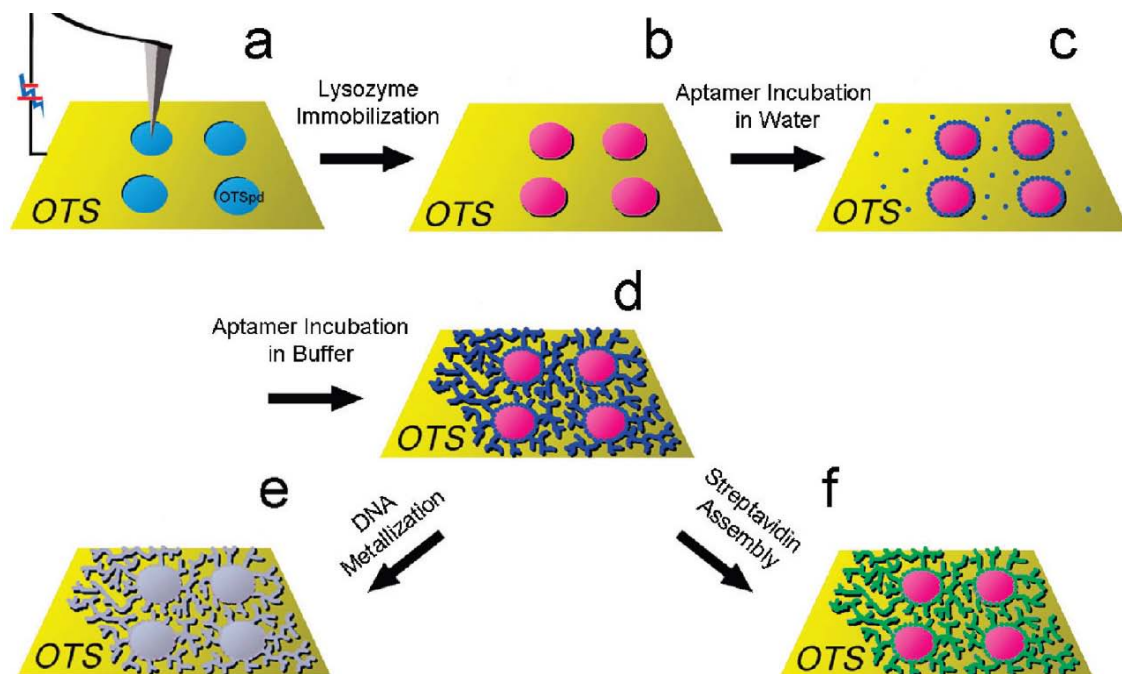
## **7.2. Experimental**

### **7.2.1. Fabrication of aptamer fibers on the edge of protein pattern**

Our experimental procedure was illustrated in Scheme 7.1. We prepare the cross-linked silane film (OTS film) on the hydroxyl-terminated silicon (100) surface from octadecyltrichlorosilane precursor molecules. On the OTS film, some carboxylic acid terminated OTSpd patterns were fabricated through the atomic force microscope (AFM) oxidation lithography (Scheme 7.1a).<sup>122,135,160</sup> These OTSpd patterns direct the shape and dimension of the protein patterns. Next, the patterned sample was incubated in the lysozyme solution, lysozyme molecules could selectively bind on the carboxylic acid-terminated OTSpd surface from solution through the coulombic force. After the sample was rinsed with deionized water and gently wiped with “KimWipe” paper, a clean and tightly packed lysozyme pattern was fabricated on the OTSpd template (Scheme 7.1b). Then, we incubated the lysozyme pattern in a solution of antilysozyme aptamers to form the edge-bound aptamer structure (Scheme 7.1c). After the subsequent AFM characterization revealed that the edge-bound aptamer structure had formed on the lysozyme pattern, we incubated the sample in the same buffer

solution again to form the aptamer fibers (Scheme 7.1d). Finally, the aptamer fibers were used as a template to synthesize nanowires. In the first example, we incubated the aptamer fibers with a solution of palladium acetate and then reduced the Pd<sup>2+</sup> bound on the fibers to form the Pd nanowires (Scheme 7.1e). In the second example, we first fabricated aptamer fibers made of biotin-tagged antilysozyme aptamer. This special aptamer fiber template was then incubated in the streptavidin solution. The streptavidin selectively assembled on the aptamer fiber template, forming streptavidin nanowires (Scheme 7.1f).





Scheme 7-1. The fabrication of nanowires on DNA template: (a) Fabrication of the carboxylic acid-terminated OTSpd pattern (light blue disks) on an OTS surface using the scanning probe deep oxidation lithography; (b) The OTSpd chemical pattern was incubated with a solution of lysozyme. A monolayer of tightly packed lysozyme formed on the OTSpd pattern. (pink disks). (c) Incubation of the lysozyme pattern with a solution of antilysozyme aptamer in water. The aptamers preferentially bound on the edge of the lysozyme disks and formed rings (dark blue rings). Additional aptamers nonspecifically adsorbed on the OTS surface. (dark blue dots). (d) Incubation of the lysozyme pattern with the antilysozyme aptamer in a 10 mM Tris buffer. The nonspecifically adsorbed aptamers self-assembled into fibers (dark blue wires in figure), which anchored on the edges of lysozyme patterns. (e) The aptamer fibers were converted into Pd nanowires (silver wires in figure) through DNA metallization. In the mean time, the lysozyme patterns were also coated with a layer of Pd (silver disks in figure). (f) Streptavidin (green) assembled on the fibers made of biotin-tagged aptamers.

Based on the earlier discovery, we found that these edge-bound aptamer molecules served as anchors for additional aptamer molecules self-assembling into fibers. It was also demonstrated that if the sample was

sufficiently rinsed with deionized water, the nonspecifically adsorbed aptamer on OTS would be washed off the surface, leaving a clean background.<sup>233</sup> Based on this finding, we developed a two-step procedure to fabricate long aptamer fibers anchored on the lysozyme pattern's edge, which is different from our previously reported procedure for the aptamer binding. In the first step, aptamer molecules selectively bound on the lysozyme edges through incubating the sample in 2  $\mu\text{M}$  aqueous solution of antilysozyme aptamer. Incubating in water instead of buffer solution precluded the assembly and precipitation of aptamers. The aptamer molecule is negatively charged in aqueous solution, which makes it difficult to form the optimized structure for target binding. However, the aptamer molecules bound to target lysozyme almost immediately in a 50 mM pH 7 buffer solution. In contrast, we found that it took 10 h for aptamer binding on the lysozyme pattern in water. We speculate that, in water, although a majority of aptamer molecules are not in the optimized structure for target binding, a variety of aptamer conformations coexist and interchange. Therefore, there is still a small fraction of aptamer molecules in the binding conformation. Given enough incubation time, the lysozyme molecules on the edge of the protein pattern will be bound by the aptamer molecules with the right structure.

The AFM image in Figure 7.1a shows that the edge of the protein pattern is higher than the interior of the lysozyme disk, indicating that the anti-lysozyme aptamer molecules bound on top of the lysozyme molecules on the pattern edge. However, to facilitate the subsequent aptamer self-assembly, we deliberately rinsed the sample with deionized water only briefly, leaving many aptamers also nonspecifically adsorbed on the OTS background. Most of these mobile aptamer molecules on OTS are invisible under AFM, because they were dragged by the AFM tip during the scanning. As a result, some horizontal lines are visible in the figure, which were caused by the interactions between weakly adsorbed aptamers on OTS and an AFM tip. When the scanning AFM tip dragged them, a line was generated in the image. This explains the noisy background in Figure 7.1a. Some of the aptamers also formed aggregates, which nonspecifically adsorbed on the OTS background. These aggregates are shown within the white

circles in Figure 7.1a. Aptamer fibers 200-400 nm long also grew from the edge of the protein pattern. They are illustrated in the white box in Figure 7.1a. When the sample was incubated with 2 $\mu$ M aptamers aqueous solution, these aptamer fibers can only grow to 200-400nm long. Longer incubation time did not lead to the further growth of these aptamer fibers. In Figure 7.1c and 7.1d, we show the zoom-in view of the green box in Figure 7.1a. Figure 7.1c and 7.1d are the topography image and the corresponding phase image, respectively. Both images clearly show that the short aptamer fibers grew from the edge of the lysozyme pattern. Figure 1b shows the height profile corresponding to the blue line in Figure 7.1c. The plot in Figure 7.1b indicates that the height of the aptamer fiber is 8 Å. It was also shown that the fibers in the phase image in Figure 7.1d is composed of multiple structural units with size of 20 $\pm$ 2nm. If the base-to-base distance in a fully stretched single-stranded DNA is assumed to be 7.5 Å,<sup>210</sup> a 42-mer signal-stranded antilysozyme aptamer is 31.5 nm long when it is fully stretched. However, if aptamer molecules are linked together through the hydrogen bonding between the complementary based on different aptamer molecules, the base-to-base distance will decrease in the hydrogen bonded section because of some different level of fibers coiling. It made the possible full length of the aptamer molecules smaller than the fully stretched length. On the other hand, the measured height of the fiber in Figure 7.1c is only 8 Å, indicating that the DNA strand is not as coiled as a double-stranded DNA. Hence, the base-to-base distance should be longer than that in double-stranded DNA. Based on these factors, we suggest that the observed periodic 20 nm sized structural unit on the aptamer fiber is the individual anti-lysozyme aptamer. Therefore, it could be concluded that the fiber grown from the edge of the lysozyme pattern is from the assembly of anti-lysozyme aptamers.

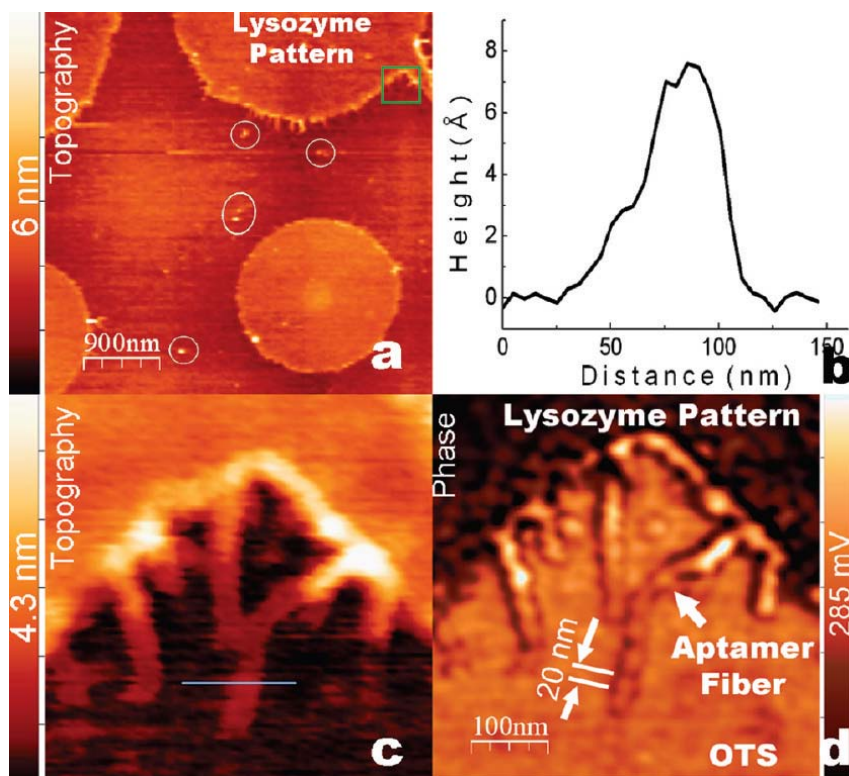


Figure 7-1. (a) Lysozyme patterns (disks) after incubation with antilysozyme aptamers in water: topography,  $4.5 \times 4.5 \mu\text{m}^2$ , the image was acquired using Agilent PicoPlus 3000 in AC mode. Aptamers biospecifically bound on the edge of the lysozyme disks, forming rings over the edges. Aptamers also began to self-assemble from the edge of the disks, forming short fibers. A few aggregates are also observed, as shown inside the white circles. They did not anchor on any of the edges of lysozyme disks. Aptamers also adsorb on the OTS. But due to their small size and mobile nature, they are invisible under AFM. The horizontal lines in the image were caused by interactions between these nonspecifically adsorbed aptamers on the OTS and the AFM tip. When the tip dragged them, a line was generated in the image. (b) The height cross-sectional plot corresponding to the blue line in c, showing the diameter of the fiber is  $8 \text{ \AA}$ . (c,d) Topography and phase images of the region inside the green box in (a):  $500 \times 500 \text{ nm}^2$ , AC mode;  $\sim 20 \text{ nm}$  sized aptamer can be identified in the high-resolution phase image.

In the second step, the sample was incubated in a 10 mM tris (hydroxymethyl) aminomethane (Tris), pH=7.0, buffer for 10-72h at 25 °C. Then the sample was incubated and rinsed in deionized water at 25 °C. After that, we observed the formation of branched, long fibers up to tens of micrometers, which were formed from the non-specifically adsorbed aptamer molecules on OTS background. Longer incubation time led to the formation of longer fibers, which were anchored on the edge of the lysozyme pattern, as shown in Figure 7.3. Occasionally, there are some trace amounts of isolated orphan fibers that are not anchored on the fibers grown from the edge of protein pattern on the surface. They will disappear after additional cycles of rinsing using the buffer solution: they were either captured by other edge-anchored fibers or rinsed off the sample surface. The fiber's length is only limited by the space between the lysozyme discs, as shown in Figure 7.2. When most of the branches are as close as ~20 nm, the fibers stop growing. In contrast, the fiber grown in an unconfined area in Figure 7.3 could reach to tens of micrometers in length. The diameter of the fiber is not even. Fibers in the terminal branches are thinner, with a typical diameter of 1-2 nm, whereas fibers in the "mainstream" have a typical diameter of 5-6 nm. These fibers adopt the fractal shape. Under our preparation conditions, different branches can be as close as 20 nm, but the fibers in one branch do not connect to fibers from other branches, nor do they cross over or collapse over each other. The position of the fibers on the surface would be slightly changed if these fibers are incubated in buffers with higher ionic concentrations (>50 mM).

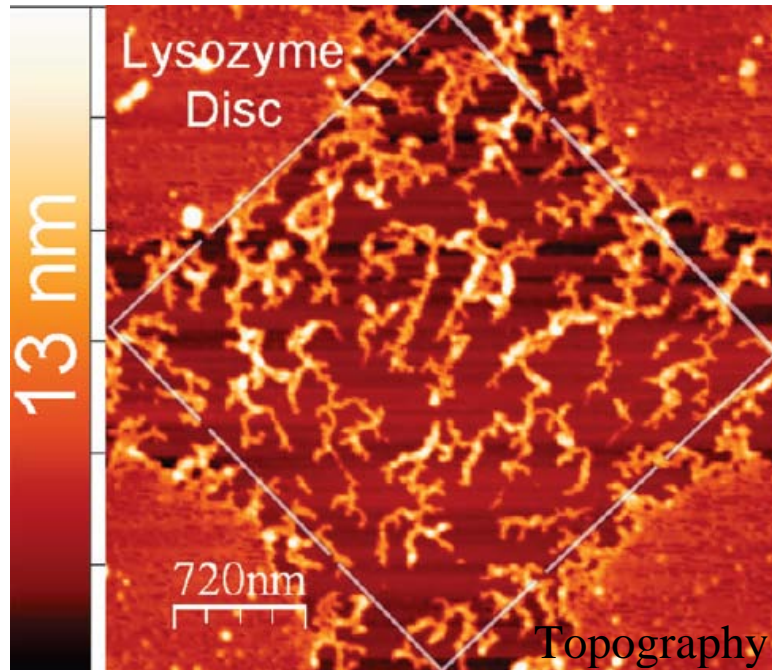


Figure 7-2. The topography image of aptamer fibers anchored on the edge of lysozyme protein patterns with the spatial limitation from the protein patterns around

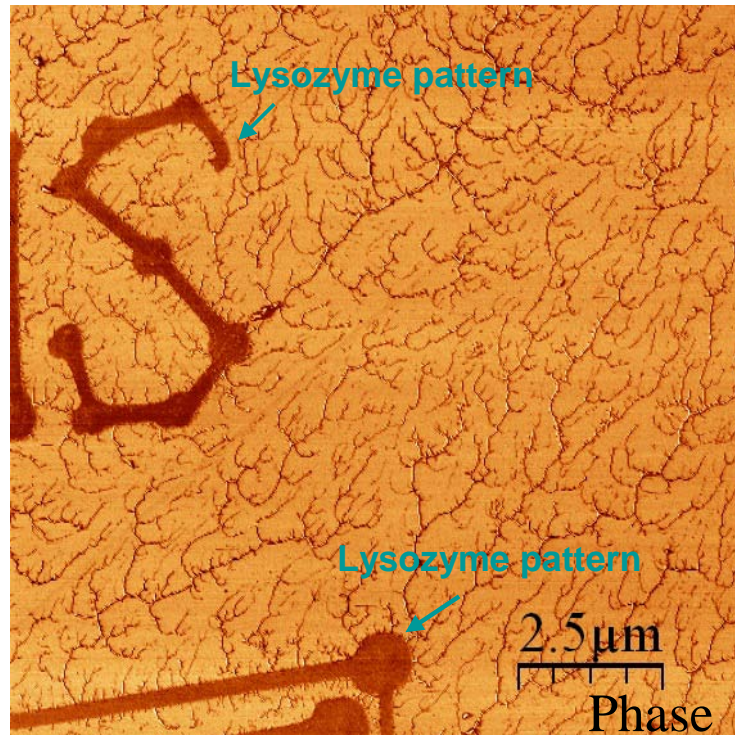


Figure 7-3. The phase image of long aptamer fibers anchored on the edge of lysozyme protein patterns without the spatial limitation

### 7.2.2. Characterization of aptamer fibers on the edge of protein pattern

After the lysozyme protein pattern was incubated in the anti-lysozyme aptamer solution and rinsed in the buffer solution, some fractal-shaped aptamer fibers could be found to grow on the edge of protein pattern. We suggested that these fibers were made of DNA.<sup>233</sup> In our control experiment, the lysozyme pattern was incubated in a blank Tris buffer. It was shown that no fiber was generated unless the aptamer was added into the Tris buffer. The observed fibers that were several micrometers long had a 1-5 nm diameter. Because an anti-lysozyme aptamer molecule (42-mer) is ~20 nm long and 1-2 nm in diameter, the fibers must consist of many aptamers self-assembled together, as we had observed in Figure 7.1d.

We speculate that the driving force of the self-assembly is the intermolecular hydrogen bond between single-stranded aptamers. To test our hypothesis, we performed control experiments with two oligonucleotides: a randomly generated single-stranded 42-mer DNA (random sample, sequence 5'-TAT GCT AAA CCT TAC AAG TTG GAA GTC GAG CGT TGA AGC AGG-3') and a single-stranded 50-mer DNA that is composed of only the guanine (polyG). They are both obtained from Operon. Results showed that the random sample also formed fibers on the surface, although these fibers could not anchor on the edge of the pattern. As a comparison, we did not observe any fibers formation for the polyG case. For both single-stranded DNAs that form fibers (the anti-lysozyme aptamer and the random sample), we found that there were complementary regions in their sequences for the interstrand base pairing. Figure 7.4 and Figure 7.5 are the analysis of complimentary sequences in the anti-lysozyme aptamer and the random aptamer, respectively. On the images, the complimentary sequences are marked with yellow "x" sign. The image is generated via the on-line sequence analysis tool from Operon Inc. In contrast, the polyG was unable to find any complementary nucleotide (the cytosine) on another polyG. Therefore, the polyG can not self-assemble into fibers without hydrogen bond existing between two polyG strands. Furthermore, to test our hypothesis, we incubated the fibers of the anti-lysozyme aptamer in water at





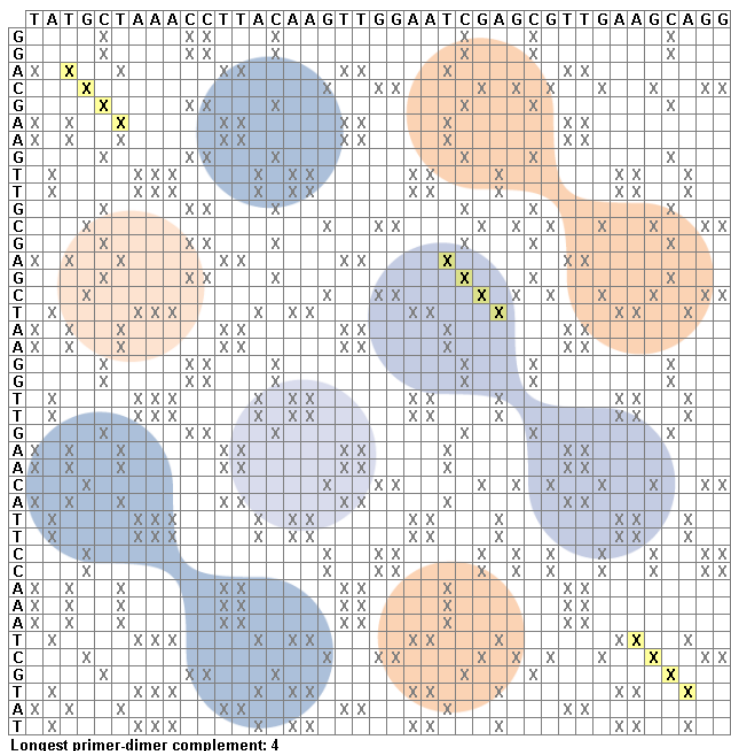


Figure 7-5 The analysis of complimentary sequences in the random aptamer

Finally, to confirm the observed fibers originated from the DNA assembly, we conducted two more experiments. We incubated the fibers in deionized water for 72h. The fibers remained intact. This fact rules out the possibility that the fiber originated from salt drying patterns, because the salt would be soluble in water and the salt pattern would disappear after incubation in water. We also stained the fiber with a 10 mM solution of ethidium bromide (EtBr), which is known to selectively bind to DNA and yields fluorescence upon excitation.<sup>234,235</sup> After rinsing, we imaged the same region on the sample using AFM and a fluorescence microscope. The AFM topography image (Figure 7.6a) and the fluorescence microscope image (Figure 7.6b) of the fibers matched exactly, as shown in Figure 7.6c. The exact matching indicates that the fluorescence signal is from the fiber. Therefore, the fiber is made of DNA. Here, the fluorescent image of aptamer fibers was acquired using the Nikon fluorescence microscope N55i.

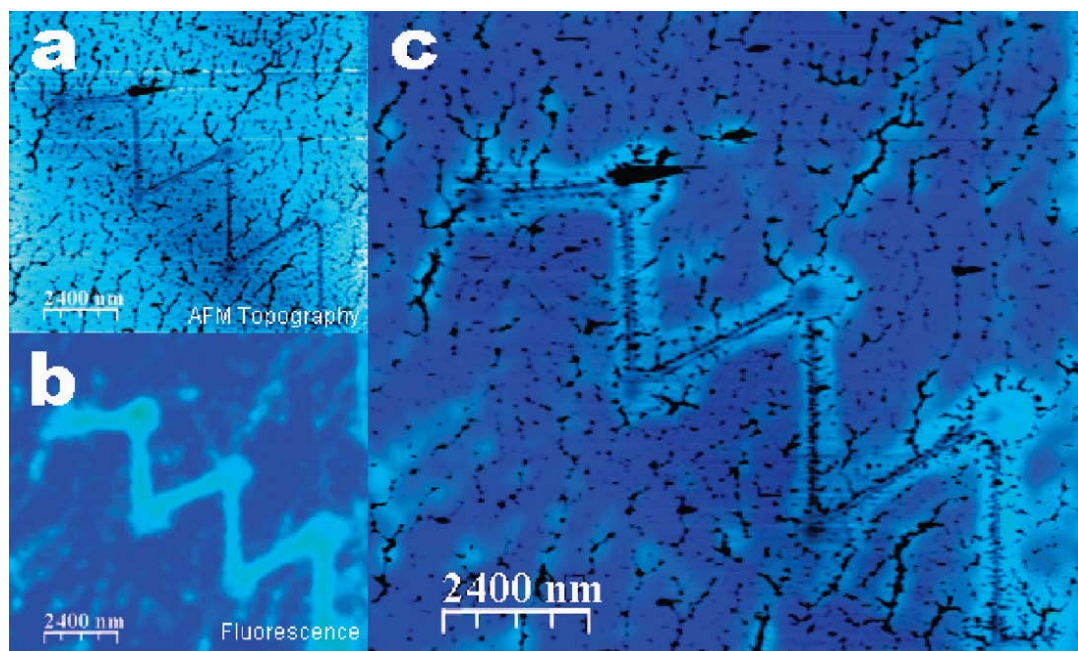


Figure 7-6. Fluorescent image of ethidium bromide-stained aptamer fibers (bright) matches exactly with the AFM image of aptamer fibers (black) of the same region. (a) AFM topography image of aptamer fibers grown from a zigzag-shaped lysozyme pattern. The image is rendered in the reverse height scale. Black represents high surface features, while a low surface feature corresponds to the bright color. (b) Optical fluorescent image of the same region. The fluorescent image was acquired using Nikon Eclipse N55i microscope, with the G-2A filter, which selectively collected fluorescence signal from ethidium bromide from 550-600 nm. (c) AFM and fluorescent images are overlaid together. The perfect matching indicates that the observed fibers are made of DNA, which can bind ethidium bromide. (Note: Some aptamer fibers in the AFM topography images 2a and 2c appear as broken. In fact, at higher height resolution, these fibers are continuous.)

Similar fiber-shaped and network-shaped structures formed by the DNA self-assembly have been reported previously.<sup>211,236,237</sup> Compared with these previous reports, the aptamer fibers fabricated in our approach can recognize and grow from the edges of the pattern. Such spatial control originates from the bio-specific recognition between the anti-lysozyme aptamer and the lysozyme

molecules on the edge of pattern. In contrast, when the lysozyme pattern was incubated with the random DNA sample, short fibers and clusters also formed. But they only non-specifically adsorbed on the OTS background. They did not anchor on the edge of the lysozyme pattern. Therefore, the fibers formed by the random sequence have no recognition ability. After the sample was incubated in deionized water at 25 °C for 8h and then rinsed with water for three times, these non-specifically adsorbed fibers were rinsed off the sample, leaving only the protein pattern on the surface. For the fibers formed from the anti-lysozyme aptamer, after such procedure, they remained because these fibers have anchored on the edge of the lysozyme pattern, where aptamer bound to the lysozyme molecules on the edge through the bio-specific recognition.

### **7.2.3. The diffusion-limited aggregation (DLA) theory**

The diffusion-limited aggregation (DLA) theory can be used to explain the mechanism of the fiber formation.<sup>238</sup> Experiments and simulations have shown that DLA generates the fractal shape which is very similar to the observed aptamer fibers.<sup>239-241</sup> We observed that when aptamers reacted with the lysozyme pattern, some aptamer molecules specifically bound on the edge of the lysozyme pattern, while other aptamers non-specifically adsorbed on the OTS background that could randomly walk around the surface. The edge-bound aptamers served as seeds for the subsequent DLA process. During the Tris buffer incubation, when a mobile non-specifically adsorbed aptamer encountered the seed, the seed can capture it. Thus, a dimer was formed on the edge of the protein pattern. Similarly, when the third aptamer randomly walked into the dimer, it was captured by the dimer to form a trimer. As such process repeated, the assembly grew longer, leading to a fractal shape.

There are two types of DLA. One is the classical Witten-Sander type,<sup>238</sup> in which only one seed exists during the growth of a branch and all particles assemble to a branch one by one. The other type is the cluster-cluster model (CL-CL), where particles (aptamers in our case) also self-assemble into small freestanding clusters.<sup>242</sup> Besides the mobile particle that can randomly walk on

the surface, these clusters also can randomly walk on the surface and be captured by the edge-bound seed aptamers. The final shape formed by the CL-CL DLA is also the fractal shape. The difference between these two types of DLA is that the fractal formed by Witten-Sander type DLA is more flowerlike with a fractal dimension of 1.7 in the two dimensional case,<sup>241</sup> while the fractal formed by the CL-CL DLA is more wire-like, with a fractal dimension between 1.4-1.5.<sup>242</sup> Because the fractal dimension reveals the mechanism of the formation of fractals, we use the perimeter-area method to calculate the dimension of the fractal formed by aptamer fibers to study how the aptamers assemble to a fiber.<sup>243</sup> In the perimeter area method, the perimeter ( $P$ ) and the area ( $A$ ) of a fractal pattern are measured first. The  $P$  and  $A$  are related by the formula

$$p = \alpha D' A^{D'/2} \quad (1)$$

Where  $\alpha$  is a constant and  $D'$  is the fractal dimension. Therefore,

$$\log_{10} p = \frac{D'}{2} \log_{10} A + \text{constant} \quad (2)$$

Figure 7.2 is a representative fractal pattern formed by aptamer fibers. These fibers grew from edges of the four lysozyme discs, which locate at the four corners of the image. We analyzed the aptamer fractal inside the white box in Figure 7.2 and plotted  $\log_{10} p$  against  $\log_{10} A$  of the fractal patterns in Figure 7.7. Equation 2 indicates that the slope of the least-squares fitting line (the red line in Figure 4) is  $D'/2$ . Thus, from this plot, the dimension of the aptamer fiber fractal is calculated to be  $1.44 \pm 0.04$ . This value suggests that the fiber formation is in line with the CL-CL DLA mechanism. Not only can a single aptamer randomly walk on the surface and then join to the fiber already anchored on the edge of a lysozyme pattern, but also aptamers can self-assemble into short freestanding fibers (clusters) on the OTS background, and these fibers then can randomly walk and be captured by the fibers that had already anchored from the pattern edge. In fact, AFM image also support this conclusion from the fractal analysis. When lysozyme patterns were incubated with the solution of aptamers, after rinsing, the AFM image revealed that a small amount of isolated short fibers (aggregates) still existed. The white circles in Figure 7.1a show the positions of these aggregates. They are weakly adsorbed on the surface. Rigorous rinsing

can minimize the presence of these freestanding aggregates from the surface. These short isolated fibers are the “clusters” under the CL-CL DLA mechanism, which might be captured by a pattern edge anchored fiber and thus be incorporated to form a longer fiber if the sample was incubated in the Tris buffer for a longer time.

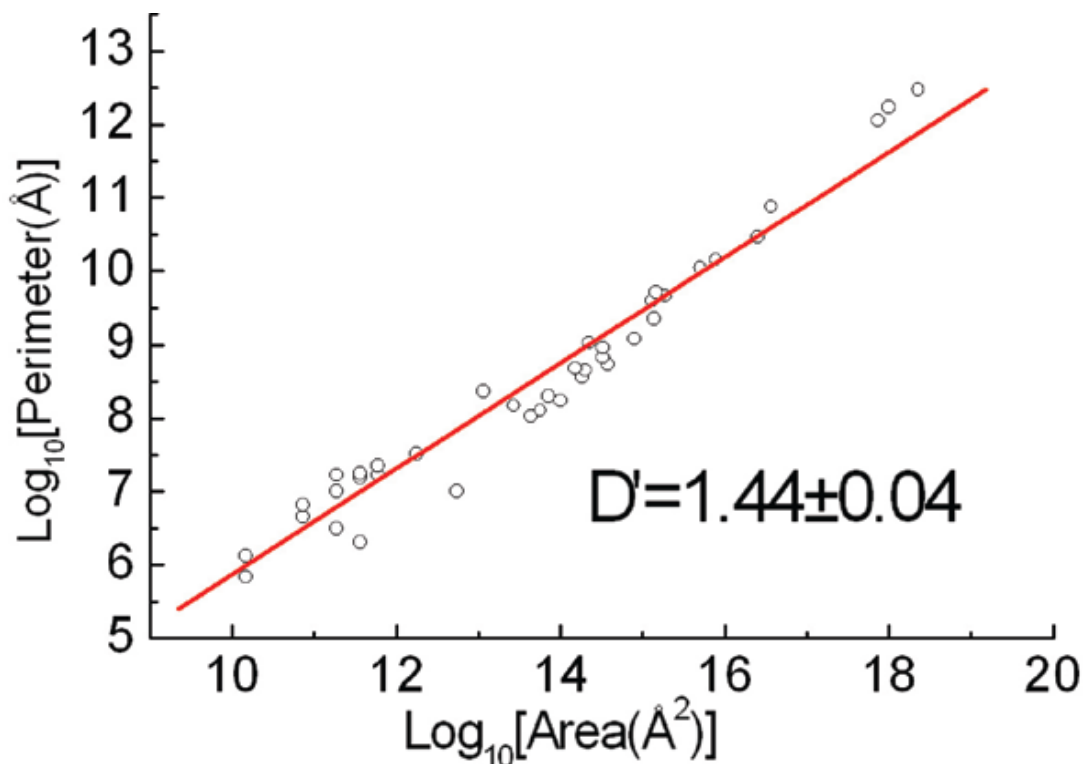


Figure 7-7. Aptamer fibers within the white box in Figure 7.2 were analyzed by the perimeter-area method to calculate the fractal dimension. The logarithm of perimeter was plotted versus the logarithm of area. The red line shows the least-squares linear fitting of the data points.

Under the two-dimensional DLA mechanism, an aptamer molecule can not be captured by two branches at the same time. Therefore, different aptamer fibers from two branches will never connect to each other, nor do they cross over or collapse over each other. Therefore, the mechanism provides an explanation of the AFM data, in which the aptamer fibers from different branches never connect or cross over each other.

#### **7.2.4. The aptamer fibers were converted into Pd nanowires through DNA metallization**

The aptamer fibers anchored on the edge of a pattern can be converted to metal nanowires through DNA metallization.<sup>244-247</sup> Pd nanowires can be fabricated through the reduction of DNA-bound Pd<sup>2+</sup>,<sup>248-250</sup> which can be conducted in three chemical reduction cycles. Firstly, 10 mg palladium acetate was dissolved in 4 mL deionized water. After 3 minutes of ultrasonication, the solution was centrifuged at 9000 g for 5 minutes to remove any insoluble particles. The solution was then diluted to 30% of the original concentration. Next, aptamer fibers were incubated with the diluted palladium acetate solution for 5 minutes. After rinsing, the sample was then soaked in the reducing solution for another 5 minutes, which includes 250 mg/L sodium citrate, 250 mg/L 85% lactic acid and 25 mg/L borane dimethylamine. This is the first reduction cycle. In the second cycle, the same sample was incubated in the palladium acetate solution for an addition 15 minutes and then it was soaked in the reducing solution for 15 minutes. In the third cycle, we added another 15 minutes for palladium acetate incubation and reduction, respectively.

The AFM image in Figure 7.8a-d shows the same region of aptamer fiber before and after the first, second, and third cycle of the metallization process. After the reduction, most fibers maintained the basic structure and morphology. In Figure 7.8e, we plotted the height cross-sectional profile of the same part of an aptamer fiber before and during the metallization process. After the first, second, and third cycle of reduction, the height of the aptamer fiber increased from 60 to 90, 100, and 120 Å, respectively. Comparing the images from Figure 7.8a-d, there were additional fine fibrils attached to the thick palladium wires. They formed from the trace remnant non-specifically adsorbed aptamer molecules on the OTS background. During the Pd<sup>2+</sup> reduction process, the continuous incubation process also facilitated the further assembly of these remnant non-specifically adsorbed aptamer molecules. The fiber's full width at half-maximum (fwhm) increased from 280 Å before the metallization to 670 Å after three cycles of reduction.

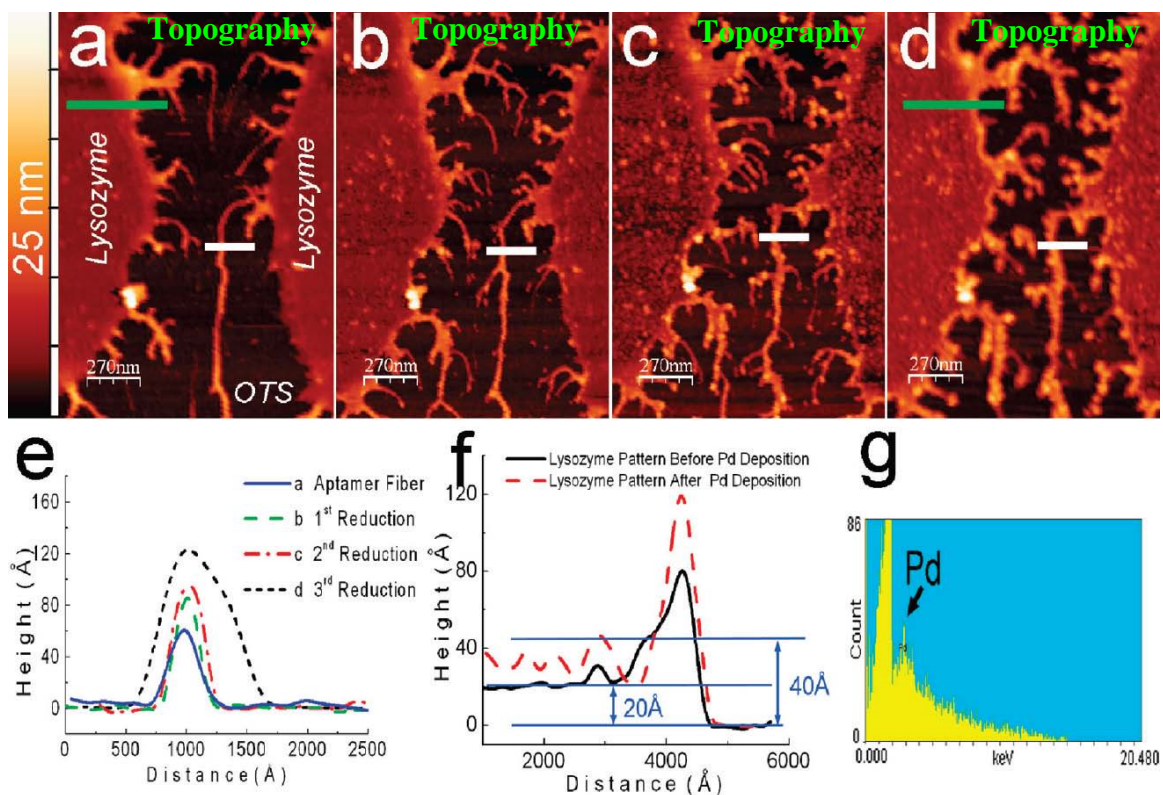


Figure 7-8. Aptamer fibers were converted into Pd nanowires. (a-d) The same region before the metallization and after the first, the second, and the third cycle of metallization. The height cross-sectional profiles of the same position on an aptamer fiber in (a), (b), (c), and (d) were plotted in (e). (f) Height cross-sectional profiles of the lysozyme pattern before the Pd deposition (black solid line) and the same place after three cycles of Pd depositions (red dash line). The black (solid) line and the red (dash) line correspond to the green bar in (a) and (d), respectively. (g) EDX spectrum of the sample. The peak at 2.8 keV confirmed the existence of Pd on the surface.

In the AFM image of Figure 7.8a, there are also faint white spots scattering around on the lysozyme disks. These spots are the aptamer molecules bound to the lysozyme molecule inside the patterns. Although the aptamer molecules preferentially bind to the lysozyme molecules on the edge, aptamer molecule still can bind to the lysozyme molecule interior of the patterns after a enough long time incubation. The preferential edge-binding effect could be understood that a few aptamer molecules could bind interior lysozyme when the

edge positions around the patterns were fully occupied. Therefore, the palladium could also selectively deposit on the lysozyme disk during the metallization process because of the existence of those aptamer molecules inside the lysozyme disk. From Figure 7.8a-d, it can be seen that the Pd particles accumulated on the lysozyme disk to form a Pd film on the top. The AFM image In Figure 7.8f shows the height cross-sectional profile of a lysozyme disk before the Pd deposition and after the three cycles of Pd reduction. The lysozyme is 20 Å above the OTS background before the metallization which is similar to our previous result.<sup>208</sup> From the height cross-sectional profile, we can see the height of disk is increased to 40 Å above the OTS background after the Pd reduction process, indicating that a layer of 20 Å Pd was deposited on the lysozyme surface. The AFM image also shows that the amount of palladium deposited on the lysozyme disk is much less than that on the fibers. It is because that the density of the aptamer molecules on the pattern disk is relatively low before the palladium deposition. As a result, a few negatively charged aptamers were covered on the disk area and thus the amount of the Pd<sup>2+</sup> bound on the fibers is insignificant.

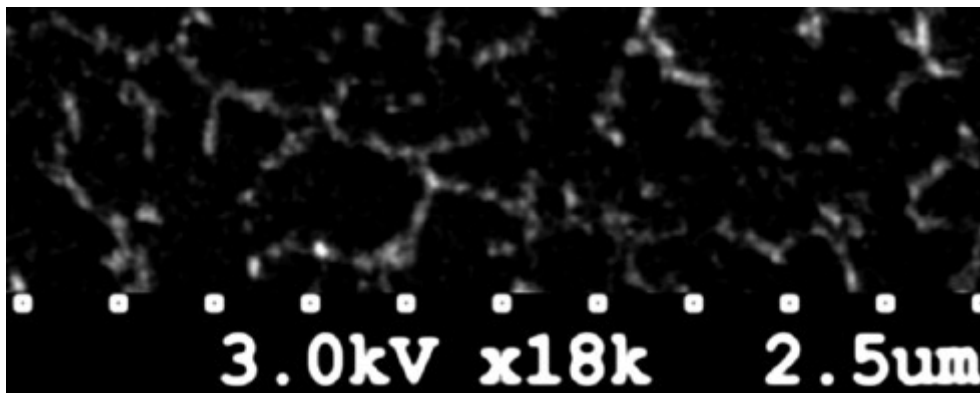


Figure 7-9. SEM image of Pd nanowires on the aptamer fiber template.

Figure 7.9 shows the scanning electron microscope (SEM) image of the Pd nanowire after three cycles of reduction. The diameter of the Pd nanowire is 20-50nm, which is consistent with the AFM results. It was shown that the Pd nanowire is made of Pd nanoparticles fused together and the whole wire is continuous. These characteristics are similar to the published results.<sup>246,248,251</sup>



In the control test, the aptamer fibers were incubated with the reducing solution, but skipped the previous PdAc<sub>2</sub> incubation step. The fibers and lysozyme patterns in the control test remained the same. There is no change of the fiber's width and height before and after the incubation. The Pd nanowires were also characterized using a Hitachi SE-3200 scanning electron microscope for energy-dispersive X-ray spectroscopy (EDX) analysis. The EDX analyzes the composition of elements within a volume of a few cubic micrometers under the electron beam impacted area. In the EDX spectrum shown in Figure 7.8g, the peak at 2.8 keV confirmed the presence of Pd on the surface besides an overwhelming peak of silicon. Therefore, it could be concluded that the palladium nanowires that originated from the protein pattern edges have been fabricated. These wires are highly branched and never connect or cross over each other. Conveniently, the lysozyme patterns were also coated by layer of metal during the DNA metallization. Thus, the pattern can be directly used as electrodes attached with metal nanowires which could be used as nanosensors and nanoelectrodes.

### **7.2.5 Streptavidin assembled on the fibers made of biotin-tagged aptamers**

In this experiment, the biotin-tagged anti-lysozyme aptamer instead of bare anti-lysozyme aptamer was used to fabricate the branched long aptamer fibers. The sequence of the biotin-tagged anti-lysozyme aptamer is 5'-ATC TAC GAA TTC ATC AGG GCT AAA GAG TGC AGA GTT ACT TAG-biotin-3', which was from Operon. The biotin-tagged aptamer fibers were fabricated according to the same procedure mentioned above. Then, the sample was incubated in 4 µg/mL streptavidin in 25 mM pH 7.0 HEPES buffer for 1h. After that, the sample was rinsed in the 25 mM pH 7.0 HEPES buffer and deionized water. Through the AFM image characterization, we can compare the same aptamer fiber before and after the incubation. It was found that the biotin-tagged aptamer fibers grew higher, indicating the streptavidin binding. To further test the streptavidin binding, we incubated the biotin-tagged aptamer fiber with the fluorescein isothiocyanate (FITC) tagged streptavidin. The same region on the surface was imaged by both

AFM and a fluorescence microscope, respectively. In the imaging of fluorescence microscope, we chose the FITC-optimized filter which can block the fluorescent signal from DNA and only selectively collected the fluorescence signal from FITC. Figure 7.10a shows the AFM topography image of the fibers (black in the image) overlaid on the fluorescent image taken by the same Nikon fluorescence microscope N55i (fluorescence signal is bright). It was proven that the fibers in the AFM topography image are always overlapped with bright bands in the fluorescent image, albeit the width of the bright band is about 500 nm, which approaches the diffraction limit of the optical microscopy. Figure 7.10a shows that the two images match exactly, indicating that the fluorescence is from the fibers. Therefore, the streptavidin indeed bound on the aptamer fibers that assembled from the biotin-tagged anti-lysozyme aptamer.

Figure 7.10c and 7.10d are the topography and phase zoom-in views of the yellow box in Figure 7.10a, respectively. This high-resolution AFM phase image resolves the aptamer fiber (black in the phase image) and the streptavidin molecules (bright dots on the fiber). The discrete streptavidin molecules can be resolved, as pointed by the white arrows in Figure 7.10c. The size of a single streptavidin tetramer in the Figure 7.10c is around 10nm, which is slightly larger than the actual dimension of a streptavidin tetramer ( $7.3 \times 8 \times 4.4$  nm, determined from the crystal structure).<sup>252</sup> We explain this difference as the tip convolution effect. Figure 7.10b plots the height cross-sectional profile along the blue line in Figure 7.10c. The plot shows that the streptavidin molecule is 4 nm above the aptamer fiber, which is consistent with the reported 3.5-4.5 nm height values measured by AFM.<sup>252-254</sup> Data in Figure 7.10 confirm that branched, long nanowires of streptavidin were fabricated on the aptamer template, which has one end anchored on the edge of the protein pattern.

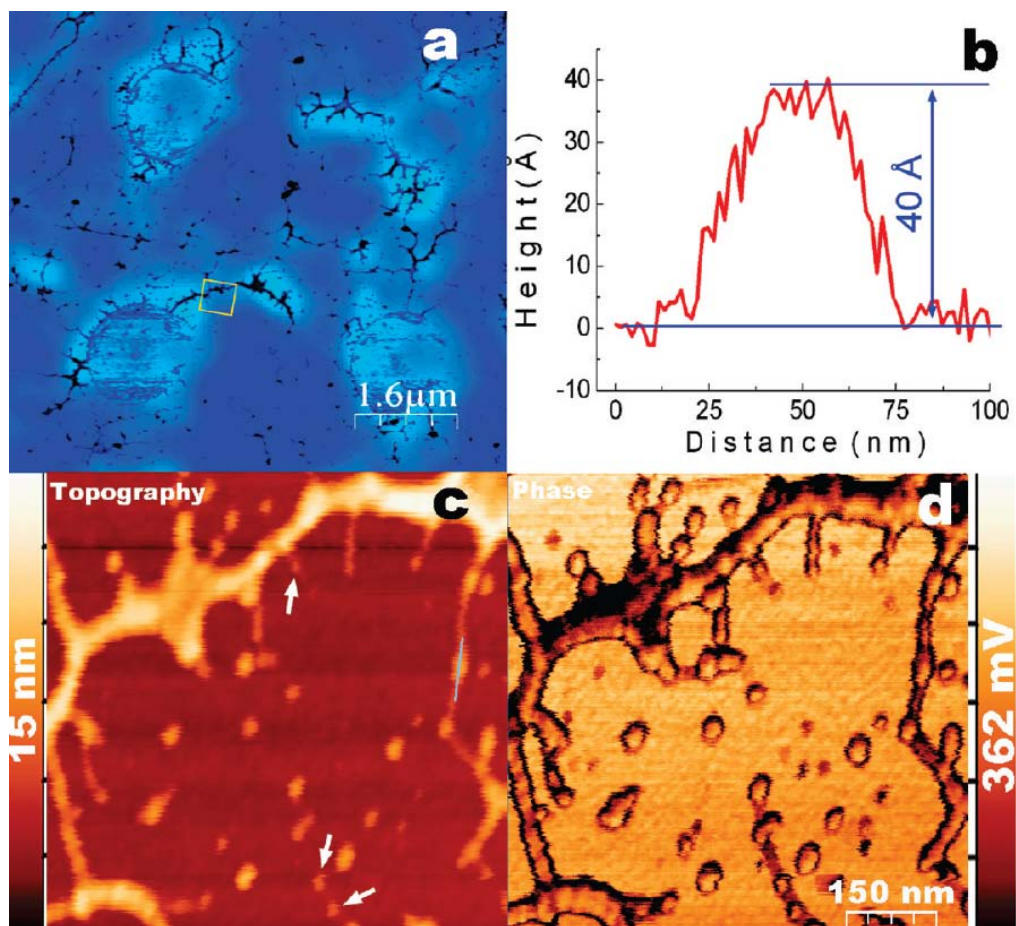


Figure 7-10. FITC-labeled streptavidin assembled on the biotin-tagged aptamer fibers. (a) AFM topography image of the FITC-labeled streptavidin assembled on the biotin-tagged aptamer fibers (black) overlaid on the fluorescent image (bright) of the same region. The fluorescent image was acquired using Nikon Eclipse N55i microscope, with the FITC optimized filter, which selectively blocked the fluorescence signal from DNA. The matching of the AFM and fluorescent images indicates that FITC-labeled streptavidin molecules bind on the fibers made of biotin-tagged antilysozyme aptamer. (b) Height cross-sectional profile along the blue line in (c), showing the streptavidin molecule is 40 Å higher than the aptamer fiber template. (c,d) High-resolution AFM topography and phase images of the aptamer fibers in the yellow box in (a). The white arrows in (c) show the positions of individual streptavidin molecules bound on the aptamer fiber. (AC mode, 750 x 750 nm<sup>2</sup>; Note: Some aptamer fibers in (a) appear as broken. In fact, at higher height resolution, these fibers are continuous.)

### 7.3. Conclusion of chapter 7

It was found that aptamer molecules could form fibers up to tens of micrometers long. Unlike the *ad hoc* DNA assembly in solution, which forms DNA networks upon drying on surface, the aptamer self-assembled into long fibers *via* surface DLA process. This one-dimensional assembly approach generates long DNA wires without the need of purifying long  $\lambda$ -DNA or synthesizing several thousand base pair-long DNA strands.

We successfully fabricated nanowires than anchored on the edge of protein patterns through the bio-specific recognition between the anti-lysozyme aptamer and lysozyme. The bio-specific recognition of the aptamer fiber controls the position of nanowires. These aptamer fibers could help to interface with other existing surface structures like DNA origamis, nanowires, electrodes, and transistors. Due to its DNA nature, additional tags, such as -SH or other aptamer, can be incorporated into the current sequence of the aptamer. Thus, the engineered fiber scaffold can be used to direct the subsequent assembly on the aptamer fiber template.

In summary, we developed a new approach that improved the spatial control and interfacing capability of DNA assemblies by exploiting the bio-specific recognition of aptamer.

## CHAPTER 8

### CONCLUSIONS AND FUTURE PROJECTS

#### 8.1. Conclusions

We fabricated a tightly packed lysozyme pattern on the carboxylic acid-terminated chemical patterns (OTSpd), which were created on OTS surface by using AFM local oxidation lithography method. Protein molecules were immobilized onto the carboxylic acid-terminated patterns through the Coulomb charge attraction. The “paper swabbing” approach removed all non-specifically adsorbed protein molecules on the OTS background. Through the binding reaction with polyclonal antibodies on the surface, it has been concluded that our protein pattern fabrication approach can generate a bio-active protein pattern with a clean background without the need of the anti-fouling surface or repetitive rinsing.

Additionally, we found that the antibodies preferentially bind to the edge lysozyme molecules at the beginning of the reaction, since they have better spatial accessibility and flexibility. Moreover, the topography of the immobilized protein pattern affects the antibody binding direction. It has been demonstrated that the antibody binding to the edge lysozyme molecules on the half-buried pattern started from the top but the binding on the extruded pattern started from the side because of their different spatial accessibility. The “edge effect” potentially can lead to an effective means to improve the activity of the immobilized enzymes. If the coverage of an immobilized protein remains the same, a protein nanoarray has more protein molecules on the edge than a protein microarray. Therefore, reducing the protein pattern feature to the nanoscale will improve the overall binding of immobilized proteins toward antibodies.

Anti-lysozyme aptamers are also found preferentially bound on the edge when they reacted with a tightly packed lysozyme pattern. In addition, we demonstrated that KPFM was capable of detecting the aptamer-lysozyme binding. The aptamer-lysozyme binding complex has a CPD value approximately

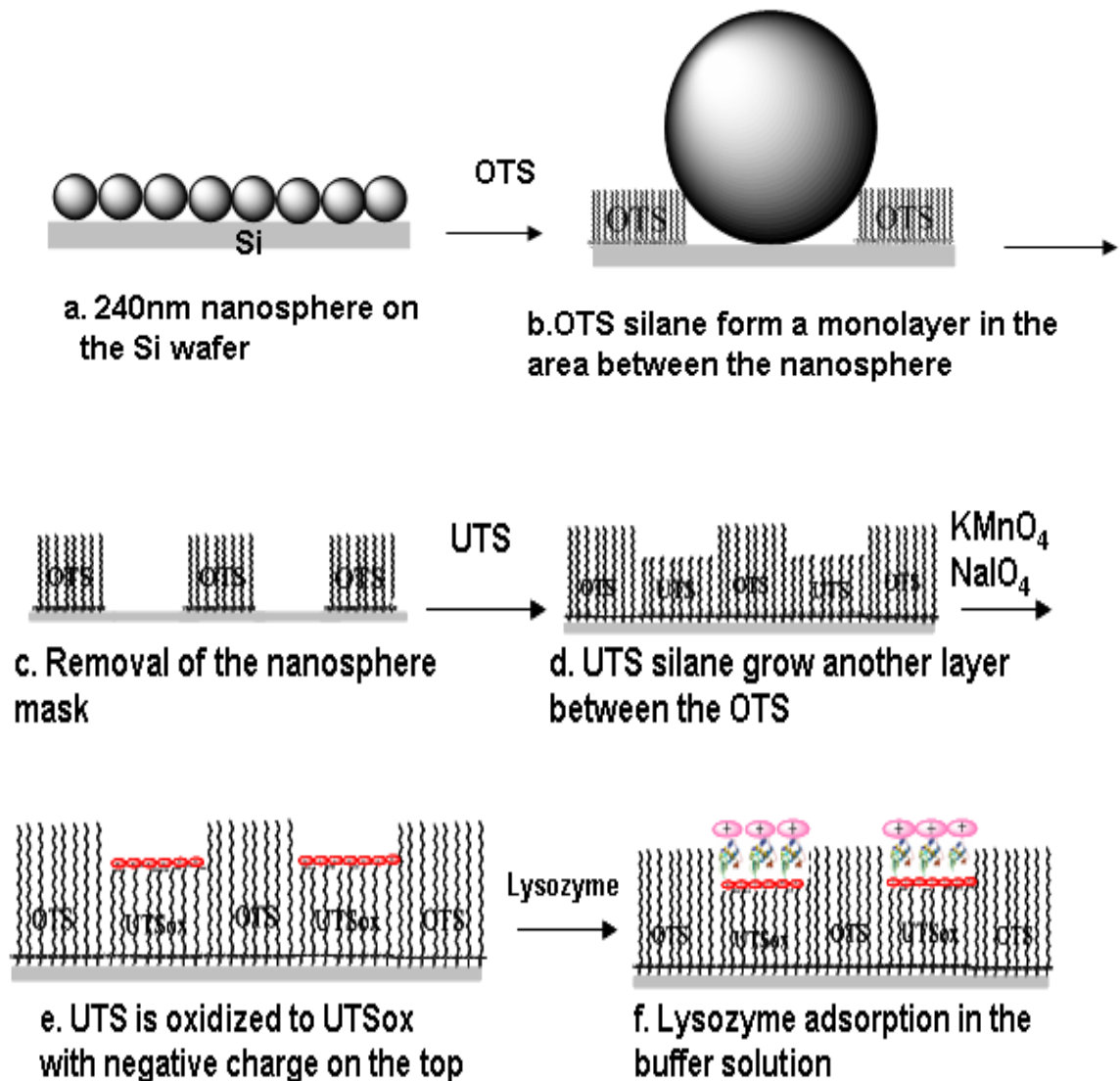
12mV lower than the lysozyme. The aptamer molecules can also form fibers with tens of micrometers long *via* surface DLA process. The aptamer fibers anchor specifically on the edge of protein patterns, which originates from the biospecific recognition between the aptamer and its target protein. Once these edge-bound fibers have formed, they can serve as scaffolds for further assembly processes. We used these aptamer fibers as templates to fabricate palladium and streptavidin nanowires. The biospecific recognition of the aptamer fiber controls the position of nanowires. Due to its DNA nature, more subsequent assembly on the aptamer fiber template could be designed and exploited in the future.

## **8.2. Large-scale fabrication of protein nanoarrays based on nanosphere lithography**

Although there are lots of surface patterning techniques such as microcontact printing ( $\mu$ CP), Dip-pen lithography, nanografting, and AFM local oxidation lithography, they either lack the nanoscale resolution or surface coverage in the patterning of protein arrays on surfaces. To satisfy both the nanometer precision and high throughput, Cai demonstrated a simple nanosphere based lithography method to direct the assembly of proteins into arrays of around 100nm islands over macroscopic surface area.<sup>182</sup> In this method, the self-assembly of a nanosphere monolayer on a solid surface provides a simple and effective mask to prevent the deposition and modification directly beneath the nanospheres. Therefore, in the subsequent surface processing, only the interstitial area between nanospheres is exposed, and thus a hexagonally patterned surface will be formed as nanospheres are later removed. Scheme 8.1 shows the way nano-patterns are fabricated and subsequent protein immobilization. In this study, he utilized both nanosphere lithography and silane chemistry to chemically pattern surfaces with a regular array of sub-100nm islands over cm sample regions. These chemically patterned regions are used as a template to selectively adsorb lysozyme on carboxylic acid-terminated islands and not on the interstitial regions between the islands. In this manner, positive-toned protein nanoarrays are fabricated on the surface.<sup>182</sup> Their bioactivity was

evidenced by their high bio-specific affinity toward the antibody. Based on this method, we also developed a kind of negative-toned nanoarrays by selectively adsorbing protein molecules on the interstitial area instead of underneath the nanospheres on carboxylic acid terminated (UTSox) silane monolayer of silicon surface.

The similar negative-toned nanoarrays have been reported by Liu and Kingshott groups,<sup>255,256</sup> respectively. In Dr. Liu's experiment, the ordered assemblies were formed by the drying of protein and latex mixture on mica and gold surfaces, and then the latex is rinsed away to leave a periodic arrays of protein nanostructures on the substrate. For this protocol to succeed, the protein needs to exhibit specifically strong adhesion to the substrate but weak adhesion to latex. Furthermore, latex needs to adhere weakly to the substrate as well in order to be selectively removed easily in the following process.<sup>256</sup> Therefore, all these requirements limit it to be a generic patterning method for different proteins. Recently, binary colloidal crystal lithography combined with plasma polymerization has been reported by Dr. Kingshott's group. Here, he used binary colloidal crystals consisting of small and large particles as masks for the deposition of an amino-functionalized ultrathin film by plasma polymerization. Then, the amino groups were covalently grafted poly (ethylene glycol) propionaldehyde (PEG-PALD) to generate a patterned surface for the direct adsorption of protein. However, extra steps of plasma polymerization and covalent grafting were needed to form the negative-tone nanoarrays,<sup>255</sup> which is not very convenient. Compared with their methods, the patterning technique used in our lab has less steps and easier procedure. It also has the potential to provide us an effective means to immobilize more than one protein on the same surface. Our experiment process is shown in Scheme 8.2.

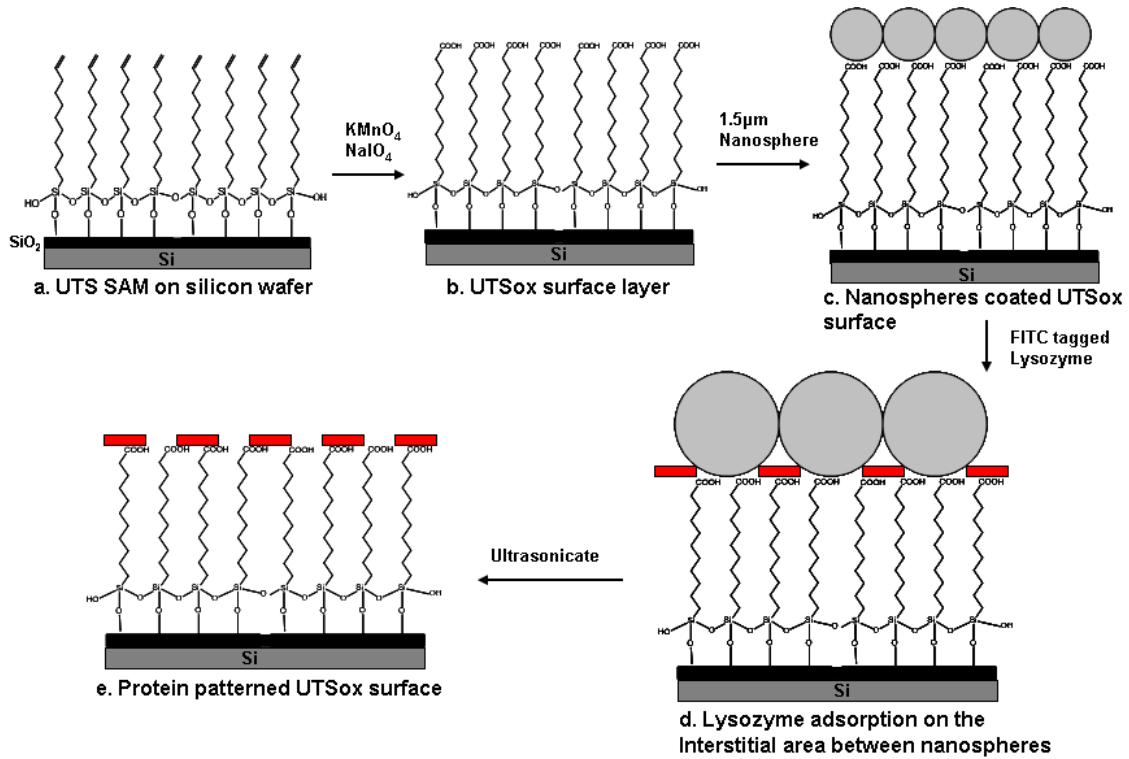


Scheme 8-1. Procedure for preparation of large-scale positive-toned protein patterns through Nanosphere Lithography a) Preparation of the nanosphere monolayer mask on the Si(100) surface. b) Vapor deposition the octadecyltrichlorosilane (OTS) silane, and it will grow in the area between the spheres. c) Removal of the nanosphere mask to expose the hexagonally arranged Si surface. d) Double bond-terminated undecenyltrichlorosilane (UTS) will grow another layer on the exposed Si surface. e) Surface oxidation converts the double bond-terminus to carboxylic (UTS<sub>ox</sub>) with negative charged. f) Incubation of the template in lysozyme solution leads to the immobilized lysozyme pattern.



As shown in Scheme 2, firstly, a flat and homogenous monolayer film of undecyltrichlorosilane (UTS) was grown on a  $1 \times 1 \text{ cm}^2$  Si(100) surface by the dipping method I discussed in chapter 2. Next, the UTS-coated silicon wafer was incubated in the oxidizing solution (0.01M  $\text{NaIO}_4$ ,  $5 \times 10^{-4}$  M  $\text{KMnO}_4$ , in 0.05M  $\text{Na}_2\text{CO}_3$  buffer) for 10h at  $40^\circ\text{C}$ . The sample was then rinsed with deionized water and followed by 1% Hydrazine for 1 min. Finally, the sample was dried in a stream of nitrogen. After this oxidation process, the double bonds on UTS molecules were converted into carboxylic acid groups. Around  $1.5 \mu\text{L}$  240nm nanosphere solution was then evenly spread on UTSox surface and dried slowly in the air. After that, the dried nanosphere-coated wafer was incubated in  $5 \mu\text{M}$  fluorescein isothiocyanate (FITC) tagged lysozyme solution for 12 hours. After being rinsed with deionied water, the fluorescence image was taken by the the Nikon fluorescence microscope N55i in our lab. The images for the same area taken under the white light (left) and the fluorescence (right) are shown in Figure 8.1. From the left image, we can see nanospheres are orderly arranged on the surface with bright color indicating nanospheres and dark color indicating the interstitial area between nanospheres. However, in the right fluorescence image, the color situation is totally opposite. The places nanospheres occupied are pretty dark and the interstitial areas are very bright. This can be clearly identified from insets which show the zoomed area in the red square on each image side by side. Since the control experiment showed that the fluorescence signal from the un-labeled protein was insignificant under for the exposure time we used, it can be concluded that the fluorescence signal generated in the fluorescence image is from the FITC-tagged protein molecules accumulated in the interstitial areas between the nanospheres. Finally, the nanospheres coated on the UTSox surface were removed by ultrasonication. The negative and carboxylic acid group-terminated patterns with tightly packed lysozyme protein molecules as background can be obtained on silicon surface. Figure 8.2a shows the AFM topography image of the negative-toned UTSox patterns fabricated by the Scheme 8.2. Figure 8.2b is the topography zoom-in view of the red box in Figure

8.2a.



Scheme 8-2. Procedure for preparation of large-scale negative-toned protein patterns through Nanosphere Lithography a) Grew UTS layer on Si(100) surface. b) Surface oxidation converted the double bond-termini on UTS to carboxylic (UTS<sub>ox</sub>) with negative charged. c) Preparation of the nanosphere monolayer mask on UTS<sub>ox</sub> layer of silicon surface. d) In 5µM FITC-tagged lysozyme solution, lysozyme molecules grew in the area between the spheres. e) Removal of the nanosphere mask to expose negative UTS<sub>ox</sub> patterns with lysozyme molecules packed around as the background.

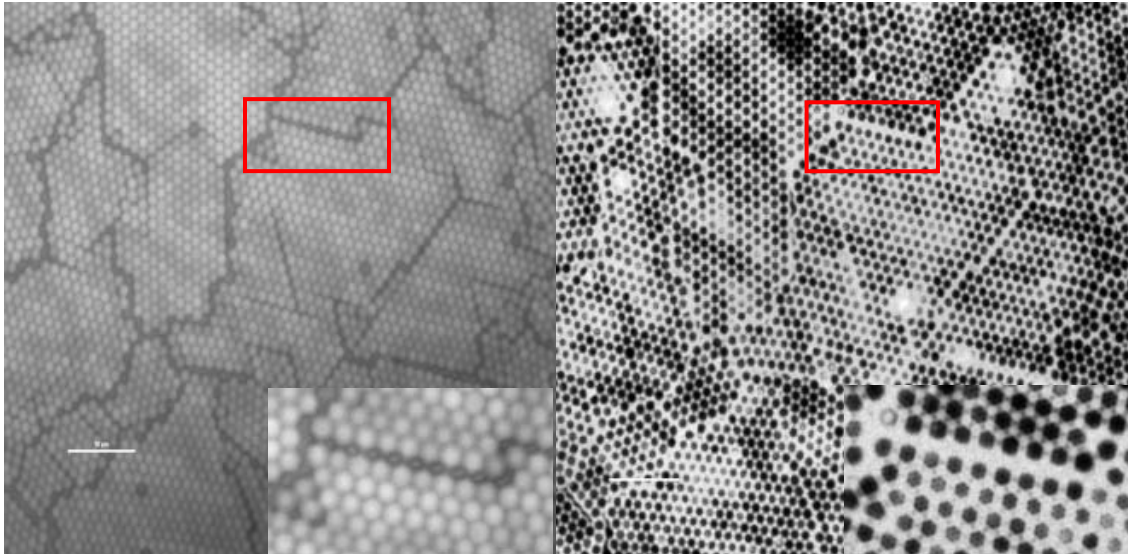


Figure 8-1. The Scheme 8.2d sample images taken separately under the white light (left) and fluorescence (right) by the Nikon fluorescence microscope N55i. The inset images are the same area in the red square from the two images, respectively

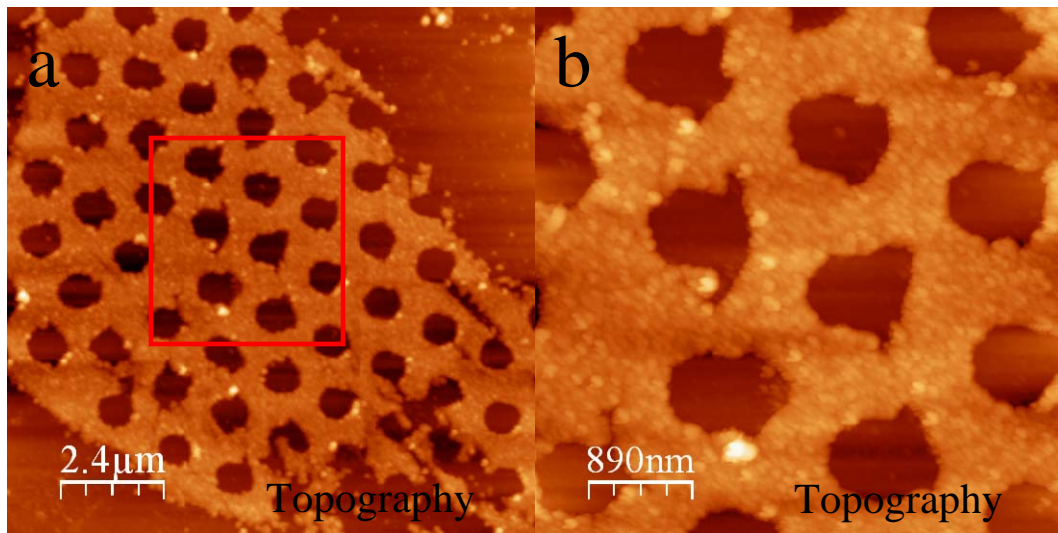


Figure 8-2. The negative-toned protein patterns through Scheme 8.2: (a) AFM topography image of negative UTSox patterns with lysozyme molecules packed tightly on the background. (b) High-resolution AFM topography image of the negative-toned patterns in the red box in (a).

It has been demonstrated that nanosphere lithography has some incomparable advantages, which include simplicity, mild environments, and high throughput. Based on the two fabrication Scheme, work is in progress to investigate if this method can be developed into a more generic patterning method for other proteins such as catalase, calmodulin (CaM) in our lab. It was reported that the size of the pattern was determined by the size of nanospheres and the molecular length of silane in scheme one. Therefore, by using smaller sized nanospheres as the mask, the size of protein patterns obtained on surfaces could be further reduced. Compared with Scheme 8.1, we find that Scheme 8.2 has fewer steps in the preparation of nanopatterns on surface, and it has potential to be an effective way to fabricate two kinds of protein molecules on one sample surface. The growth mechanism of protein molecules in scheme two will be further investigated through varying the size of nanospheres. Meanwhile, the reproducibility for the two methods needs to be improved in our lab.

### **8.3. The investigation of surface properties of OTSpd patterns**

OTSpd pattern can be fabricated by AFM local oxidation lithography. AFM images show the OTSpd pattern is 10.2Å lower than the OTS film, from which we could infer that OTS molecules are partially degraded and stay on the surface after the oxidation process. Also, the conversion of terminal methyl groups on OTS molecules to carboxylic acid groups was demonstrated by FTIR and fluorescence microscope. The detail information can be found in chapter 3. As we have already known, there are two opposite processes happened simultaneously in this oxidation, the partial degradation of OTS film, which decreases the pattern height, and the growth of silicon oxide, which increases the pattern height. We speculate that these two opposite processes reached equilibrium when the height of OTSpd was 10 Å lower than the OTS film. Therefore, the 10 Å depth measured from AFM is actually the summation of the two processes rather than exact eight CH<sub>2</sub> units were truncated from the degradation. In addition, the depth of OTSpd was measured by AFM with the tip contact area around 10×10 nm<sup>2</sup> or larger. During the AFM measurement, surface

features that are smaller than the tip size are subject to the tip convolution. OTS molecules that were truncated more than eight CH<sub>2</sub> units might also coexist with the OTS molecules are exactly 10Å lower than OTS background. When tall and short molecules mixed, AFM can only detect the tall molecules because of the tip size. As the primary substrate we worked on, OTSpd patterns play an important role on protein immobilization and alkane spreading which is another ongoing project in our lab. Therefore, the understanding of OTSpd patterns can lead to a better interpretation of the behavior of protein and alkane molecules. Since the AFM data only provide limited knowledge to OTSpd surface, other techniques and experiments such as Kelvin probe force microscopy (KPFM), fluorescence microscopy, and friction measurement on OTSpd surface have been used to investigate this AFM based oxidation process. The following sections are some results we got recently.

It has been demonstrated that UTSox pattern can be fabricated on OTS layer of silicon surface. AFM image in Figure 8.3 shows that UTSox pattern is around 1.6nm higher than the OTS background. To compare with the carboxylic acid-terminated patterns created by wet chemical reactions, OTSpd patterns are fabricated together with UTSox patterns in 50×50µm<sup>2</sup> of OTS surface area. The detailed fabrication procedure can be found in chapter three. As I have discussed in chapter six, KPFM detects the contact potential difference (CPD) between a conducting AFM probe and the surface. The surface potential image in Figure 8.4a shows the OTSpd patterns are much brighter than UTSox pattern. According to the potential cross sectional profile in Figure 8.4b, we can conclude that the CPD value of OTSpd is roughly 76.76mv higher than that of UTSox. It means that OTSpd surface has a higher charge density than that on UTSox pattern surface.

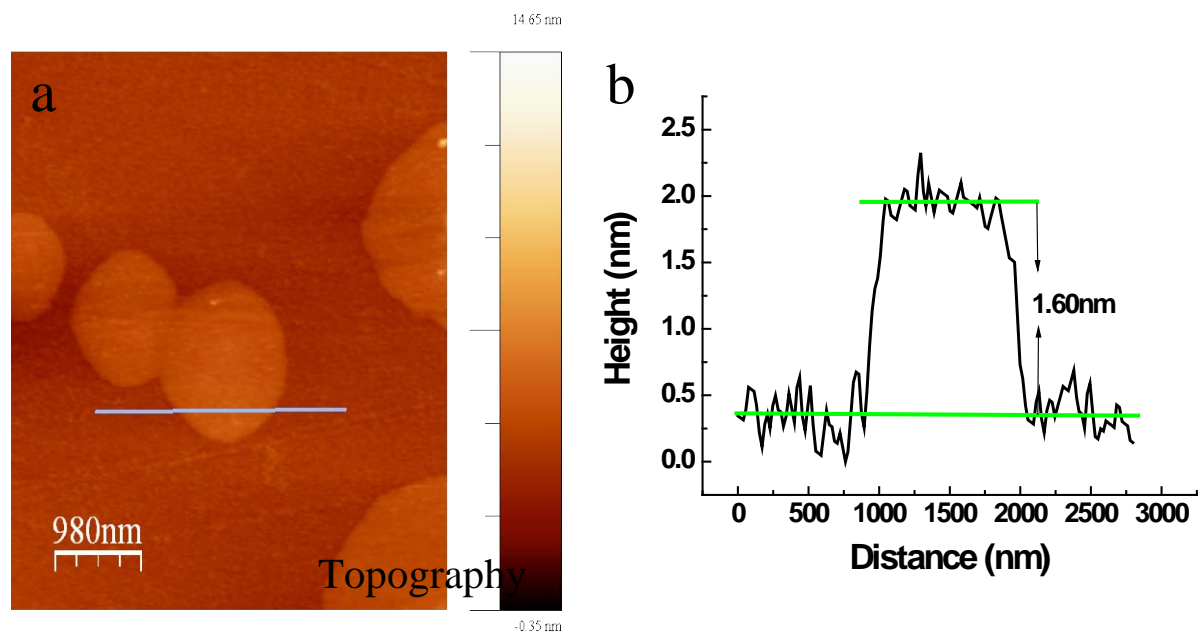


Figure 8-3. (a) The topography image of UTSoxOTSpd patterns on OTS self-assembled monolayer of silicon surface; (b) The height cross-sectional profiles corresponding to the blue line in (a).

In another experiment, we also compared the carboxylic acid group coverage on OTSpd and UTSox patterns through the fluorescence signal quantitatively generated from the bound PDAM. When the fluorescence image and surface potential image were put together, we got inconsistent experiment result. In the fluorescence microscope image of Figure 8.5a, we can clearly identify that the fluorescence signal on UTSox pattern has higher intensity than that on OTSpd pattern, and the cross sectional profile in Figure 8.5b shows the difference is about 30.60. Fluorescent image suggests that the carboxylic acid group density on UTSox pattern surface is higher than that on OTSpd pattern surface. However, the CPD values measured by KPFM are supposed to get the opposite results. Based on the inconsistent results, we speculate that there probably exist some PDAM non-bound carboxylic acid groups on the OTSpd pattern during the incubation in 3mM PDAM methanol solution. Therefore, the OTSpd pattern surface shows the weaker fluorescence signal than UTSox pattern surface, while shows the higher charge density than UTSox pattern in surface potential image.

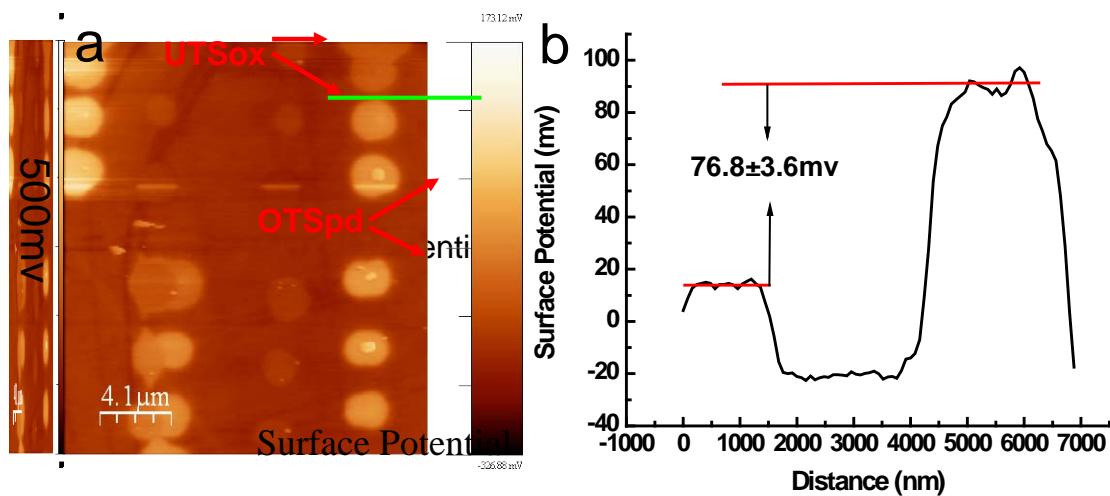


Figure 8-4. (a) The surface potential image of OTSpd and UTSox patterns on OTS surface. (b) The surface potential cross-sectional profile along the green line in (a) shows the surface potential of OTSpd patterns is roughly  $76.76 \pm 3.59$  mV higher than that of UTSox patterns.

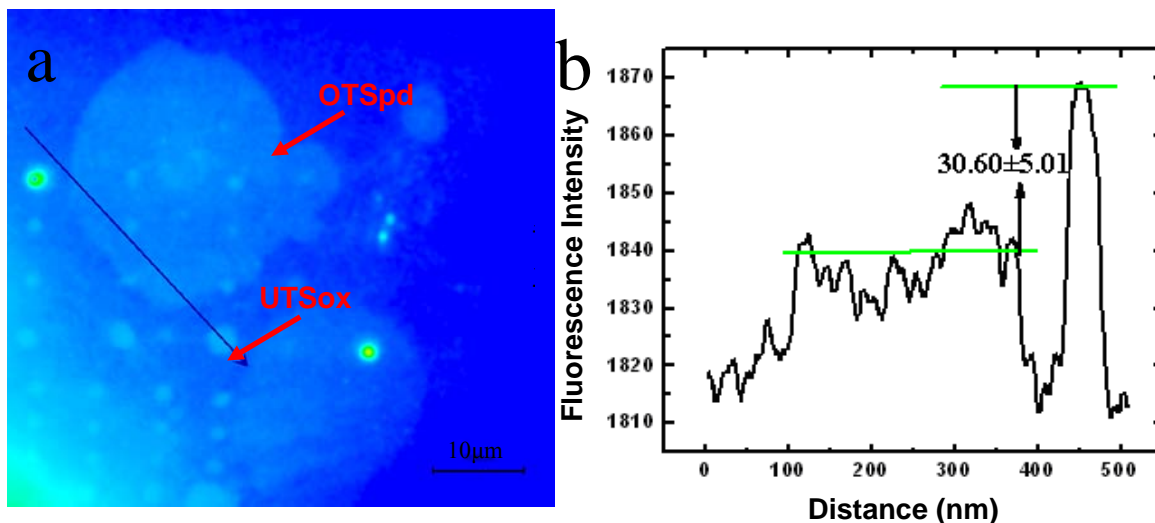


Figure 8-5. (a) The fluorescence microscope image of OTSpd (big patterns) and UTSox (small pattern) patterns on OTS surface. (b) The height cross-sectional profile along the blue line in (a) shows the fluorescence intensity on UTSox pattern is  $30.60 \pm 5.01$  higher than that on OTSpd pattern.

This could be understood by a possible heterogeneous degradation reaction happened during the AFM local oxidation lithography and thus generated different length of degraded OTS molecules covered on the OTSpd pattern. So, the relatively big PDAM molecules can not reach the carboxylic acid groups on the shorter length of degraded OTS molecules in the incubation because of the spatial hindrance around them as the cartoon shown in Figure 8.6. As the result, the fluorescence signal on the OTSpd pattern surface is not consistent with its surface potential result. In comparison, the chemical oxidation process generates a homogeneous surface on UTSox pattern surface with a unique height of molecules on the top. PDAM molecules can react with the carboxylic acid group on the surface without any spatial resistance and thus generate higher fluorescence signal intensity than OTSpd pattern. This hypothesis needs to be further identified by other methods in the future.

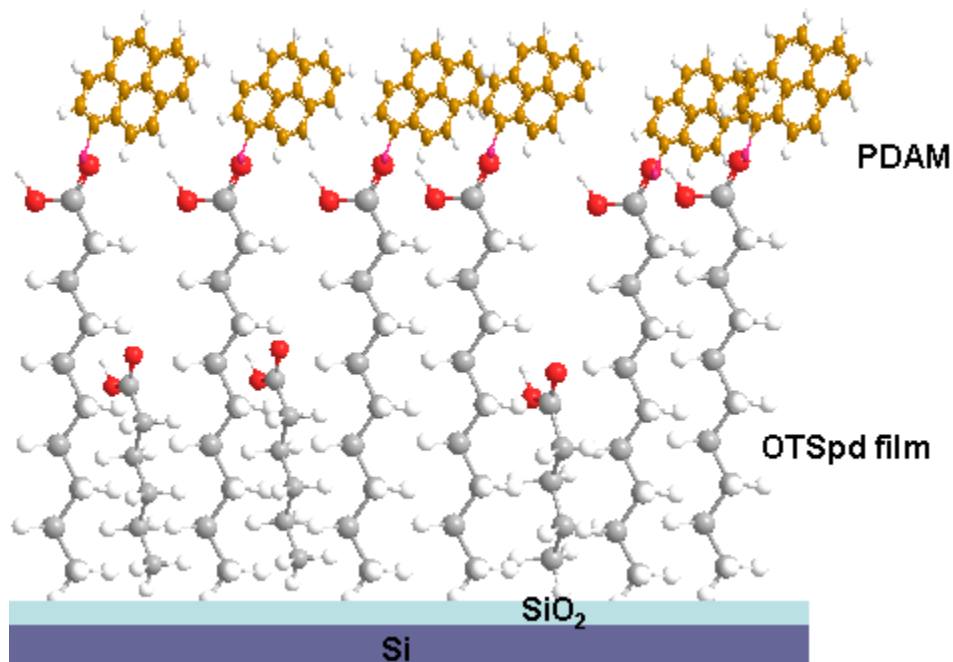


Figure 8-6. The spatial hindrance of the higher molecules around blocks the PDAM binding on the short length OTSpd molecules on silicon surface. The red label on each top of molecules indicates carboxylic acid group.



Besides that, we also measured and compared the frictions on the OTSpd, UTSox and OTS surface to get more surface-associated information. In the friction measurement, the three different surface domains OTS, OTSpd and UTSox were created side-by-side on the same area of surface. The contact mode scanning under various loading forces using the same MikroMasch CSC-17 tip was employed. As shown in Figure 8.7a, different zones between two green lines were scanned under different loading forces. In each scanned zone, OTS, OTSpd and UTSox chemical islands are aligned along the scanning direction, thus the friction associated with the three different surfaces can be obtained simultaneously under the same loading force and the same instrumental set-up. The image in Figure 8.7b is the friction image corresponding to the topography image in Figure 8.7a. The friction cross-sectional profile in each force zone corresponding to the green lines in Figure 8.7a was created. Based on the each friction cross-sectional profile, the frictions of OTS, OTSpd and UTSox under different loading forces were plotted in Figure 8.8. In these measurements, the friction forces increased linearly with the applied load. In addition, the plot indicates that the frictions of the UTSox surface are higher than the OTSpd under the same loading force, even though both surfaces are carboxylic acid-terminated. The linear fitting of the friction versus loading force plot shows that the coefficient of friction (COF) of the OTSpd is equal to UTSox.

Generally, the chemical properties on surfaces dominate the observed friction difference in structurally well defined system. However, it has been demonstrated that other mechanical properties of the SAMs such as elasticity, crystallinity and chain-length can also affect the frictional behavior of the organic layer.<sup>71,257,258</sup> The result of friction measurements further proves the previous conclusion that OTSpd and UTSox surfaces are structurally different. The large magnitude of the friction force on UTSox patterns probably originates mainly from the larger contact area between AFM tip with carboxylic groups on UTSox surface than OTSpd surface under the same loading force. This is also because of the roughness of OTSpd surface.

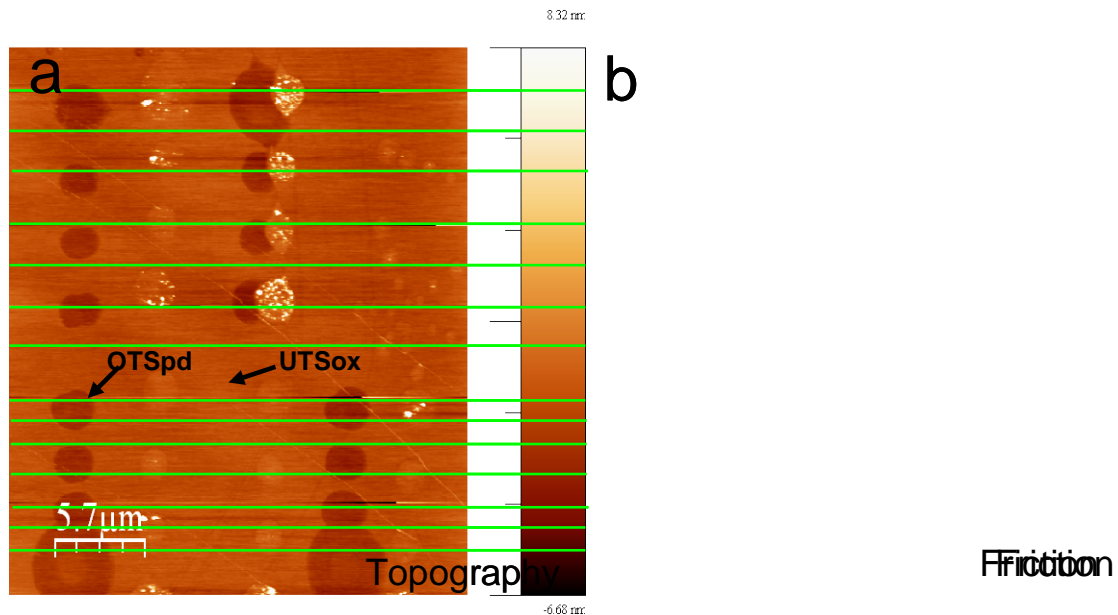


Figure 8-7. The topography (a) and friction images (b) obtained during the contact mode scanning with different loading forces

In this experiment, the plot we are able to directly obtain from the friction image is the AFM force set point versus friction, and both the X and Y axis have the unit of voltage. In order to convert the voltage information obtained from the friction cross sectional-profile to force unit (newton), the normal spring constant of a cantilever ( $K_z$ ) and its torsional spring constant ( $K_\psi$ ) need to be calculated. Firstly, the tip's frequency response curve was measured to get the tip's resonant frequency. Then, the quality factor  $Q_f$  of the fundamental flexural resonance peak for the cantilever beam in air can be calculated according to equation (1), where  $\omega_f$  is the AFM tip's resonant frequency and  $\Delta f$  is the width of half the maximum of the energy frequency curve. Since what we measured is amplitude frequency response curve, and the energy is directly proportional to the square of the oscillation amplitude,  $\Delta f$  here is actually the width of  $1/\sqrt{2}$  of the maximum of the amplitude frequency curve. Besides that, the physical dimensions of the cantilever and the tip pyramid were measured using a Nikon Eclipse 55i microscope. With the measured data, the spring constant of the cantilever ( $K_z$ ) was calculated according to Sader's method.<sup>259,260</sup> The torsion

spring constant of the cantilever ( $K_\psi$ ) was calculated according to the formula (2).<sup>260</sup>

$$Q_f = \frac{\omega_f}{\Delta f} \quad (1)$$

$$K_\psi = \frac{2L^2}{3(1+\nu)} K_z \quad (2)$$

Here, L is the length of the cantilever, and  $\nu$  is the Poisson ration of the cantilever. For the MikroMasch CSC 17 tip used here, the cantilever is made of silicon (100), and  $\nu$  equals 0.28.<sup>261</sup> However,  $K_z$  obtained from Sader's method has the unit of N/m, which still can not convert the voltage to Newton directly. So, a force-distance curve of AFM tip was measured to calculate the ratio of piezo displacement (nm) to cantilever deflection (V). By timing the ratio with  $K_z$ , its unit is changed into nN/V which can convert the voltage to Newton. Upon the same method, the unit of  $K_\psi$  was converted to nN/V as well. Finally, by multiplying the each datum on X axis with  $K_z$  (nN/V), the loading force on sample surface with unit of Newton can be obtained. Similarly, by multiplying the each datum on Y axis with  $K_\psi$  (nN/V), the friction with unit of Newton according to the different loading force is obtainable as well.

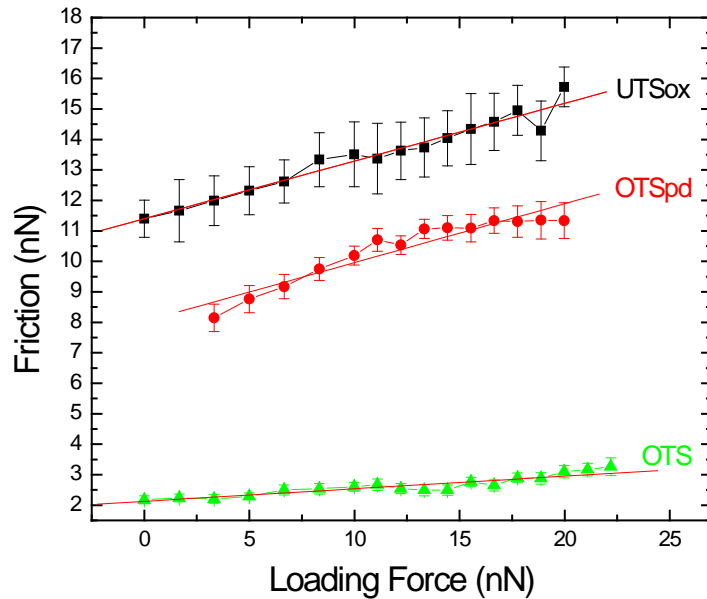


Figure 8-8. The friction force as a function of AFM tip loading force on surfaces. The green line is the friction response of the OTS film. The red line is the friction response of OTSpd pattern surface. The black line is the friction response of UTSox pattern surface.

As I mentioned before, we also measured the AFM force-distance curve. Based on the curve, another important parameter of adhesion force has been measured and studied. From the force-distance curve in Figure 8.9, we can see that the probe is far away from the surface at the beginning, so there is no interaction between the tip and the sample. As the probe-sample separation is reduced beyond a certain point, the attractive forces between atoms on the probe and sample begin to act, causing the flexible cantilever to bend toward the sample. If the force acting on the tip is greater than the spring constant of the cantilever at a sufficiently small probe-sample spacing, the instability causes a jump of the probe to contact. Once in contact with the surface, the probe will experience an ever-increasing repulsive force, which causes the cantilever to bend away from the surface. It is referred as the contact region as shown in the force curve. Upon withdrawing the probe, the bending of the cantilever is again

towards the sample surface. To further separate the probe and surface, we need to overcome the adhesion force between them which are created during their contact. Similarly, as the bending of the cantilever reaches a certain point, the tip-surface contact is broken. From this moment, the probe will not experience any adhesion from the sample.

The adhesion force can be estimated from the deflection of cantilever right before the jump-off contact point. By using Hooke's law, one can obtain the adhesion force between the tip and the sample

$$F = k_{tip} \times \Delta z \quad (3)$$

Where  $k_{tip}$  represents the spring constant of the cantilever and  $\Delta z$  represents the jump-off displacement during retraction of the tip from the surface. In addition, there is always a thin water film covers both the probe and the sample as the AFM is operated in air. This thin film creates capillary forces that may have a dramatic effect on the force curves. To eliminate this interference, our experiment was performed in 2-butanol instead of air.

Besides that, in order to carry out a quantitative analysis for the adhesion force, fifty experimental measurements on OTS, OTSpd and UTSox chemical islands were conducted in the same environment, respectively. Histograms of the adhesive force versus the number of times this force is observed typically to exhibit Gaussian distributions. Therefore, the mean adhesion forces ( $\pm$ experimental uncertainty) associated with the three different chemical surfaces were yielded and the results were summarized in Table 8.1. This result is generally consistent with the friction measurement before, and more detailed study is ongoing in our lab.

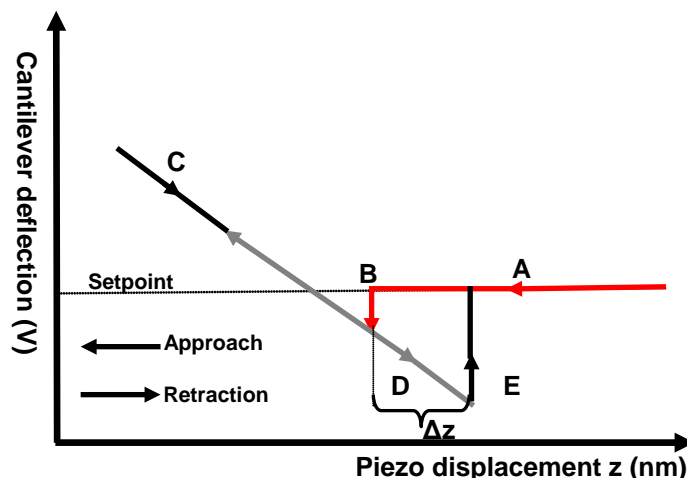


Figure 8-9. Schematic representation of a force-distance curve. The labels are corresponding to the tip-sample interaction points. A: Approach; B: Jump to contact; C: Contact; D: Adhesion; E: Pull-off.

Table 8-1. The statistical analysis result of adhesion forces obtained from the fifty points measured on OTS, OTSpd and UTSox surface.

	OTS	OTSpd	UTSox
<b>Adhesion Force (nN)</b>	<b>2.206±0.004</b>	<b>9.0±0.1</b>	<b>9.7±0.2</b>

In view of this, more experiment data will be collected to prove the reproducibility and consistency of all the measurements associated with the three difference chemical domains in the future. We also expect to get more interesting information regarding to the OTSpd surface properties from other methods to understand the AFM local oxidation lithography technique.

## Reference

- (1) Ngunjiri, J.; Garno, J. C. AFM-based lithography for nanoscale protein assays. *Analytical Chemistry* **2008**, *80*, 1361.
- (2) Rosi, N. L.; Mirkin, C. A. Nanostructures in biodiagnostics. *Chemical Reviews* **2005**, *105*, 1547.
- (3) Christman, K. L.; Enriquez-Rios, V. D.; Maynard, H. D. Nanopatterning proteins and peptides. *Soft Matter* **2006**, *2*, 928.
- (4) Wink, T.; vanZuilen, S. J.; Bult, A.; vanBennekom, W. P. Self-assembled monolayers for biosensors. *Analyst* **1997**, *122*, R43.
- (5) Gopel, W.; Heiduschka, P. Interface analysis in biosensor design. *Biosensors & Bioelectronics* **1995**, *10*, 853.
- (6) Cornell, B. A.; BraachMaksvytis, V. L. B.; King, L. G.; Osman, P. D. J.; Raguse, B.; Wiczorek, L.; Pace, R. J. A biosensor that uses ion-channel switches. *Nature* **1997**, *387*, 580.
- (7) Galla, H. J. Field-effect transistors as sensors of neural systems. *Angewandte Chemie-International Edition* **1992**, *31*, 45.
- (8) Rodriguez-Mozaz, S.; Marco, M. P.; de Alda, M. J. L.; Barcelo, D. Biosensors for environmental monitoring of endocrine disruptors: a review article. *Analytical and Bioanalytical Chemistry* **2004**, *378*, 588.
- (9) Makarenko, A. A.; Bezverbnaya, I. P.; Kosheleva, I. A.; Kuvichkina, T. N.; Il'yasov, P. V.; Reshetilov, A. N. Development of biosensors for phenol determination from bacteria found in petroleum fields of West Siberia. *Applied Biochemistry and Microbiology* **2002**, *38*, 23.
- (10) Brynda, E.; Houska, M.; Skvor, J.; Ramsden, J. J. Immobilization of multilayer bioreceptor assemblies on solid substrates. *Biosensors & Bioelectronics* **1998**, *13*, 165.
- (11) Prime, K. L.; Whitesides, G. M. Adsorption of proteins onto surfaces containing end-attached oligo(ethylene oxide) - a model system using self-assembled monolayers. *Journal of the American Chemical Society* **1993**, *115*, 10714.
- (12) Medintz, I. L.; Clapp, A. R.; Mattoussi, H.; Goldman, E. R.; Fisher, B.; Mauro, J. M. Self-assembled nanoscale biosensors based on quantum dot FRET donors. *Nature Materials* **2003**, *2*, 630.
- (13) Prime, K. L.; Whitesides, G. M. Self-assembled organic monolayers - model systems for studying adsorption of proteins at surfaces. *Science* **1991**, *252*, 1164.
- (14) Cullum, B. M.; Vo-Dinh, T. The development of optical nanosensors for biological measurements. *Trends in Biotechnology* **2000**, *18*, 388.
- (15) Mandal, H. S.; Kraatz, H. B. Effect of the surface curvature on the secondary structure of peptides adsorbed on nanoparticles. *Journal of the American Chemical Society* **2007**, *129*, 6356.
- (16) Patel, N.; Davies, M. C.; Hartshorne, M.; Heaton, R. J.; Roberts, C. J.; Tendler, S. J. B.; Williams, P. M. Immobilization of protein molecules onto homogeneous and mixed carboxylate-terminated self-assembled monolayers. *Langmuir* **1997**, *13*, 6485.
- (17) Wadu-Mesthrige, K.; Amro, N. A.; Liu, G. Y. Immobilization of proteins on self-assembled monolayers. *Scanning* **2000**, *22*, 380.

- (18) Gates, B. D.; Xu, Q. B.; Love, J. C.; Wolfe, D. B.; Whitesides, G. M. Unconventional nanofabrication. *Annual Review of Materials Research* **2004**, *34*, 339.
- (19) Ito, T.; Okazaki, S. Pushing the limits of lithography. *Nature* **2000**, *406*, 1027.
- (20) Chou, S. Y.; Krauss, P. R.; Renstrom, P. J. Nanoimprint lithography. *Journal of Vacuum Science & Technology B* **1996**, *14*, 4129.
- (21) Chou, S. Y.; Krauss, P. R. Imprint lithography with sub-10 nm feature size and high throughput. *Microelectronic Engineering* **1997**, *35*, 237.
- (22) Xia, Y. N.; Whitesides, G. M. Soft lithography. *Annual Review of Materials Science* **1998**, *28*, 153.
- (23) Chen, Y.; Pepin, A. Nanofabrication: Conventional and nonconventional methods. *Electrophoresis* **2001**, *22*, 187.
- (24) Whitesides, G. M.; Mathias, J. P.; Seto, C. T. Molecular self-assembly and nanochemistry - a chemical strategy for the synthesis of nanostructures. *Science* **1991**, *254*, 1312.
- (25) Binnig, G.; Quate, C. F.; Gerber, C. Atomic force microscope. *Physical Review Letters* **1986**, *56*, 930.
- (26) Binnig, G.; Rohrer, H.; Gerber, C.; Weibel, E. Surface studies by scanning tunneling microscopy. *Physical Review Letters* **1982**, *49*, 57.
- (27) Okazaki, S. Resolution limits of optical lithography. *Journal of Vacuum Science & Technology B* **1991**, *9*, 2829.
- (28) Itani, T.; Wakamiya, W.; Cashmore, J.; Gower, M. 157-nm lithography with high numerical aperture lens for sub-70 nm node. *Microelectronic Engineering* **2003**, *67-8*, 39.
- (29) Pease, R. F. W. Nanolithography and its prospects as a manufacturing technology. *Journal of Vacuum Science & Technology B* **1992**, *10*, 278.
- (30) Rothschild, M.; Ehrlich, D. J. Attainment of 0.13- $\mu\text{m}$  lines and spaces by excimer-laser projection lithography in diamond-like carbon-resist. *Journal of Vacuum Science & Technology B* **1987**, *5*, 389.
- (31) Hibbs, M.; Kunz, R.; Rothschild, M. 193-nm lithography at mit lincoln lab. *Solid State Technology* **1995**, *38*, 69.
- (32) Levenson, M. D. Extending optical lithography to the gigabit era. *Solid State Technology* **1995**, *38*, 57.
- (33) White, D. L.; Bjorkholm, J. E.; Bokor, J.; Eichner, L.; Freeman, R. R.; Jewell, T. E.; Mansfield, W. M.; Macdowell, A. A.; Szeto, L. H.; Taylor, D. W.; Tennant, D. M.; Waskiewicz, W. K.; Windt, D. L.; Wood, O. R. Soft-x-ray projection lithography. *Solid State Technology* **1991**, *34*, 37.
- (34) Broers, A. N.; Molzen, W. W.; Cuomo, J. J.; Wittels, N. D. Electron-beam fabrication of 80- $\text{\AA}$  metal structures. *Applied Physics Letters* **1976**, *29*, 596.
- (35) Wilbur, J. L.; Kumar, A.; Biebuyck, H. A.; Kim, E.; Whitesides, G. M. Microcontact printing of self-assembled monolayers: Applications in microfabrication. *Nanotechnology* **1996**, *7*, 452.
- (36) Love, J. C.; Wolfe, D. B.; Haasch, R.; Chabinyc, M. L.; Paul, K. E.; Whitesides, G. M.; Nuzzo, R. G. Formation and structure of self-assembled monolayers of alkanethiolates on palladium. *Journal of the American Chemical Society* **2003**, *125*, 2597.



- (37) Carvalho, A.; Geissler, M.; Schmid, H.; Michel, B.; Delamarche, E. Self-assembled monolayers of eicosanethiol on palladium and their use in microcontact printing. *Langmuir* **2002**, *18*, 2406.
- (38) Noble-Luginbuhl, A. R.; Nuzzo, R. G. Assembly and characterization of SAMs formed by the adsorption of alkanethiols on zinc selenide substrates. *Langmuir* **2001**, *17*, 3937.
- (39) Biebuyck, H. A.; Larsen, N. B.; Delamarche, E.; Michel, B. Lithography beyond light: Microcontact printing with monolayer resists. *Ibm Journal of Research and Development* **1997**, *41*, 159.
- (40) Odom, T. W.; Love, J. C.; Wolfe, D. B.; Paul, K. E.; Whitesides, G. M. Improved pattern transfer in soft lithography using composite stamps. *Langmuir* **2002**, *18*, 5314.
- (41) Schmid, H.; Michel, B. Siloxane polymers for high-resolution, high-accuracy soft lithography. *Macromolecules* **2000**, *33*, 3042.
- (42) Bao, L. R.; Cheng, X.; Huang, X. D.; Guo, L. J.; Pang, S. W.; Yee, A. F. Nanoimprinting over topography and multilayer three-dimensional printing. *Journal of Vacuum Science & Technology B* **2002**, *20*, 2881.
- (43) Xia, Y. N.; McClelland, J. J.; Gupta, R.; Qin, D.; Zhao, X. M.; Sohn, L. L.; Celotta, R. J.; Whitesides, G. M. Replica molding using polymeric materials: A practical step toward nanomanufacturing. *Advanced Materials* **1997**, *9*, 147.
- (44) Zhao, X. M.; Xia, Y. N.; Whitesides, G. M. Fabrication of three-dimensional micro-structures: Microtransfer molding. *Advanced Materials* **1996**, *8*, 837.
- (45) Frommer, J. Scanning Tunneling Microscopy and Atomic Force Microscopy in Organic-Chemistry. *Angewandte Chemie-International Edition* **1992**, *31*, 1298.
- (46) Mcdermott, C. A.; Mcdermott, M. T.; Green, J. B.; Porter, M. D. Structural origins of the surface depressions at alkanethiolate monolayers on Au(111) - a scanning tunneling and atomic-force microscopic investigation. *Journal of Physical Chemistry* **1995**, *99*, 13257.
- (47) Schonenberger, C.; Sondaghuethorst, J. A. M.; Jorritsma, J.; Fokkink, L. G. J. What are the holes in self-assembled monolayers of alkanethiols on gold. *Langmuir* **1994**, *10*, 611.
- (48) Ohnesorge, F.; Binnig, G. True atomic-resolution by atomic force microscopy through repulsive and attractive forces. *Science* **1993**, *260*, 1451.
- (49) Zasadzinski, J. A.; Viswanathan, R.; Madsen, L.; Garnaes, J.; Schwartz, D. K. Langmuir-blodgett-films. *Science* **1994**, *263*, 1726.
- (50) Noy, A.; Frisbie, C. D.; Rozsnyai, L. F.; Wrighton, M. S.; Lieber, C. M. Chemical force microscopy - exploiting chemically-modified tips to quantify adhesion, friction, and functional-group distributions in molecular assemblies. *Journal of the American Chemical Society* **1995**, *117*, 7943.
- (51) Wilbur, J. L.; Biebuyck, H. A.; Macdonald, J. C.; Whitesides, G. M. Scanning force microscopies can image patterned self-assembled monolayers. *Langmuir* **1995**, *11*, 825.
- (52) Frisbie, C. D.; Rozsnyai, L. F.; Noy, A.; Wrighton, M. S.; Lieber, C. M. Functional-group imaging by chemical force microscopy. *Science* **1994**, *265*, 2071.

- (53) Hoepfner, S.; Maoz, R.; Cohen, S. R.; Chi, L. F.; Fuchs, H.; Sagiv, J. Metal nanoparticles, nanowires, and contact electrodes self-assembled on patterned monolayer templates - A bottom-up chemical approach. *Advanced Materials* **2002**, *14*, 1036.
- (54) El Feninat, F.; Elouatik, S.; Ellis, T. H.; Sacher, E.; Stangel, I. Quantitative assessment of surface roughness as measured by AFM: application to polished human dentin. *Applied Surface Science* **2001**, *183*, 205.
- (55) Stahrenberg, K.; Herrmann, T.; Wilmers, K.; Esser, N.; Richter, W.; Lee, M. J. G. Optical properties of copper and silver in the energy range 2.5-9.0 eV. *Physical Review B* **2001**, *6411*.
- (56) Loh, K. P.; Xie, X. N.; Lim, Y. H.; Teo, E. J.; Zheng, J. C.; Ando, T. Surface oxygenation studies on (100)-oriented diamond using an atom beam source and local anodic oxidation. *Surface Science* **2002**, *505*, 93.
- (57) Nguyen, C. V.; Chao, K. J.; Stevens, R. M. D.; Delzeit, L.; Cassell, A.; Han, J.; Meyyappan, M. Carbon nanotube tip probes: stability and lateral resolution in scanning probe microscopy and application to surface science in semiconductors. *Nanotechnology* **2001**, *12*, 363.
- (58) Bradby, J. E.; Williams, J. S.; Wong-Leung, J.; Kucheyev, S. O.; Swain, M. V.; Munroe, P. Spherical indentation of compound semiconductors. *Philosophical Magazine a-Physics of Condensed Matter Structure Defects and Mechanical Properties* **2002**, *82*, 1931.
- (59) Hudspeth, Q. M.; Nagle, K. P.; Zhao, Y. P.; Karabacak, T.; Nguyen, C. V.; Meyyappan, M.; Wang, G. C.; Lu, T. M. How does a multiwalled carbon nanotube atomic force microscopy probe affect the determination of surface roughness statistics? *Surface Science* **2002**, *515*, 453.
- (60) Ji, Z. G.; Wong, K. W.; Tse, P. K.; Kwok, R. W. M.; Lau, W. M. Copper phthalocyanine film grown by vacuum deposition under magnetic field. *Thin Solid Films* **2002**, *402*, 79.
- (61) Amro, N. A.; Xu, S.; Liu, G. Y. Patterning surfaces using tip-directed displacement and self-assembly. *Langmuir* **2000**, *16*, 3006.
- (62) Xu, S.; Liu, G. Y. Nanometer-scale fabrication by simultaneous nanoshaving and molecular self-assembly. *Langmuir* **1997**, *13*, 127.
- (63) Xu, S.; Miller, S.; Laibinis, P. E.; Liu, G. Y. Fabrication of nanometer scale patterns within self-assembled monolayers by nanografting. *Langmuir* **1999**, *15*, 7244.
- (64) Ginger, D. S.; Zhang, H.; Mirkin, C. A. The evolution of dip-pen nanolithography. *Angewandte Chemie-International Edition* **2004**, *43*, 30.
- (65) Demers, L. M.; Ginger, D. S.; Park, S. J.; Li, Z.; Chung, S. W.; Mirkin, C. A. Direct patterning of modified oligonucleotides on metals and insulators by dip-pen nanolithography. *Science* **2002**, *296*, 1836.
- (66) Hong, S. H.; Zhu, J.; Mirkin, C. A. Multiple ink nanolithography: Toward a multiple-pen nano-plotter. *Science* **1999**, *286*, 523.
- (67) Piner, R. D.; Zhu, J.; Xu, F.; Hong, S. H.; Mirkin, C. A. "Dip-pen" nanolithography. *Science* **1999**, *283*, 661.
- (68) Maoz, R.; Frydman, E.; Cohen, S. R.; Sagiv, J. "Constructive nanolithography": Inert monolayers as patternable templates for in-situ nanofabrication of

metal-semiconductor-organic surface structures - A generic approach. *Advanced Materials* **2000**, *12*, 725.

(69) Cai, Y. G. Chemical template directed iodine patterns on the octadecyltrichlorosilane surface. *Langmuir* **2008**, *24*, 337.

(70) Radmacher, M.; Tilmann, R. W.; Gaub, H. E. Imaging viscoelasticity by force modulation with the atomic force microscope. *Biophysical Journal* **1993**, *64*, 735.

(71) Overney, R. M.; Meyer, E.; Frommer, J.; Guntherodt, H. J.; Fujihira, M.; Takano, H.; Gotoh, Y. Force microscopy study of friction and elastic compliance of phase-separated organic thin-films. *Langmuir* **1994**, *10*, 1281.

(72) Joyce, S. A.; Thomas, R. C.; Houston, J. E.; Michalske, T. A.; Crooks, R. M. Mechanical relaxation of organic monolayer films measured by force microscopy. *Physical Review Letters* **1992**, *68*, 2790.

(73) Carpick, R. W.; Ogletree, D. F.; Salmeron, M. Lateral stiffness: A new nanomechanical measurement for the determination of shear strengths with friction force microscopy. *Applied Physics Letters* **1997**, *70*, 1548.

(74) Overney, R. M.; Takano, H.; Fujihira, M.; Paulus, W.; Ringsdorf, H. Anisotropy in Friction and Molecular Stick-Slip Motion. *Physical Review Letters* **1994**, *72*, 3546.

(75) Czajkowsky, D. M.; Mou, J.; Shao, Z. Imaging bilayer heterogeneity with AFM in solution. *Biophysical Journal* **1996**, *70*, Su330.

(76) Radmacher, M.; Tillmann, R. W.; Fritz, M.; Gaub, H. E. From molecules to cells - imaging soft samples with the atomic force microscope. *Science* **1992**, *257*, 1900.

(77) Florin, E. L.; Rief, M.; Lehmann, H.; Ludwig, M.; Dornmair, C.; Moy, V. T.; Gaub, H. E. Sensing specific molecular-interactions with the atomic-force microscope. *Biosensors & Bioelectronics* **1995**, *10*, 895.

(78) Ludwig, M.; Dettmann, W.; Gaub, H. E. Atomic force microscope imaging contrast based on molecular recognition. *Biophysical Journal* **1997**, *72*, 445.

(79) Kolbe, W. F.; Ogletree, D. F.; Salmeron, M. B. Atomic force microscopy imaging of T4 bacteriophages on silicon substrates. *Ultramicroscopy* **1992**, *42*, 1113.

(80) Hansma, P. K.; Cleveland, J. P.; Radmacher, M.; Walters, D. A.; Hillner, P. E.; Bezanilla, M.; Fritz, M.; Vie, D.; Hansma, H. G.; Prater, C. B.; Massie, J.; Fukunaga, L.; Gurley, J.; Elings, V. Tapping mode atomic-force microscopy in liquids. *Applied Physics Letters* **1994**, *64*, 1738.

(81) San Paulo, A.; Garcia, R. High-resolution imaging of antibodies by tapping-mode atomic force microscopy: Attractive and repulsive tip-sample interaction regimes. *Biophysical Journal* **2000**, *78*, 1599.

(82) Thomas, R. C.; Tangyonyong, P.; Houston, J. E.; Michalske, T. A.; Crooks, R. M. Chemically-sensitive interfacial force microscopy - contact potential measurements of self-assembling monolayer films. *Journal of Physical Chemistry* **1994**, *98*, 4493.

(83) Marrian, C. R. K.; Snow, E. S. Proximal probe lithography and surface modification. *Microelectronic Engineering* **1996**, *32*, 173.

- (84) Bard, A. J.; Fan, F. R. F.; Pierce, D. T.; Unwin, P. R.; Wipf, D. O.; Zhou, F. M. Chemical Imaging of Surfaces with the Scanning Electrochemical Microscope. *Science* **1991**, *254*, 68.
- (85) Crooks, R. M.; Ricco, A. J. New organic materials suitable for use in chemical sensor arrays. *Accounts of Chemical Research* **1998**, *31*, 219.
- (86) Flink, S.; van Veggel, F. C. J. M.; Reinhoudt, D. N. Sensor functionalities in self-assembled monolayers. *Advanced Materials* **2000**, *12*, 1315.
- (87) Willner, I.; Katz, E. Integration of layered redox proteins and conductive supports for bioelectronic applications. *Angewandte Chemie-International Edition* **2000**, *39*, 1180.
- (88) Dubois, L. H.; Nuzzo, R. G. Synthesis, structure, and properties of model organic-surfaces. *Annual Review of Physical Chemistry* **1992**, *43*, 437.
- (89) Dimilla, P. A.; Folkers, J. P.; Biebuyck, H. A.; Harter, R.; Lopez, G. P.; Whitesides, G. M. Wetting and protein adsorption of self-assembled monolayers of alkanethiolates supported on transparent films of gold. *Journal of the American Chemical Society* **1994**, *116*, 2225.
- (90) Laibinis, P. E.; Whitesides, G. M. Self-assembled monolayers of N-alkanethiolates on copper are barrier films that protect the metal against oxidation by air. *Journal of the American Chemical Society* **1992**, *114*, 9022.
- (91) Whitesides, G. M.; Laibinis, P. E. Wet chemical approaches to the characterization of organic-surfaces - self-assembled monolayers, wetting, and the physical organic-chemistry of the solid liquid interface. *Langmuir* **1990**, *6*, 87.
- (92) Porter, M. D.; Bright, T. B.; Allara, D. L.; Chidsey, C. E. D. Spontaneously organized molecular assemblies .4. structural characterization of normal-alkyl thiol monolayers on gold by optical ellipsometry, infrared-spectroscopy, and electrochemistry. *Journal of the American Chemical Society* **1987**, *109*, 3559.
- (93) Bain, C. D.; Biebuyck, H. A.; Whitesides, G. M. Comparison of self-assembled monolayers on gold - coadsorption of thiols and disulfides. *Langmuir* **1989**, *5*, 723.
- (94) Chidsey, C. E. D.; Loiacono, D. N. Chemical functionality in self-assembled monolayers - structural and electrochemical properties. *Langmuir* **1990**, *6*, 682.
- (95) Troughton, E. B.; Bain, C. D.; Whitesides, G. M.; Nuzzo, R. G.; Allara, D. L.; Porter, M. D. Monolayer films prepared by the spontaneous self-assembly of symmetrical and unsymmetrical dialkyl sulfides from solution onto gold substrates - structure, properties, and reactivity of constituent functional-groups. *Langmuir* **1988**, *4*, 365.
- (96) Xia, Y. N.; Rogers, J. A.; Paul, K. E.; Whitesides, G. M. Unconventional methods for fabricating and patterning nanostructures. *Chemical Reviews* **1999**, *99*, 1823.
- (97) Liu, G. Y.; Xu, S.; Qian, Y. L. Nanofabrication of self-assembled monolayers using scanning probe lithography. *Accounts of Chemical Research* **2000**, *33*, 457.
- (98) Tour, J. M. Molecular electronics. synthesis and testing of components. *Accounts of Chemical Research* **2000**, *33*, 791.
- (99) Joachim, C.; Gimzewski, J. K.; Aviram, A. Electronics using hybrid-molecular and mono-molecular devices. *Nature* **2000**, *408*, 541.

- (100) Sagiv, J. Organized monolayers by adsorption .1. formation and structure of oleophobic mixed monolayers on solid-surfaces. *Journal of the American Chemical Society* **1980**, *102*, 92.
- (101) Faucheux, N.; Schweiss, R.; Lutzow, K.; Werner, C.; Groth, T. Self-assembled monolayers with different terminating groups as model substrates for cell adhesion studies. *Biomaterials* **2004**, *25*, 2721.
- (102) Wasserman, S. R.; Whitesides, G. M.; Tidswell, I. M.; Ocko, B. M.; Pershan, P. S.; Axe, J. D. The structure of self-assembled monolayers of alkylsiloxanes on silicon - a comparison of results from ellipsometry and low-angle x-ray reflectivity. *Journal of the American Chemical Society* **1989**, *111*, 5852.
- (103) Nuzzo, R. G.; Allara, D. L. Adsorption of Bifunctional Organic Disulfides on Gold Surfaces. *Journal of the American Chemical Society* **1983**, *105*, 4481.
- (104) Nuzzo, R. G.; Dubois, L. H.; Allara, D. L. Fundamental-studies of microscopic wetting on organic-surfaces .1. formation and structural characterization of a self-consistent series of polyfunctional organic monolayers. *Journal of the American Chemical Society* **1990**, *112*, 558.
- (105) Tour, J. M.; Jones, L.; Pearson, D. L.; Lamba, J. J. S.; Burgin, T. P.; Whitesides, G. M.; Allara, D. L.; Parikh, A. N.; Atre, S. V. Self-assembled monolayers and multilayers of conjugated thiols, alpha,omega-dithiols, and thioacetyl-containing adsorbates - understanding attachments between potential molecular wires and gold surfaces. *Journal of the American Chemical Society* **1995**, *117*, 9529.
- (106) Himmel, H. J.; Weiss, K.; Jager, B.; Dannenberger, O.; Grunze, M.; Woll, C. Ultrahigh vacuum study on the reactivity of organic surfaces terminated by OH and COOH groups prepared by self-assembly of functionalized alkanethiols on Au substrates. *Langmuir* **1997**, *13*, 4943.
- (107) Kang, J. F.; Ulman, A.; Jordan, R.; Kurth, D. G. Optically induced band shifts in infrared spectra of mixed self-assembled monolayers of biphenyl thiols. *Langmuir* **1999**, *15*, 5555.
- (108) Leung, T. Y. B.; Schwartz, P.; Scoles, G.; Schreiber, F.; Ulman, A. Structure and growth of 4-methyl-4'-mercaptobiphenyl monolayers on Au(111): a surface diffraction study. *Surface Science* **2000**, *458*, 34.
- (109) Fenter, P.; Eisenberger, P.; Li, J.; Camillone, N.; Bernasek, S.; Scoles, G.; Ramanarayanan, T. A.; Liang, K. S. Structure of  $\text{CH}_3(\text{CH}_2)_{17}\text{SH}$  self-assembled on the Ag(111) surface - an incommensurate monolayer. *Langmuir* **1991**, *7*, 2013.
- (110) Laibinis, P. E.; Whitesides, G. M.; Allara, D. L.; Tao, Y. T.; Parikh, A. N.; Nuzzo, R. G. Comparison of the structures and wetting properties of self-assembled monolayers of normal-alkanethiols on the coinage metal-surfaces, Cu, Ag, Au. *Journal of the American Chemical Society* **1991**, *113*, 7152.
- (111) Mekhalif, Z.; Riga, J.; Pireaux, J. J.; Delhalle, J. Self-assembled monolayers of n-dodecanethiol on electrochemically modified polycrystalline nickel surfaces. *Langmuir* **1997**, *13*, 2285.
- (112) Maoz, R.; Sagiv, J. Targeted self-replication of silane multilayers. *Advanced Materials* **1998**, *10*, 580.
- (113) Bain, C. D.; Evall, J.; Whitesides, G. M. Formation of monolayers by the coadsorption of thiols on gold - variation in the head group, tail group, and solvent. *Journal of the American Chemical Society* **1989**, *111*, 7155.

- (114) Fenter, P.; Eisenberger, P.; Liang, K. S. Chain-length dependence of the structures and phases of  $\text{CH}_3(\text{CH}_2)_{N-1}\text{SH}$  self-assembled on Au(111). *Physical Review Letters* **1993**, *70*, 2447.
- (115) Dubois, L. H.; Zegarski, B. R.; Nuzzo, R. G. Molecular ordering of organosulfur compounds on Au(111) and Au(100) - adsorption from solution and in ultrahigh-vacuum. *Journal of Chemical Physics* **1993**, *98*, 678.
- (116) Hu, K.; Bard, A. J. In situ monitoring of kinetics of charged thiol adsorption on gold using an atomic force microscope. *Langmuir* **1998**, *14*, 4790.
- (117) Zhang, H.; He, H. X.; Wang, J.; Liu, Z. F. Atomic force microscopy evidence of citrate displacement by 4-mercaptopyridine on gold in aqueous solution. *Langmuir* **2000**, *16*, 4554.
- (118) Hoffmann, H.; Mayer, U.; Krischanitz, A. Structure of alkylsiloxane monolayers on silicon surfaces investigated by external reflection infrared-spectroscopy. *Langmuir* **1995**, *11*, 1304.
- (119) Jeon, N. L.; Finnie, K.; Branshaw, K.; Nuzzo, R. G. Structure and stability of patterned self-assembled films of octadecyltrichlorosilane formed by contact printing. *Langmuir* **1997**, *13*, 3382.
- (120) Casal, H. L.; Cameron, D. G.; Mantsch, H. H. Infrared-spectra of crystalline normal-alkanes - changes observed during the phase-I -Phase-II Transition. *Canadian Journal of Chemistry-Revue Canadienne De Chimie* **1983**, *61*, 1736.
- (121) Darhuber, A. A.; Troian, S. M.; Davis, J. M.; Miller, S. M.; Wagner, S. Selective dip-coating of chemically micropatterned surfaces. *Journal of Applied Physics* **2000**, *88*, 5119.
- (122) Cai, Y. G. The partially degraded hydrophilic silane pattern and its application in studying the structures of long chain alkane films. *Langmuir* **2009**, *25*, 5594.
- (123) Chowdhury, D.; Maoz, R.; Sagiv, J. Wetting driven self-assembly as a new approach to template-guided fabrication of metal nanopatterns. *Nano Letters* **2007**, *7*, 1770.
- (124) Checco, A.; Cai, Y. G.; Gang, O.; Ocko, B. M. High resolution non-contact AFM imaging of liquids condensed onto chemically nanopatterned surfaces. *Ultramicroscopy* **2006**, *106*, 703.
- (125) Day, H. C.; Allee, D. R. Selective area oxidation of silicon with a scanning force microscope. *Applied Physics Letters* **1993**, *62*, 2691.
- (126) Garcia, R.; Martinez, R. V.; Losilla, N. S.; Martinez, J.; Tello, M. Sequential and parallel patterning by local chemical nanolithography. *Nanotechnology* **2007**, *18*.
- (127) Avouris, P.; Martel, R.; Hertel, T.; Sandstrom, R. AFM-tip-induced and current-induced local oxidation of silicon and metals. *Applied Physics a-Materials Science & Processing* **1998**, *66*, S659.
- (128) Calleja, M.; Garcia, R. Nano-oxidation of silicon surfaces by noncontact atomic-force microscopy: Size dependence on voltage and pulse duration. *Applied Physics Letters* **2000**, *76*, 3427.
- (129) Fontaine, P. A.; Dubois, E.; Stievenard, D. Characterization of scanning tunneling microscopy and atomic force microscopy-based techniques for nanolithography on hydrogen-passivated silicon. *Journal of Applied Physics* **1998**, *84*, 1776.

- (130) Kinser, C. R.; Schmitz, M. J.; Hersam, M. C. Conductive atomic force microscope nanopatterning of hydrogen-passivated silicon in inert organic solvents. *Nano Letters* **2005**, *5*, 91.
- (131) Schoer, J. K.; Zamborini, F. P.; Crooks, R. M. Scanning probe lithography .3. Nanometer-scale electrochemical patterning of Au and organic resists in the absence of intentionally added solvents or electrolytes. *Journal of Physical Chemistry* **1996**, *100*, 11086.
- (132) Mirkin, C. A.; Jang, J. W.; Sanedrin, R. G.; Maspoeh, D.; Hwang, S.; Fujigaya, T.; Jeon, Y. M.; Vega, R. A.; Chen, X. D. Electrically biased nanolithography with KOH-coated AFM tips. *Nano Letters* **2008**, *8*, 1451.
- (133) Xie, X. N.; Chung, H. J.; Sow, C. H.; Wee, A. T. S. Oxide growth and its dielectrical properties on alkylsilated native-SiO<sub>2</sub>/Si surface. *Chemical Physics Letters* **2004**, *388*, 446.
- (134) Yang, M. L.; Zheng, Z. K.; Liu, Y. Q.; Zhang, B. L. Scanned probe oxidation on an octadecyl-terminated silicon (111) surface with an atomic force microscope: kinetic investigations in line patterning. *Nanotechnology* **2006**, *17*, 330.
- (135) Maoz, R.; Cohen, S. R.; Sagiv, J. Nanoelectrochemical patterning of monolayer surfaces: Toward spatially defined self-assembly of nanostructures. *Advanced Materials* **1999**, *11*, 55.
- (136) Sugimura, H. Scanning probe-based chemical conversion of organic monolayers. *Japanese Journal of Applied Physics Part 1-Regular Papers Short Notes & Review Papers* **2004**, *43*, 4477.
- (137) Maoz, R.; Frydman, E.; Cohen, S. R.; Sagiv, J. Constructive nanolithography: Site-defined silver self-assembly on nanoelectrochemically patterned monolayer templates. *Advanced Materials* **2000**, *12*, 424.
- (138) Liu, S. T.; Maoz, R.; Sagiv, J. Planned nanostructures of colloidal gold via self-assembly on hierarchically assembled organic bilayer template patterns with in-situ generated terminal amino functionality. *Nano Letters* **2004**, *4*, 845.
- (139) Liu, S. T.; Maoz, R.; Schmid, G.; Sagiv, J. Template guided self-assembly of [Au<sub>5</sub>(5)] clusters on nanolithographically defined monolayer patterns. *Nano Letters* **2002**, *2*, 1055.
- (140) Wouters, D.; Willems, R.; Hoeppener, S.; Flipse, C. F. J.; Schubert, U. S. Oxidation conditions for octadecyl trichlorosilane monolayers on silicon: A detailed atomic force microscopy study of the effects of pulse height and duration on the oxidation of the monolayer and the underlying Si substrate. *Advanced Functional Materials* **2005**, *15*, 938.
- (141) Nimura, N.; Kinoshita, T.; Yoshida, T.; Uetake, A.; Nakai, C. 1-Pyrenyldiazomethane as a fluorescent labeling reagent for liquid-chromatographic determination of carboxylic-acids. *Analytical Chemistry* **1988**, *60*, 2067.
- (142) Wasserman, S. R.; Tao, Y. T.; Whitesides, G. M. Structure and reactivity of alkylsiloxane monolayers formed by reaction of alkyltrichlorosilanes on silicon substrates. *Langmuir* **1989**, *5*, 1074.
- (143) Yan, B.; Liu, L.; Astor, C. A.; Tang, Q. Determination of the absolute amount of resin bound hydroxyl or carboxyl groups for the optimization of solid phase combinatorial and parallel organic synthesis. *Analytical Chemistry* **1999**, *71*, 4564.

- (144) Sharma, S.; Johnson, R. W.; Desai, T. A. Ultrathin poly(ethylene glycol) films for silicon-based microdevices. *Applied Surface Science* **2003**, *206*, 218.
- (145) Li, L. Y.; Chen, S. F.; Zheng, J.; Ratner, B. D.; Jiang, S. Y. Protein adsorption on oligo(ethylene glycol)-terminated alkanethiolate self-assembled monolayers: The molecular basis for nonfouling behavior. *Journal of Physical Chemistry B* **2005**, *109*, 2934.
- (146) Chapman, R. G.; Ostuni, E.; Takayama, S.; Holmlin, R. E.; Yan, L.; Whitesides, G. M. Surveying for surfaces that resist the adsorption of proteins. *Journal of the American Chemical Society* **2000**, *122*, 8303.
- (147) Feldman, K.; Hahner, G.; Spencer, N. D.; Harder, P.; Grunze, M. Probing resistance to protein adsorption of oligo(ethylene glycol)-terminated self-assembled monolayers by scanning force microscopy. *Journal of the American Chemical Society* **1999**, *121*, 10134.
- (148) Clare, T. L.; Clare, B. H.; Nichols, B. M.; Abbott, N. L.; Hamers, R. J. Functional monolayers for improved resistance to protein adsorption: Oligo(ethylene glycol)-modified silicon and diamond surfaces. *Langmuir* **2005**, *21*, 6344.
- (149) Popat, K. C.; Sharma, S.; Johnson, R. W.; Desai, T. A. AFM analysis of organic silane thin films for bioMEMS applications. *Surface and Interface Analysis* **2003**, *35*, 205.
- (150) Cai, C. Z.; Gu, J. H.; Yam, C. M.; Li, S. Nanometric protein arrays on protein-resistant monolayers on silicon surfaces. *Journal of the American Chemical Society* **2004**, *126*, 8098.
- (151) Arenkov, P.; Kukhtin, A.; Gemell, A.; Voloshchuk, S.; Chupeeva, V.; Mirzabekov, A. Protein microchips: Use for immunoassay and enzymatic reactions. *Analytical Biochemistry* **2000**, *278*, 123.
- (152) Nicolau, D. V.; Taguchi, T.; Taniguchi, H.; Yoshikawa, S. Negative and positive tone protein patterning on e-beam/deep-UV resists. *Langmuir* **1999**, *15*, 3845.
- (153) Hoff, J. D.; Cheng, L. J.; Meyhofer, E.; Guo, L. J.; Hunt, A. J. Nanoscale protein patterning by imprint lithography. *Nano Letters* **2004**, *4*, 853.
- (154) Pavlovic, E.; Oscarsson, S.; Quist, A. P. Nanoscale site-specific immobilization of proteins through electroactivated disulfide exchange. *Nano Letters* **2003**, *3*, 779.
- (155) Mooney, J. F.; Hunt, A. J.; McIntosh, J. R.; Liberko, C. A.; Walba, D. M.; Rogers, C. T. Patterning of functional antibodies and other proteins by photolithography of silane monolayers. *Proceedings of the National Academy of Sciences of the United States of America* **1996**, *93*, 12287.
- (156) Maoz, R.; Matlis, S.; DiMasi, E.; Ocko, B. M.; Sagiv, J. Self-replicating amphiphilic monolayers. *Nature* **1996**, *384*, 150.
- (157) Sauter, C.; Otalora, F.; Gavira, J. A.; Vidal, O.; Giege, R.; Garcia-Ruiz, J. M. Structure of tetragonal hen egg-white lysozyme at 0.94 angstrom from crystals grown by the counter-diffusion method. *Acta Crystallographica Section D-Biological Crystallography* **2001**, *57*, 1119.
- (158) Gershevit, O.; Sukenik, C. N. In situ FTIR-ATR analysis and titration of carboxylic acid-terminated SAMs. *Journal of the American Chemical Society* **2004**, *126*, 482.



- (159) Koehler, J. A.; Ulbricht, M.; Belfort, G. Intermolecular forces between proteins and polymer films with relevance to filtration. *Langmuir* **1997**, *13*, 4162.
- (160) Gao, P.; Cai, Y. G. The boundary molecules in a lysozyme pattern exhibit preferential antibody binding. *Langmuir* **2008**, *24*, 10334.
- (161) Li, L. Y.; Chen, S. F.; Oh, S. J.; Jiang, S. Y. In situ single-molecule detection of antibody-antigen binding by tapping-mode atomic force microscopy. *Analytical Chemistry* **2002**, *74*, 6017.
- (162) Cullen, D. C.; Lowe, C. R. AFM studies of protein adsorption .1. time-resolved protein adsorption to highly oriented pyrolytic-graphite. *Journal of Colloid and Interface Science* **1994**, *166*, 102.
- (163) Xu, H.; Zhao, X. B.; Grant, C.; Lu, J. R.; Williams, D. E.; Penfold, J. Orientation of a monoclonal antibody adsorbed at the solid/solution interface: A combined study using atomic force microscopy and neutron reflectivity. *Langmuir* **2006**, *22*, 6313.
- (164) Patel, N.; Sanders, G. H. W.; Shakesheff, K. M.; Cannizzaro, S. M.; Davies, M. C.; Langer, R.; Roberts, C. J.; Tendler, S. J. B.; Williams, P. M. Atomic force microscopic analysis of highly defined protein patterns formed by microfluidic networks. *Langmuir* **1999**, *15*, 7252.
- (165) Chin, D.; Means, A. R. Calmodulin: a prototypical calcium sensor. *Trends in Cell Biology* **2000**, *10*, 322.
- (166) Allbritton, N. L.; Meyer, T. Localized calcium spikes and propagating calcium waves. *Cell Calcium* **1993**, *14*, 691.
- (167) Hardingham, G. E.; Cruzalegui, F. H.; Chawla, S.; Bading, H. Mechanisms controlling gene expression by nuclear calcium signals. *Cell Calcium* **1998**, *23*, 131.
- (168) Thomas, A. P.; Bird, G. S. J.; Hajnoczky, G.; RobbGaspers, L. D.; Putney, J. W. Spatial and temporal aspects of cellular calcium signaling. *Faseb Journal* **1996**, *10*, 1505.
- (169) Ghosh, A.; Greenberg, M. E. Calcium signaling in neurons - molecular mechanisms and cellular consequences. *Science* **1995**, *268*, 239.
- (170) Sheldon, R. A. Enzyme immobilization: The quest for optimum performance. *Advanced Synthesis & Catalysis* **2007**, *349*, 1289.
- (171) Lim, J. H.; Ginger, D. S.; Lee, K. B.; Heo, J.; Nam, J. M.; Mirkin, C. A. Direct-write dip-pen nanolithography of proteins on modified silicon oxide surfaces. *Angewandte Chemie-International Edition* **2003**, *42*, 2309.
- (172) Rinaldi, R.; Biasco, A.; Maruccio, G.; Arima, V.; Visconti, P.; Cingolani, R.; Facci, P.; De Rienzo, F.; Di Felice, R.; Molinari, E.; Verbeet, M. P.; Canters, G. W. Electronic rectification in protein devices. *Applied Physics Letters* **2003**, *82*, 472.
- (173) Choi, E. J.; Foster, M. D.; Daly, S.; Tilton, R.; Przybycien, T.; Majkrzak, C. F.; Witte, P.; Menzel, H. Effect of flow on human serum albumin adsorption to self-assembled monolayers of varying packing density. *Langmuir* **2003**, *19*, 5464.
- (174) Veiseh, M.; Zareie, M. H.; Zhang, M. Q. Highly selective protein patterning on gold-silicon substrates for biosensor applications. *Langmuir* **2002**, *18*, 6671.
- (175) Liu, G. Y.; Amro, N. A. Positioning protein molecules on surfaces: A nanoengineering approach to supramolecular chemistry. *Proceedings of the National Academy of Sciences of the United States of America* **2002**, *99*, 5165.

- (176) Lee, K. B.; Park, S. J.; Mirkin, C. A.; Smith, J. C.; Mirksich, M. Protein nanoarrays generated by dip-pen nanolithography. *Science* **2002**, *295*, 1702.
- (177) MacBeath, G.; Schreiber, S. L. Printing proteins as microarrays for high-throughput function determination. *Science* **2000**, *289*, 1760.
- (178) Soong, R. K.; Bachand, G. D.; Neves, H. P.; Olkhovets, A. G.; Craighead, H. G.; Montemagno, C. D. Powering an inorganic nanodevice with a biomolecular motor. *Science* **2000**, *290*, 1555.
- (179) Pallandre, A.; De Meersman, B.; Blondeau, F.; Nysten, B.; Jonas, A. M. Tuning the orientation of an antigen by adsorption onto nanostriped templates. *Journal of the American Chemical Society* **2005**, *127*, 4320.
- (180) Leisten, F.; Wiechmann, M.; Enders, O.; Kolb, H. A. Generation of nanostructures of mica supported lysozyme molecules in aqueous solution by atomic force microscopy. *Journal of Colloid and Interface Science* **2006**, *298*, 508.
- (181) BrowningKelley, M. E.; WaduMesthrige, K.; Hari, V.; Liu, G. Y. Atomic force microscopic study of specific antigen/antibody binding. *Langmuir* **1997**, *13*, 343.
- (182) Cai, Y. G.; Ocko, B. M. Large-scale fabrication of protein nanoarrays based on nanosphere lithography. *Langmuir* **2005**, *21*, 9274.
- (183) Wadu-Mesthrige, K.; Xu, S.; Amro, N. A.; Liu, G. Y. Fabrication and imaging of nanometer-sized protein patterns. *Langmuir* **1999**, *15*, 8580.
- (184) Davies, D. R.; Cohen, G. H. Interactions of protein antigens with antibodies. *Proceedings of the National Academy of Sciences of the United States of America* **1996**, *93*, 7.
- (185) Blawas, A. S.; Reichert, W. M. Protein patterning. *Biomaterials* **1998**, *19*, 595.
- (186) Zhu, H.; Snyder, M. Protein chip technology. *Current Opinion in Chemical Biology* **2003**, *7*, 55.
- (187) Cahill, D. J. Protein and antibody arrays and their medical applications. *Journal of Immunological Methods* **2001**, *250*, 81.
- (188) Ramsay, G. DNA chips: State-of-the-art. *Nature Biotechnology* **1998**, *16*, 40.
- (189) Sinensky, A. K.; Belcher, A. M. Label-free and high-resolution protein/DNA nanoarray analysis using Kelvin probe force microscopy. *Nature Nanotechnology* **2007**, *2*, 653.
- (190) Palermo, V.; Palma, M.; Samori, P. Electronic characterization of organic thin films by Kelvin probe force microscopy. *Advanced Materials* **2006**, *18*, 145.
- (191) Laoudj, D.; Guasch, C.; Renault, E.; Bennes, R.; Bonnet, J. Surface potential mapping of dispersed proteins. *Analytical and Bioanalytical Chemistry* **2005**, *381*, 1476.
- (192) Cheran, L. E.; Sadeghi, S.; Thompson, M. Scanning Kelvin nanoprobe detection in materials science and biochemical analysis. *Analyst* **2005**, *130*, 1569.
- (193) Thompson, M.; Cheran, L. E.; Zhang, M. Q.; Chacko, M.; Huo, H.; Sadeghi, S. Label-free detection of nucleic acid and protein microarrays by scanning Kelvin nanoprobe. *Biosensors & Bioelectronics* **2005**, *20*, 1471.
- (194) Hansen, D. C.; Hansen, K. M.; Ferrell, T. L.; Thundat, T. Discerning biomolecular interactions using Kelvin probe technology. *Langmuir* **2003**, *19*, 7514.

- (195) Mairal, T.; Ozalp, V. C.; Sanchez, P. L.; Mir, M.; Katakis, I.; O'Sullivan, C. K. Aptamers: molecular tools for analytical applications. *Analytical and Bioanalytical Chemistry* **2008**, *390*, 989.
- (196) Cheng, A. K. H.; Ge, B.; Yu, H. Z. Aptamer-based biosensors for label-free voltammetric detection of lysozyme. *Analytical Chemistry* **2007**, *79*, 5158.
- (197) Wang, J. L.; Zhou, H. S. Aptamer-based Au nanoparticles-enhanced surface plasmon resonance detection of small molecules. *Analytical Chemistry* **2008**, *80*, 7174.
- (198) Willner, I.; Zayats, M. Electronic aptamer-based sensors. *Angewandte Chemie-International Edition* **2007**, *46*, 6408.
- (199) Tombelli, S.; Minunni, A.; Mascini, A. Analytical applications of aptamers. *Biosensors & Bioelectronics* **2005**, *20*, 2424.
- (200) Rodriguez, M. C.; Kawde, A. N.; Wang, J. Aptamer biosensor for label-free impedance spectroscopy detection of proteins based on recognition-induced switching of the surface charge. *Chemical Communications* **2005**, 4267.
- (201) Nutiu, R.; Li, Y. F. Structure-switching signaling aptamers: Transducing molecular recognition into fluorescence signaling. *Chemistry-a European Journal* **2004**, *10*, 1868.
- (202) Navani, N. K.; Li, Y. F. Nucleic acid aptamers and enzymes as sensors. *Current Opinion in Chemical Biology* **2006**, *10*, 272.
- (203) Kawde, A. N.; Rodriguez, M. C.; Lee, T. M. H.; Wang, J. Label-free bioelectronic detection of aptamer-protein interactions. *Electrochemistry Communications* **2005**, *7*, 537.
- (204) Nutiu, R.; Li, Y. F. Structure-switching signaling aptamers. *Journal of the American Chemical Society* **2003**, *125*, 4771.
- (205) White, R. J.; Phares, N.; Lubin, A. A.; Xiao, Y.; Plaxco, K. W. Optimization of electrochemical aptamer-based sensors via optimization of probe packing density and surface chemistry. *Langmuir* **2008**, *24*, 10513.
- (206) Hamula, C. L. A.; Guthrie, J. W.; Zhang, H. Q.; Li, X. F.; Le, X. C. Selection and analytical applications of aptamers. *Trac-Trends in Analytical Chemistry* **2006**, *25*, 681.
- (207) Kirby, R.; Cho, E. J.; Gehrke, B.; Bayer, T.; Park, Y. S.; Neikirk, D. P.; McDevitt, J. T.; Ellington, A. D. Aptamer-based sensor arrays for the detection and quantitation of proteins. *Analytical Chemistry* **2004**, *76*, 4066.
- (208) Gao, P.; Cai, Y. G. A method for fabricating protein patterns on the octadecyltrichlorosilane(OTS) surface through paper swabbing. *Ultramicroscopy* **2009**, *109*, 1023.
- (209) Kim, D. T.; Blanch, H. W.; Radke, C. J. Direct imaging of lysozyme adsorption onto mica by atomic force microscopy. *Langmuir* **2002**, *18*, 5841.
- (210) Smith, S. B.; Cui, Y. J.; Bustamante, C. Overstretching B-DNA: The elastic response of individual double-stranded and single-stranded DNA molecules. *Science* **1996**, *271*, 795.
- (211) Balint, Z.; Nagy, K.; Laczko, I.; Bottka, S.; Vegh, G. A.; Szegletes, Z.; Varo, G. Adsorption and self-assembly of oligodeoxynucleotides onto a mica surface. *Journal of Physical Chemistry C* **2007**, *111*, 17032.

- (212) Nonnenmacher, M.; Oboyle, M. P.; Wickramasinghe, H. K. Kelvin probe force microscopy. *Applied Physics Letters* **1991**, *58*, 2921.
- (213) Zisman, W. A. A new method of measuring contact potential differences in metals. *Review of Scientific Instruments* **1932**, *3*, 367.
- (214) Jacobs, H. O.; Leuchtmann, P.; Homan, O. J.; Stemmer, A. Resolution and contrast in Kelvin probe force microscopy. *Journal of Applied Physics* **1998**, *84*, 1168.
- (215) Saito, N.; Hayashi, K.; Sugimura, H.; Takai, O.; Nakagiri, N. Surface potential images of self-assembled monolayers patterned by organosilanes: ab initio molecular orbital calculations. *Surface and Interface Analysis* **2002**, *34*, 601.
- (216) Yazdanpanah, M. M.; Harfenist, S. A.; Safir, A.; Cohn, R. W. Selective self-assembly at room temperature of individual freestanding Ag<sub>2</sub>Ga alloy nanoneedles. *Journal of Applied Physics* **2005**, *98*.
- (217) Jacobs, H. O.; Knapp, H. F.; Stemmer, A. Practical aspects of Kelvin probe force microscopy. *Review of Scientific Instruments* **1999**, *70*, 1756.
- (218) Kolmakov, A.; Moskovits, M. Chemical sensing and catalysis by one-dimensional metal-oxide nanostructures. *Annual Review of Materials Research* **2004**, *34*, 151.
- (219) Goldberger, J.; Hochbaum, A. I.; Fan, R.; Yang, P. D. Silicon vertically integrated nanowire field effect transistors. *Nano Letters* **2006**, *6*, 973.
- (220) Liu, H. Q.; Kameoka, J.; Czaplewski, D. A.; Craighead, H. G. Polymeric nanowire chemical sensor. *Nano Letters* **2004**, *4*, 671.
- (221) Law, M.; Greene, L. E.; Johnson, J. C.; Saykally, R.; Yang, P. D. Nanowire dye-sensitized solar cells. *Nature Materials* **2005**, *4*, 455.
- (222) Cui, Y.; Wei, Q. Q.; Park, H. K.; Lieber, C. M. Nanowire nanosensors for highly sensitive and selective detection of biological and chemical species. *Science* **2001**, *293*, 1289.
- (223) Martensson, T.; Carlberg, P.; Borgstrom, M.; Montelius, L.; Seifert, W.; Samuelson, L. Nanowire arrays defined by nanoimprint lithography. *Nano Letters* **2004**, *4*, 699.
- (224) Sun, Y. G.; Khang, D. Y.; Hua, F.; Hurley, K.; Nuzzo, R. G.; Rogers, J. A. Photolithographic route to the fabrication of micro/nanowires of III-V semiconductors. *Advanced Functional Materials* **2005**, *15*, 30.
- (225) Menke, E. J.; Thompson, M. A.; Xiang, C.; Yang, L. C.; Penner, R. M. Lithographically patterned nanowire electrodeposition. *Nature Materials* **2006**, *5*, 914.
- (226) Lu, W.; Lieber, C. M. Nanoelectronics from the bottom up. *Nature Materials* **2007**, *6*, 841.
- (227) Friedrichs, E.; Simmel, F. C. Controlling DNA polymerization with a switchable aptamer. *ChemBiochem* **2007**, *8*, 1662.
- (228) Seeman, N. C. DNA in a material world. *Nature* **2003**, *421*, 427.
- (229) Yan, H.; Park, S. H.; Finkelstein, G.; Reif, J. H.; LaBean, T. H. DNA-templated self-assembly of protein arrays and highly conductive nanowires. *Science* **2003**, *301*, 1882.
- (230) Simmel, F. C.; Dittmer, W. U. DNA nanodevices. *Small* **2005**, *1*, 284.
- (231) Liu, Y.; Lin, C. X.; Li, H. Y.; Yan, H. Protein nanoarrays - Aptamer-directed self-assembly of protein arrays on a DNA nanostructure. *Angewandte Chemie-International Edition* **2005**, *44*, 4333.

- (232) Chhabra, R.; Sharma, J.; Ke, Y. G.; Liu, Y.; Rinker, S.; Lindsay, S.; Yan, H. Spatially addressable multiprotein nanoarrays templated by aptamer-tagged DNA nanoarchitectures. *Journal of the American Chemical Society* **2007**, *129*, 10304.
- (233) Gao, P.; Cai, Y. G. Label-free detection of the aptamer binding on protein patterns using Kelvin probe force microscopy (KPFM). *Analytical and Bioanalytical Chemistry* **2009**, *394*, 207.
- (234) Lepecq, J. B.; Paoletti, C. A fluorescent complex between ethidium bromide and nucleic acids - physical-chemical characterization. *Journal of Molecular Biology* **1967**, *27*, 87.
- (235) Waring, M. J. *Journal of Molecular Biology* **1965**, *13*, 269.
- (236) Aldaye, F. A.; Sleiman, H. F. Guest-mediated access to a single DNA nanostructure from a library of multiple assemblies. *Journal of the American Chemical Society* **2007**, *129*, 10070.
- (237) Li, Y. G.; Tseng, Y. D.; Kwon, S. Y.; D'Espaux, L.; Bunch, J. S.; Mceuen, P. L.; Luo, D. Controlled assembly of dendrimer-like DNA. *Nature Materials* **2004**, *3*, 38.
- (238) Witten, T. A.; Sander, L. M. Diffusion-limited aggregation, a kinetic critical phenomenon. *Physical Review Letters* **1981**, *47*, 1400.
- (239) Xiao, L. H.; Zhou, R.; He, Y.; Li, Y. J.; Yeung, E. S. Direct observation of nanoparticle self-assembly dynamics at the water-air interface using differential interference contrast microscopy. *Journal of Physical Chemistry C* **2009**, *113*, 1209.
- (240) Roder, H.; Hahn, E.; Brune, H.; Bucher, J. P.; Kern, K. Building one-dimensional and 2-dimensional nanostructures by diffusion-controlled aggregation at surfaces. *Nature* **1993**, *366*, 141.
- (241) Hurd, A. J.; Schaefer, D. W. Diffusion-limited aggregation in 2 dimensions. *Physical Review Letters* **1985**, *54*, 1043.
- (242) Meakin, P. Formation of fractal clusters and networks by irreversible diffusion-limited aggregation. *Physical Review Letters* **1983**, *51*, 1119.
- (243) Gomezrodriguez, J. M.; Baro, A. M.; Vazquez, L.; Salvarezza, R. C.; Vara, J. M.; Arvia, A. J. Fractal surfaces of gold and platinum electrodeposits - dimensionality determination by scanning tunneling microscopy. *Journal of Physical Chemistry* **1992**, *96*, 347.
- (244) Samson, J.; Varotto, A.; Nahirney, P. C.; Toschi, A.; Piscopo, I.; Drain, C. M. Fabrication of metal nanoparticles using toroidal plasmid DNA as a sacrificial mold. *Acs Nano* **2009**, *3*, 339.
- (245) Stoltenberg, R. M.; Woolley, A. T. DNA-templated nanowire fabrication. *Biomedical Microdevices* **2004**, *6*, 105.
- (246) Deng, Z. X.; Mao, C. D. DNA-templated fabrication of 1D parallel and 2D crossed metallic nanowire arrays. *Nano Letters* **2003**, *3*, 1545.
- (247) Gu, Q.; Cheng, C. D.; Gonela, R.; Suryanarayanan, S.; Anabathula, S.; Dai, K.; Haynie, D. T. DNA nanowire fabrication. *Nanotechnology* **2006**, *17*, R14.
- (248) Richter, J.; Seidel, R.; Kirsch, R.; Mertig, M.; Pompe, W.; Plaschke, J.; Schackert, H. K. Nanoscale palladium metallization of DNA. *Advanced Materials* **2000**, *12*, 507.
- (249) Richter, J.; Mertig, M.; Pompe, W.; Vinzelberg, H. Low-temperature resistance of DNA-templated nanowires. *Applied Physics a-Materials Science & Processing* **2002**, *74*, 725.

- (250) Richter, J. Metallization of DNA. *Physica E-Low-Dimensional Systems & Nanostructures* **2003**, *16*, 157.
- (251) Braun, E.; Eichen, Y.; Sivan, U.; Ben-Yoseph, G. DNA-templated assembly and electrode attachment of a conducting silver wire. *Nature* **1998**, *391*, 775.
- (252) Livnah, O.; Bayer, E. A.; Wilchek, M.; Sussman, J. L. 3-Dimensional structures of avidin and the avidin-biotin complex. *Proceedings of the National Academy of Sciences of the United States of America* **1993**, *90*, 5076.
- (253) Leung, C.; Kinns, H.; Hoogenboom, B. W.; Howorka, S.; Mesquida, P. Imaging surface charges of individual biomolecules. *Nano Letters* **2009**, *9*, 2769.
- (254) Park, S. H.; Yin, P.; Liu, Y.; Reif, J. H.; LaBean, T. H.; Yan, H. Programmable DNA self-assemblies for nanoscale organization of ligands and proteins. *Nano Letters* **2005**, *5*, 729.
- (255) Singh, G.; Griesser, H. J.; Bremmell, K.; Kingshott, P. Highly ordered nanometer-scale chemical and protein patterns by binary colloidal crystal lithography combined with plasma polymerization. *Advanced Functional Materials* **2011**, *21*, 540.
- (256) Garno, J. C.; Amro, N. A.; Wadu-Mesthrige, K.; Liu, G. Y. Production of periodic arrays of protein nanostructures using particle lithography. *Langmuir* **2002**, *18*, 8186.
- (257) Noy, A.; Vezenov, D. V.; Lieber, C. M. Chemical force microscopy. *Annual Review of Materials Science* **1997**, *27*, 381.
- (258) Xiao, X. D.; Hu, J.; Charych, D. H.; Salmeron, M. Chain length dependence of the frictional properties of alkylsilane molecules self-assembled on Mica studied by atomic force microscopy. *Langmuir* **1996**, *12*, 235.
- (259) Green, C. P.; Sader, J. E. Torsional frequency response of cantilever beams immersed in viscous fluids with applications to the atomic force microscope. *Journal of Applied Physics* **2002**, *92*, 6262.
- (260) Green, C. P.; Lioe, H.; Cleveland, J. P.; Proksch, R.; Mulvaney, P.; Sader, J. E. Normal and torsional spring constants of atomic force microscope cantilevers. *Review of Scientific Instruments* **2004**, *75*, 1988.
- (261) Flater, E. E.; Ashurst, W. R.; Carpick, R. W. Nanotribology of octadecyltrichlorosilane monolayers and silicon: Self-mated versus unmated interfaces and local packing density effects. *Langmuir* **2007**, *23*, 9242.

## VITA

Pei Gao

### DATE AND PLACE OF BIRTH

June 11, 1979, P.R. CHINA

### EDUCATION

M.S., Electrochemistry, Wuhan University, Wuhan, P. R. China 2004  
B.S., Applied Chemistry, Zhengzhou University, Zhengzhou, P. R. China 2001

### RESEARCH EXPERIENCE

Department of Chemistry, University of Kentucky, 2006 to 2011  
Department of Chemistry, Wuhan University, 2001 to 2004

### AWARDS AND FELLOWSHIPS

Research Challenge Trust Fund (RCTF) Fellowship, University of Kentucky, 2009-2011  
Outstanding Research Award, University of Kentucky, 2009  
Champion Award in Graduate Research Competition of the 94th Annual Meeting of the Kentucky Academy of Science, 2008

### PUBLICATIONS

- (1) Detection of protein–DNA interaction and regulation using gold nanoparticles. Fang, J.; Yu, L. L.; Gao, P.; Cai, Y. G.; Wei, Y. A. *Anal Biochem* 2010, 399, 262.
- (2) Aptamer Fiber Anchored on the Edge of a Protein Pattern: A Template for Nanowire Fabrication. Gao, P.; Cai, Y. G. *Acs Nano* 2009, 3, 3475.
- (3) A method for fabricating protein patterns on the Octadecyltrichlorosilane (OTS) surface through paper swabbing. Gao, P.; Cai, Y. G. *Ultramicroscopy* 2009, 109, 1023.
- (4) Label-free detection of the aptamer binding on protein patterns using Kelvin probe force microscopy (KPFM). Gao, P.; Cai, Y. G. *Analytical and Bioanalytical Chemistry* 2009, 394, 207. (Cover Story)
- (5) The Boundary Molecules in a Lysozyme Pattern Exhibit Preferential Antibody Binding. Gao, P.; Cai, Y. G. *Langmuir* 2008, 24, 10334.
- (6) A quartz sealed Ag/AgCl reference electrode for CaCl<sub>2</sub> based molten salts. Gao, P.; Jin, X. B.; Wang, D. H.; Hu, X. H.; Chen, G. Z. *Journal of Electroanalytical Chemistry* 2005, 579, 321.
- (7) Electrochemical preparation of silicon and its alloys from solid oxides in molten calcium chloride. Jin, X. B.; Gao, P.; Wang, D. H.; Hu, X. H.; Chen, G. Z. *Angewandte Chemie-International Edition* 2004, 43, 733.